ABSTRACT

Title of Dissertation: THERMO-STRUCTURAL INFLUENCES ON OPTICAL CHARACTERISTICS of POLYMER BRAGG GRATINGS

Kyoung Joon Kim, Doctor of Philosophy, 2006

Dissertation directed by: Professor Avram Bar-Cohen
Professor Bongtae Han
Department of Mechanical Engineering

The objective of this study is to investigate thermo-optical issues in polymer Bragg gratings. The first order thermo-optical model of a polymer Bragg grating is provided. The model was applied to investigate the thermo-optical behavior of the PMMA Bragg grating. The development of a thermo-optical model of an illuminated polymer fiber Bragg grating (PFBG), combining use of the coupled-mode theory with thermal conduction theory and the Transfer Matrix Method (TMM), is presented. The model is verified comparing predicted results with the measured values of the thermo-optical experiment. This model is applied to the prediction of the thermo-optical behavior of an intrinsically-heated and passively-cooled PMMA Fiber Bragg Grating illuminated by a

LED and SMLDs and operating over a range of ambient temperatures. Parametric influences on the thermo-optic characteristics and the predictive accuracy of several simplifications in the Bragg Grating relations are also explored.

THERMO-STRUCTURAL INFLUENCES ON OPTICAL CHARACTERISTICS of POLYMER BRAGG GRATINGS

by

Kyoung Joon Kim

Dissertation submitted to the Faculty of the Graduate School of the
University of Maryland, College Park in partial fulfillment
of the requirements for the degree of
Doctor of Philosophy
2006

Advisory Committee:
Professor Avram Bar-Cohen, Chair
Associate Professor Bongtae Han, Co-Chair
Professor Julius Goldhar
Professor Abhijit Dasgupta
Assistant Professor Bao Yang

To my wife, Eun Ha Lee
and my daughter, Christine Kim

ACKNOWLEDGEMENT

I would like to thank my advisor, Professor Avram Bar-Cohen and co-advisor, Professor Bongtae Han for their significant supports, helpful advices, and encouragements for the research work during the Ph.D. study in Mechanical Engineering at University of Maryland. I would like to extend my thanks to Professor Julius Goldhar for great discussions and Professor Miao Yu for her generosity in allowing me the use of laboratory equipment as well as the space for the experiment. I thank the other committee members, Professors Abhijit Dasgupta and Bao Yang, for good comments and advice. I also like to thank Dr. Seungmin Cho and Dae Whan Kim for their assistance in the research work. I thank Dr. Changwoon Han, Dr. Samson Yoon, Dr. Yuchul Hwang, Dr. Junpyo Lee, Yuri Lee, Peng Wang, Chris Bachmann, Kevin Moores for their friendships during the Ph.D. study.

I really want to thank my wife, Eun Ha Lee and my daughter, Christine Sayhee Kim for their tremendous patience, sincere support, encouragement and trust. I would like to thank my father, Jaeok Kim, my mother, Chooja Moon, my brother, Kyungman Kim, my sister, Dr. Sooyeon Kim, and my brother-in law, Dr. Bumjin Song for their sincere support and encouragement.

TABLE OF CONTENTS

LIST OF TABLES

LIST OF FIGURES

Chapter 1

Introduction

Despite their relatively high light absorption rates, polymer materials provide a potent alternative to conventional optical materials due to low-cost, ease of fabrication and assembly, and compatibility with other materials. The recent literature reveals a rapidly increasing interest in the use of polymer components in photonics systems.[1] While polymer waveguides are currently receiving much of the attention, it is to be expected that signal management requirements will lead to progressively greater efforts in gratings, mirrors, and lenses.

A Bragg grating (BG) in a light transmitting waveguide produces a very narrow band of reflected optical energy, with a maximum reflectivity at the characteristic wavelength of the grating, called the *Bragg wavelength*, as illustrated in Figure 1.1. Unlike the conventional glass fibers, the index of refraction in light-transmitting polymers typically varies inversely with the temperature, leading to negative thermo-optic coefficients that are 10 to 30 times greater than the positive thermo-optic coefficient of conventional silica glass [1]. This strong negative thermo-optical characteristic imbues polymer BGs, generally packaged on low thermal expansion substrates, with precise wavelength discrimination when used as tuning filters.

Another important characteristic of polymeric optical materials is their relatively high light absorption rate, at approximately 0.2 dB/cm, as compared to 0.2 dB/km for glass fibers at wavelength of 1550 nm. However, as shown in Figure 1.2 for the Acrylic-based polymers of Allied Signal [1], the absorption rates of polymeric optical materials

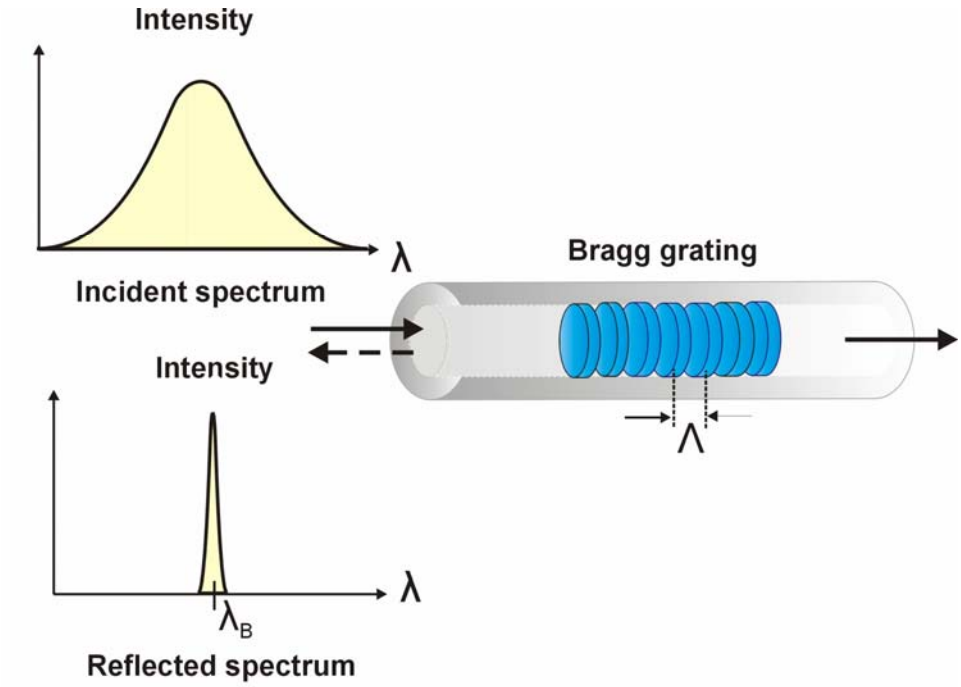

Figure 1.1: Fundamental characteristics of a Bragg grating

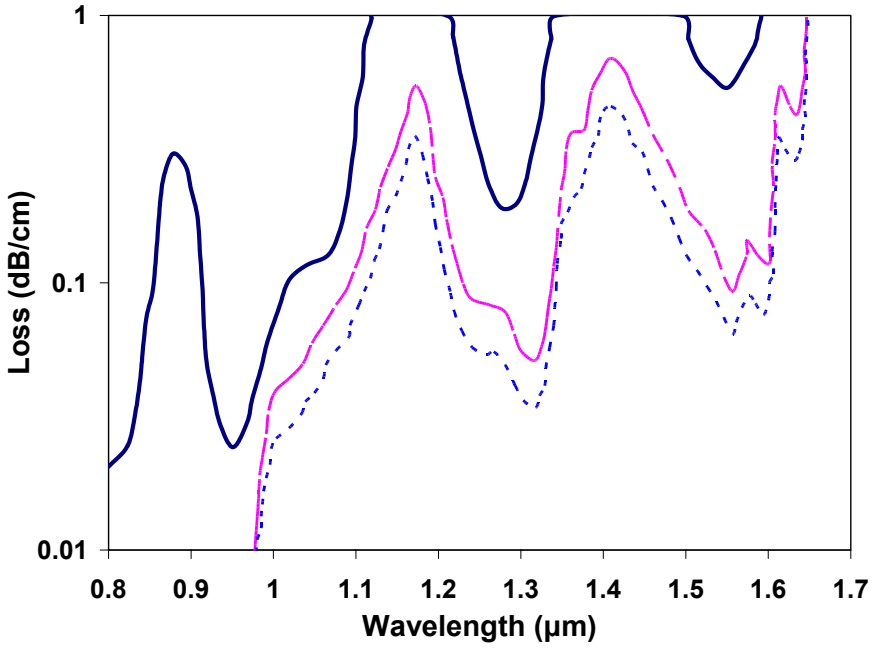

Figure 1.2: Light absorptions in polymer systems {Allied Signal Acrylic: solid line –100% CH; dashed line –30% CH; dotted line –20% CH}[1]

strongly depends on the wavelength. For example, in Acrylic with full CH content, the absorption rate (0.5 dB/cm) at 1.55 μm is 25 times greater than that at 0.8 μm. Intrinsic self-heating, resulting from these high absorption rates, can produce considerable temperature changes within polymer waveguides and gratings. Such self-heating, as well as the induced temperature gradients and possible changes in the ambient temperature, can cause undesirable shifts in the Bragg wavelength and changes in the reflectivity/transmissivity of the grating.

To facilitate the selection of polymeric optical materials and the rational design of polymer BGs, this thesis seeks to provide a complete understanding of thermo-optic behavior of polymer BG's. Following this introduction, Chapter 2 describes the physical aspects and explains the basic optical principles of BGs. Chapter 3 describes a typical structure of a polymer Bragg grating waveguide, and presents first order thermal, thermo-structural, and thermo-optical models of a self-heated polymer BG waveguide. Chapter 3 also presents the results of applying these first-order models to the determination of the Bragg wavelength shift in an illuminated PMMA **(**Polymethylmetacrylate**)** Bragg grating waveguide.

Chapter 4 presents a methodology for the detailed thermo-optical modeling of a self-heated polymer fiber Bragg grating (PFBG) associated with the intrinsic absorption of light energy. An analytical formulation based on coupled-mode theory is described, which determines the power variation induced by the coupling between counter-directional light waves within the PFBG. An analytical description for absorption-induced heat generation is provided and is then embedded in a model for the temperature distribution in the grating. A numerical thermo-optical model, using the Transfer Matrix

Method (TMM), along with a simple analytical thermo-optical model, is also given. Chapter 5 focuses on the apparatus used to obtain experimental thermo-optical data and compares the obtained spectral characteristics of an isothermal Fiber Bragg Grating (FBG) and a non-isothermal FBG with the predicted values.

Chapter 6 discusses the thermo-optical behavior of a self-heated PMMA FBG associated with LED illumination. Spectral characteristics, as well as effects of incident optical power and ambient temperature, on the Bragg wavelength shift are presented. Chapter 7 shows the thermo-optical behavior of the PMMA FBG illuminated by single mode laser diodes, including the thermally-induced spectral changes of the reflected optical signals of the PMMA FBG and the detailed parametric results in the Bragg wavelength shifts. Chapter 8 summarizes this thesis and suggests future research to further examine the thermo-optical behavior of polymer Bragg gratings.

Chapter 2

Fundamentals of Bragg Gratings

2.1 Physical Descriptions

A Bragg grating (BG) can be formed by index modulations in the waveguide material, induced by exposure to ultraviolet (UV) light and/or doping [2-4], or by trenching (interrupting) of the waveguide material with etchants and/or focused laser beams [5]. A BG formed by UV exposure and/or doping, without physical trenches, is referred to as a *bulk index grating*, and a BG formed by physical deformation is referred to as a *surface relief grating*. Bragg gratings (BGs) can be found in numerous photonic components and systems, including distributed feedback laser diodes (DFB LDs), distributed Bragg reflector laser diodes (DBR LDs) and can be formed in optical fibers, as well as in planar waveguides.

Two of the most popular forms of BGs are illustrated in Figures 2.1 and 2.2; a fiber Bragg grating (FBG), i.e. a BG formed in a fiber, and a planar Bragg grating (PBG), i.e. a BG in a planar waveguide. A FBG is usually a bulk index grating, while both surface relief and bulk indexing are used to create a PBG.

Figure 2.3 illustrates the most widely used *phase-mask* technique to inscribe a BG in an optical fiber [3], using a diffractive optical component (a transmission diffraction grating) as a phase-mask. The phase mask is designed and fabricated to suppress the zeroth order diffraction, while the ±1st diffraction orders interfere to produce a sinusoidal intensity distribution in space. A doped photosensitive optical fiber is placed in the region where the two beams intersect and a BG is imprinted on a glass or polymer fiber.

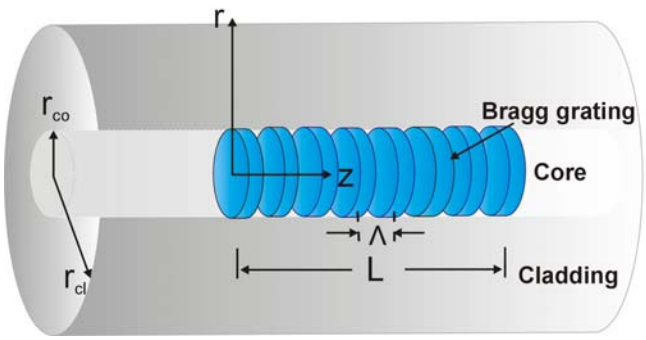

Figure 2.1: Fiber Bragg grating structure

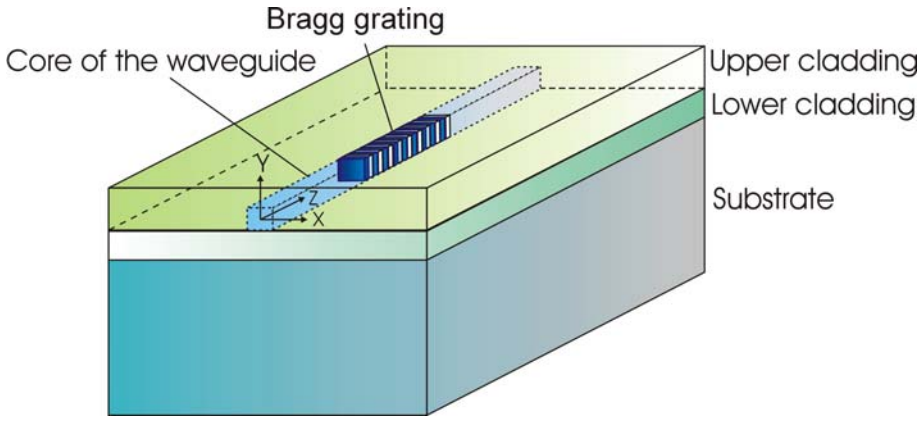

Figure 2.2: Packaged planar Bragg grating structure

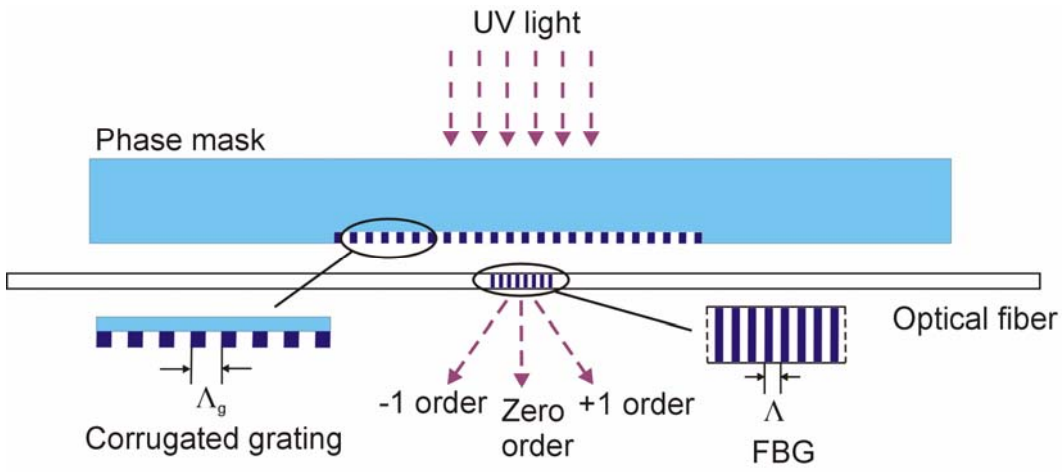

Figure 2.3: Phase-mask technique for a fiber Bragg grating fabrication

Inscription of a BG in a polymer optical fiber requires more rigorous fabrication techniques because of its much higher UV absorption rate [6].

Since formation of a permanent BG in a glass optical fiber was first demonstrated by Hill et al. [4], BG-integrated fibers and other waveguides have been among the key components in photonics systems. They have been used widely for filtering, switching, and stabilizing optical signals in telecommunication applications such as Wavelength Division Multiplexing/ Demultiplexing (WDM) and Optical Add-Drop Multiplexing (OADM) [5]. With their simplicity and unique filtering characteristics, BGs have also been used as narrow band reflectors in wavelength stabilized lasers, fiber lasers, and pump amplifiers [2, 5]. More recently, FBG sensors have been proposed as future medical sensor systems to measure temperatures during medical procedures [7-11]. A FBG is dielectric, and thus unlike thermocouples, thermistors and other conventional temperature measuring electronic devices, is immune to electromagnetic interference.

Polymer BGs have been proposed as passive filters [12-14], tuning filters [15, 16], WDM systems [1, 17-19] and couplers [20]. A very narrow spectral bandwidth of ~ 0.2

nm at 1550 nm was demonstrated using passive polymer BG filters with uniform grating periods [12], and an even narrower band of 0.03 nm at 1290 nm was demonstrated using phase shifted BG filters [13]. Polymer BGs have also been demonstrated as filters in WDM systems for short haul data transmission with a wavelength tolerance of 0.2 ~ 0.5 nm/K [1, 15]. As a future solution for an economical multiplexing system, polymer BG-based optical add/drop multiplexers (OADM's) were introduced with a channel spacing of 400 GHz (3.2 nm) and a thermal stability of 0.04 nm/K [19].

2.2 Basic Optical Principles

The axial refractive index modulation in a BG is typically represented in sinusoidal form [21], as illustrated in Figure 2.4 and expressed in Eq. (2.1)

$$\delta n_{eff}(z) = \overline{\delta n_{eff}(z)}\left[1 + \cos\left(\frac{2\pi z}{\Lambda} + \phi(z)\right)\right] \tag{2.1}$$

where $\delta n_{eff}(z)$ is the modulation of the effective refractive index, $\overline{\delta n_{eff}(z)}$ is the average modulation of the effective refractive index, Λ is the grating period, and $\phi(z)$ is a grating chirp, i.e., the inherent or fabrication tolerance related to non-uniformity in the grating period.

As light is incident on the fiber, entering from the left in Figure 2.4, the refractive index modulation results in the reflection of a narrow bandwidth of light, centered around the Bragg wavelength, λ_B.

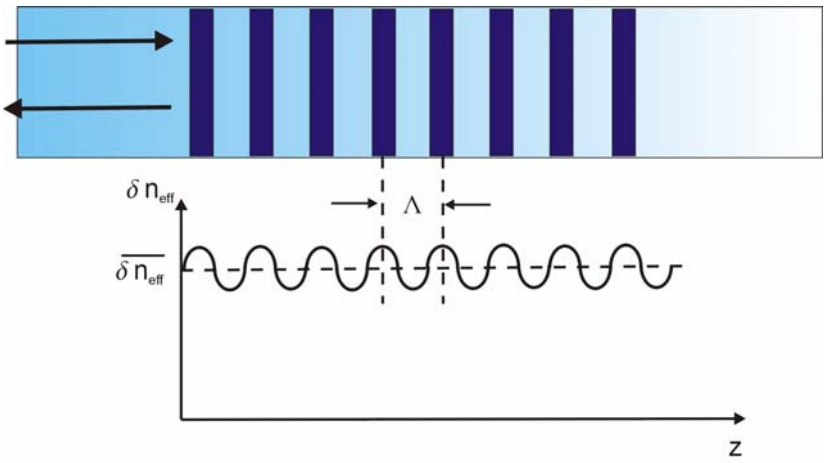

Figure 2.4: Refractive index modulation along a Bragg grating

This characteristic wavelength is determined by the effective refractive index and the grating period, and can be defined as [21]

$$\lambda_B = 2n_{eff}\Lambda \tag{2.2}$$

where n_{eff} is the effective refractive index, combining the contributions of the waveguide and the cladding.

The intrinsic optical parameters of the FBG include the refractive indices of the fiber core and the cladding (n_{co} and n_{cl}), the index modulation ($\overline{\delta n_{eff}(z)}$), and the grating period (Λ). From these intrinsic parameters, working through several defined optical parameters, the effective refractive index (n_{eff}), Bragg wavelength (λ_B), coupling coefficient (κ) (relating to the interaction between the incident and reflected waves in the BG), and maximum reflectivity ($\rho_{\max}$) can be determined.

For single mode operation, the Numerical Aperture, *NA* is defined [22] as

$$NA = \sin\phi_{\max} = \sqrt{n_{co}^2 - n_{cl}^{\ 2}} \tag{2.3}$$

where $\phi_{\max}$ is the critical angle (or the maximum incident angle for total internal reflection).

To assure single mode operation [22], the generalized frequency, V, defined in Eq. (2.4), must be maintained below 2.4048 [22] as

$$V = \frac{2\pi r_{co}}{\lambda} NA < 2.4048 \tag{2.4}$$

where r_{co} is the core radius.

This leads to a relation for the generalized guide index, b, given by Eq. (2.5)

$$b = \left(1.1428 - \frac{0.996}{V}\right)^2 \tag{2.5}$$

Reflecting the combined effects of the numerical aperture, guide index, and cladding refractive index, the effective index of refraction, n_{eff}, can be expressed as [22]

$$n_{eff} = \sqrt{b \cdot (NA)^2 + n_{cl}^2} \tag{2.6}$$

Substituting Eq. (2.2) through (2.5) into Eq. (2.6) and rearranging the terms, the n_{eff} relation takes the following form

$$\left(1 - \frac{0.996^2}{(\pi r_{co})^2}\Lambda^2\right) n_{eff}{}^2 + 2.2765 \frac{\Lambda \cdot NA}{\pi r_{co}} n_{eff} - n_{cl}{}^2 - (1.1428)^2 NA^2 = 0 \tag{2.7}$$

where single mode operation dictates that the solution of Eq. (2.7) for the effective index must also satisfy the following relationship: $n_{eff} > \frac{\pi \cdot r_{co} NA}{2.4048 \cdot \Lambda}$.

Using the intrinsic parameters (r_{co}, n_{co}, n_{cl}, and Λ) of a FBG, the effective index of the FBG can be found using Eq. (2.7).

For a single mode BG [23, 24], the coupling coefficient, κ is defined as

$$\kappa = \frac{\pi}{\lambda}\overline{\delta n_{eff}} \tag{2.8}$$

Then, the maximum reflectivity, produced at the Bragg resonance condition, is

$$\rho_{\max} = \tanh^2\left(\kappa_B L\right) \tag{2.9}$$

where L is the total grating length (Figure 2.1) and κ_B is the coupling coefficient at the Bragg wavelength, λ_B.

Chapter 3

First Order Thermo-Optical Modeling of Polymer Bragg Grating

3.1 Thermo-Optical Model

3.1.1 Introduction

Due to the sensitivity of the optical and mechanical properties of the optical polymers, as well as the physical dimensions of the grating, to temperature and stress, any temperature variance and stress change can affect the refractive index and the grating period and lead to a shift in the Bragg wavelength of the grating. For an isotropic BG with modest changes in temperature and stress, these individual effects can be superimposed to yield the Bragg wavelength shift [25].

$$\frac{\Delta\lambda_B}{\lambda_B} = \frac{\Delta n_{eff}}{n_{eff}} + \frac{\Delta\Lambda}{\Lambda} \tag{3.1}$$

where $\frac{\Delta n_{eff}}{n_{eff}}$ and $\frac{\Delta\Lambda}{\Lambda}$ represent the changes in the index of refraction and the grating pitch.

The total index shift caused by the temperature and stress change can be superposed as [25]

$$\Delta n_{eff} = \Delta n_{eff}^{\Delta T} + \Delta n_{eff}^{\sigma} \tag{3.2}$$

where $\Delta n_{eff}^{\Delta T}$ and Δn_{eff}^{σ} are the index shifts caused by the temperature and stress change, respectively.

By similarity to a glass optical waveguide, it can be expected that – despite their small differences in the index of refraction – the core and the cladding would be similar in other optical properties. Consequently, the derivative of the effective index of a BG

with respect to temperature can be taken equal to the *dn/dT* of the waveguide core material and the change in the effective index of refraction for the grating expressed as

$$\Delta n_{eff}^{\Delta T} = \frac{dn}{dT}\Delta T \tag{3.3}$$

where *dn/dT* is the thermo-optical coefficient, and ΔT is the temperature change of the BG relative to an appropriate reference temperature. Typical values for *dn/dT* for glassy polymers range from -100 to -200 x 10^{-6}/K [26], leading to an approximately 0.07% to 0.14% decrease in the index of refraction for a 10K increase in temperature. These are 10 to 20 times greater in magnitude, though opposite in sign, than those for glass fibers.

3.1.2 Photoelastic effect

The stress imposed or developed in an optical material creates a change in the refractive index and it results in an optically anisotropic behavior, which is commonly referred to as the photoelastic effect.

For an isotropic grating, a stress-induced index shift can be expressed as [25]

$$\Delta n_{eff}^{\sigma} = \frac{-n^3}{2}\left[p_{12}\varepsilon_1^{\sigma} + (p_{11} + p_{12})\frac{\varepsilon_2^{\sigma} + \varepsilon_3^{\sigma}}{2} \right] \tag{3.4}$$

where ε_1^{σ}, ε_2^{σ}, and ε_3^{σ} are stress-induced principal strains along the axes 1, 2, and 3 as shown in Figure 3.1 , and p_{11} and p_{12} are strain optical constants.

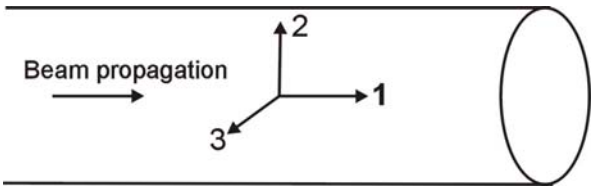

Figure 3.1: Principal axes in an optical fiber

For the uni-axial stress state along the axis '1', principal strains to the axes, '2' and '3' can be rewritten in the form of

$$\varepsilon_2^\sigma = \varepsilon_3^\sigma = -\nu\varepsilon_1^\sigma \tag{3.5}$$

where v is Poisson's ratio.

Substituting Eq. (3.5) into (3.4), the stress-induced refractive index shift associated with the uni-axial stress in the axial direction can be determined as [25]

$$\Delta n_{eff}^\sigma = -P_{eq}\varepsilon^\sigma n_{eff} \tag{3.6}$$

where ε^σ , the rewritten form of ε_1^σ , is the stress-induced strain along the axis '1', and the equivalent photoelastic constant, $P_{eq,}$ is related to the strain optical constants, p_{11} and p_{12} [25] as

$$P_{eq} = \frac{n^2}{2}[p_{12} - \nu(p_{11} + p_{12})] \tag{3.7}$$

These strain optical constants can be obtained in the form of stress optical constants, C_1 and C_2 [27-30]

$$p_{11} = \frac{2E[C_1(1-\nu) + 2\nu C_2]}{n^3(2\nu^2 + \nu - 1)} \tag{3.8}$$

$$p_{12} = \frac{2E[\nu C_1 + C_2]}{n^3(2\nu^2 + \nu - 1)} \tag{3.9}$$

For optical polymers P_{eq} varies from 0.06 to 0.12 [26], [31-32], resulting in an approximately 0.006% to 0.012% decrease in the index of refraction for a 0.001 increase in stress-induced strain. Interestingly, P_{eq} for glass fiber (0.22) [2] is about 2 to 4 times greater than those for optical polymers.

3.1.3 Strain effect

The relative change of the grating period due to the thermal expansion and the stress-induced strain is given as

$$\frac{\Delta\Lambda}{\Lambda} = \alpha\Delta T + \varepsilon^{\sigma} \tag{3.10}$$

where α is the coefficient of thermal expansion (CTE).

For optical polymers, CTEs vary from 60 to 80×10^{-6} K^{-1}[26] leading to a 0.06% to 0.08% increase in grating pitch change for a 10K increase in temperature. 0.001 increase in the stress-induced strain causes 0.1% increase in the grating pitch change. 0.16% -0.18% increase in grating pitch change would encounter for a 10K increase in temperature with a 0.001 increase in the stress-induced strain. The CTE for a typical glass fiber is 0.55×10^{-6} K^{-1} [26] resulting in nearly two orders of magnitude smaller increase in grating pitch than those with optical polymers for a 10K increase in temperature.

3.1.4 Bragg wavelength shift

Linear Superposition: Returning to Eq. 3.1, for optical polymers, a 10K increase in temperature and a 0.001 increase in stress-induced strain result in individual shifts in Bragg wavelengths; -1 nm to -2.1 nm by the thermally-driven index shift, 2.5 nm to 2.8 nm by the grating pitch change and -0.1 nm shift for the stress-driven index shift. Consequently, the total shift in Bragg wavelength ranges from 0.3 nm to 1.7 nm. For a glass optical fiber associated with equivalent changes in temperature and stress-induced strain, 0.1 nm, 1.5 nm, and -0.2 nm shifts in Bragg wavelengths are caused by the thermally-driven index shift, the grating pitch change, and the stress-driven index shift, respectively. As a result, the total shift is 1.4 nm. It may thus be seen that while the overall Bragg wavelength shift for typical optical polymers may be of the same

magnitude of the commonly used glass fibers, the individual components of the Bragg shift may be relatively large.

Quadratic Relation: To improve the accuracy with which the Bragg shift is calculated, it is appropriate to return to Eq. (2.2) and observe that the shifted Bragg wavelength, λ_{B2}, can be written as

$$\lambda_{B2} = 2n_{eff_2}\Lambda_2 = 2\left(n_{eff_1} + \Delta n_{eff}\right)\left(\Lambda_1 + \Delta\Lambda\right) \tag{3.11}$$

where subscript '1' denotes the initial state before the temperature change and the stress.

Substituting Eqs. (3.3), (3.6), and (3.10) into (3.11), one can get

$$\lambda_{B2} = 2\left(n_{eff_1} + \frac{dn}{dT}\Delta T - n_{eff_1}P_{eq}\varepsilon^{\sigma} \right)\left[\Lambda_1 + \Lambda_1\left(\alpha\Delta T + \varepsilon^{\sigma}\right)\right] \tag{3.12}$$

Subtracting the expression for the initial Bragg wavelength, λ_{B1}, the Bragg wavelength shift, $\Delta\lambda_B$, can be expressed as

$$\Delta\lambda_B = \lambda_{B1}\left\{\begin{array}{l}\left(\frac{1}{n_{eff_1}}\frac{dn}{dT}\Delta T\right) + \left(-P_{eq}\varepsilon^{\sigma}\right) + \left(\alpha\Delta T + \varepsilon^{\sigma}\right) \\ + \left[\left(\frac{1}{n_{eff_1}}\frac{dn}{dT}\Delta T\right)\left(\alpha\Delta T + \varepsilon^{\sigma}\right)\right] + \left[\left(-P_{eq}\varepsilon^{\sigma}\right)\left(\alpha\Delta T + \varepsilon^{\sigma}\right)\right]\end{array}\right\} \tag{3.13}$$

The shift of Bragg wavelength induced by the individual effect can be predicted by de-coupling Eq. (3.13). The Bragg wavelength shift associated with the thermally-induced index change can be expressed as

$$\Delta\lambda_B{}^{\Delta n_{eff}^{\Delta T}} = \lambda_{B1}\left(\frac{1}{n_{eff_1}}\frac{dn}{dT}\Delta T\right) \tag{3.14}$$

The Bragg wavelength shift associated with the stress-induced index change, i.e. photoelastic effect, can be predicted as

$$\Delta\lambda_B^{\Delta n_{eff}^{\sigma}} = \lambda_{B1}\left(-P_{eq}\varepsilon^{\sigma}\right) \tag{3.15}$$

The Bragg wavelength shift resulting from the grating pitch change can be written as

$$\Delta\lambda_B^{\Delta\Lambda} = \lambda_{B1}\left(\alpha\Delta T + \varepsilon^{\sigma}\right) \tag{3.16}$$

The Bragg wavelength shift produced by the product of the thermally-induced index shift and the grating pitch change can be expressed as

$$\Delta\lambda_B^{\Delta n_{eff}^{\Delta T}\cdot\Delta\Lambda} = \lambda_{B1}\left(\frac{1}{n_{eff_1}}\frac{dn}{dT}\Delta T\right)\left(\alpha\Delta T + \varepsilon^{\sigma}\right) \tag{3.17}$$

Finally, the Bragg wavelength shift resulting from the product of the stress-induced index shift and the grating pitch change can be predicted as

$$\Delta\lambda_B^{\Delta n_{eff}^{\sigma}\cdot\Delta\Lambda} = \lambda_{B1}\left(-P_{eq}\varepsilon^{\sigma}\right)\left(\alpha\Delta T + \varepsilon^{\sigma}\right) \tag{3.18}$$

In a BG inscribed in a glass optical material, e.g. a fiber Bragg grating (FBG), the 4th and 5th terms in Eq. (3.13) would be negligible due to the low CTE (~ 0.55 x 10^{-6}/K) of the glass BG when the temperature change and the stress-induced strain are not extreme, i.e., the temperature change up to the glass transition temperature and the stress-induced strain below 1%. However, for typical optical polymer materials, the thermal expansion coefficient can be expected to range from 60 to 80 x 10^{-6}/K [26]. It may, thus, be seen that for polymer optical waveguides, the effects of the thermally-induced changes of the index and the grating pitch on the Bragg wavelength shift are relatively large and of the same order of magnitude, but opposite in sign. Care must be taken in evaluating the net Bragg wavelength shift using Eq. (3.13).

To investigate the importance of two product terms shown in Eqs. (3.17) and (3.18) for predicting the net Bragg wavelength shift, individual and net shifts for a glass BG and a polymer BG for the temperature increase, ranging from 0 K to 50 K, and a

stress-induced strain of -0.01% were calculated. Figures 3.2 and 3.3 present individual and total $\Delta\lambda_B$, respectively. An initial Bragg wavelength of 1550 nm and n_{eff} of 1.5 were used for the calculation, and 1×10^{-5} K^{-1} and -1×10^{-4} K^{-1} for *dn/dT*, 0.55 $\times10^{-6}K^{-1}$ and 70 $\times10^{-6}K^{-1}$for CTE, 0.1 and 0.22 for P_{eq} were used for the properties of a glass BG and a polymer BG, respectively.

Figures 3.2(a) and (b) show that each $\Delta\lambda_B$, induced by thermally-driven index shift and grating pitch change for the glass BG is just 10% and 1% to that for the polymer BG, and much smaller dn/dT and CTE for the glass BG can explain this. It may be seen that $\Delta\lambda_B$ by two coupled-effects as well as a photoelastic effect are much smaller than other individual shifts.

Figures 3.3(a) and (b) present the net $\Delta\lambda_B$, predicted by two equations (3.1 and 3.13), for the glass and polymer BGs. The results show considerable discrepancies up to 30% for the polymer BG while net $\Delta\lambda_B$, predicted by two different ways, for the glass BG are found to be almost identical with discrepancies below 0.5%. Hence, Figure 3.3(b) demonstrates that $\Delta\lambda_B$ created by two coupled-effects; the thermally-induced index shift and the grating pitch change, the stress-induced index shift and the grating pitch change; should be considered to precisely predict the net $\Delta\lambda_B$ of a polymer BG.

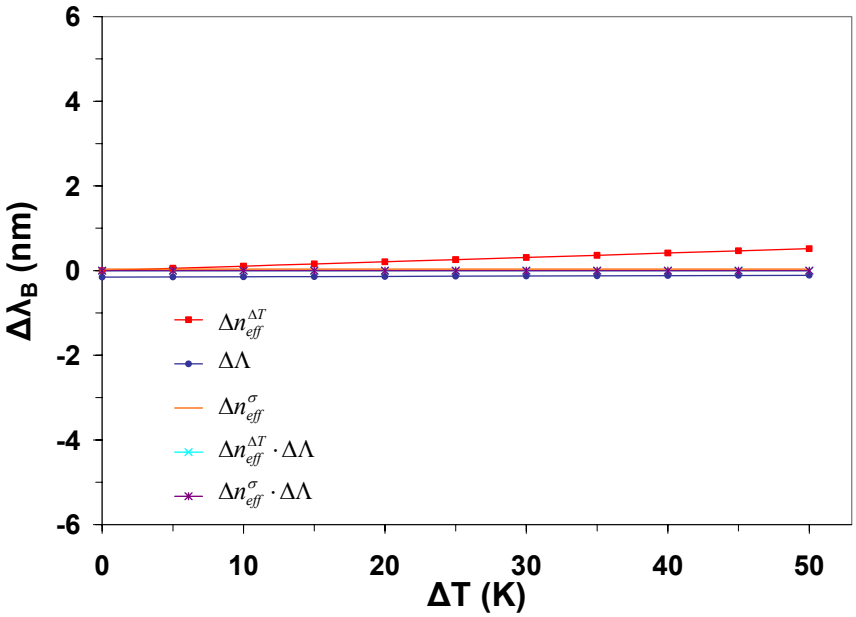

(a)

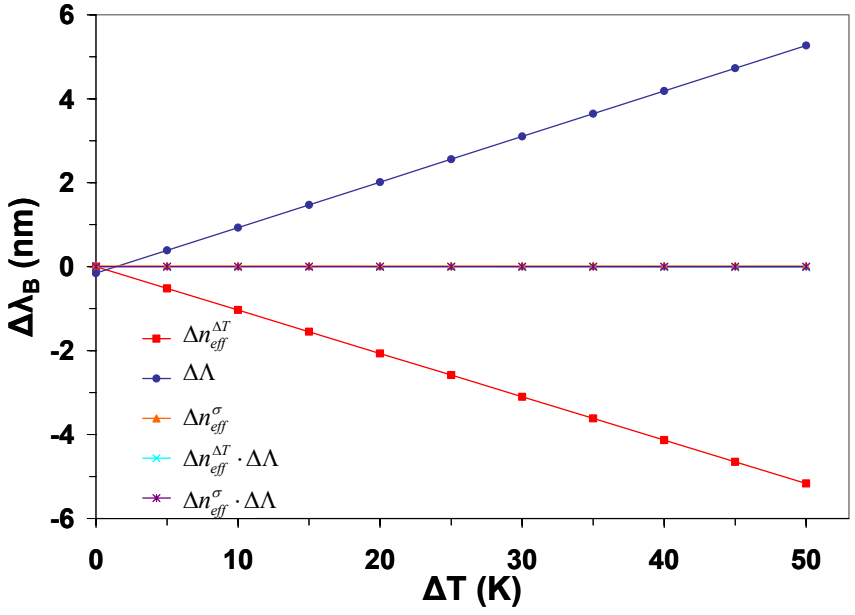

(b)

Figure 3.2: Individual Bragg wavelength shifts of (a) a glass Bragg grating (b) a polymer Bragg grating for the temperature increase varying from 0 K to 50 K and a stress-induced strain of -0.01%

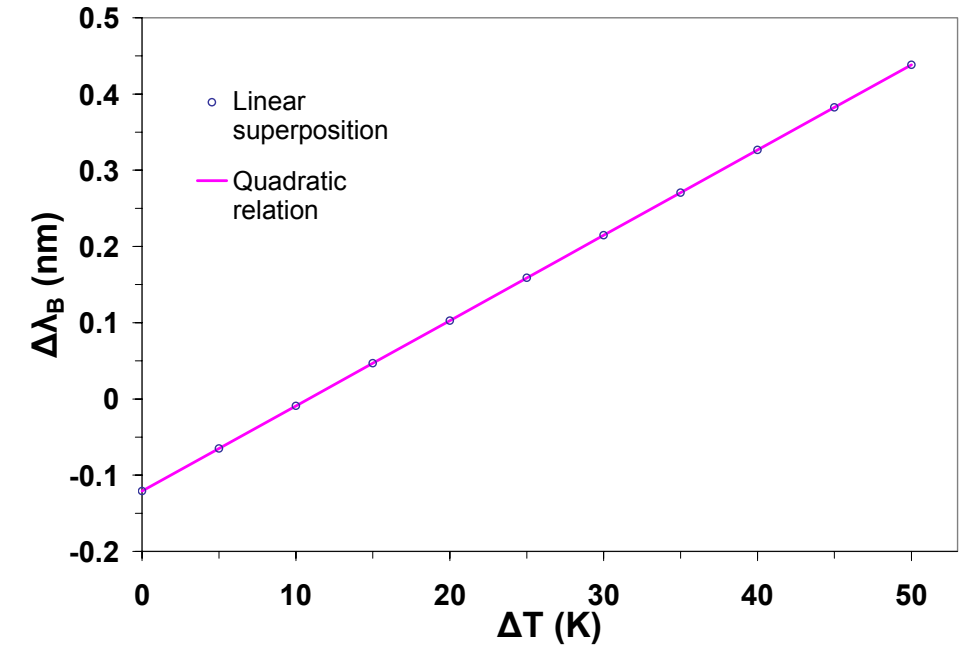

(a)

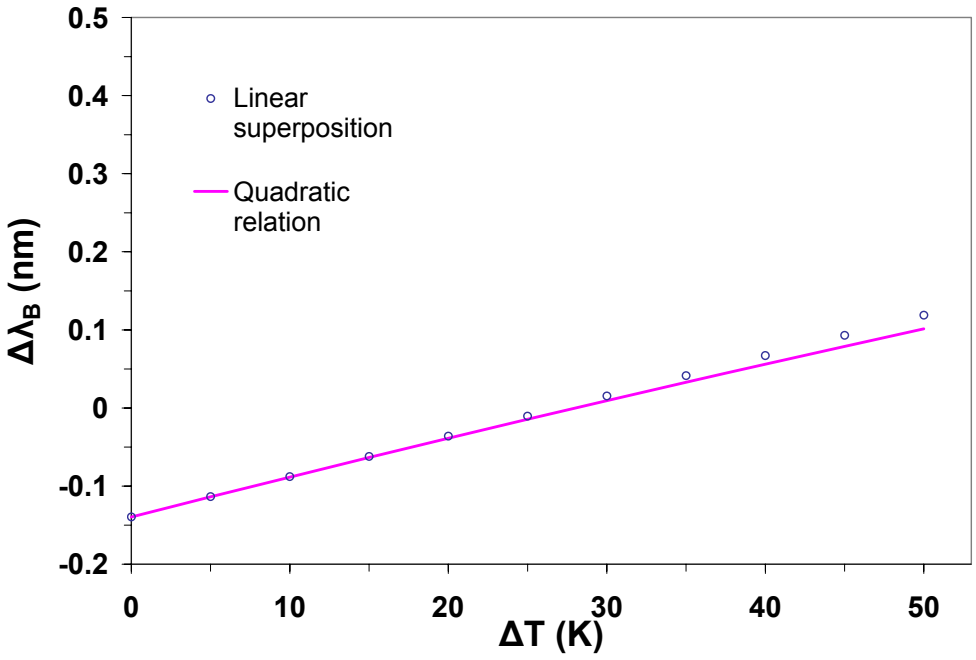

(b)

Figure 3.3: Total Bragg wavelength shifts of (a) a glass Bragg grating (b) a polymer Bragg grating for a temperature increase varying from 0 K to 50 K and a stress-induced strain of –0.01%

3.2 Analytical Thermal Model

A typical structure of a polymer Bragg grating waveguide is shown in Fig. 3.4. The Bragg grating is inscribed on the core of the waveguide, which is mechanically supported by the upper and lower claddings. A substrate supports the claddings and the core of the waveguide. The waveguide core typically has a rectangular shape, and the inscribed grating is a planar Bragg grating.

The axial distribution of the optical power, induced by the Bragg grating, along the waveguide core is expected to be significant only near the Bragg resonance, and it is expected that the spectral region strongly affected by the Bragg grating will be a very small fraction of the total spectrum of the broad band light source. Hence, for broadband illumination, the effect of the Bragg grating on the optical power distribution along the waveguide core can be assumed to be negligible.

Light incident on the waveguide core experiences a loss of intensity due to absorption, scattering, and reflection [5]. Assuming the extrinsic optical loss is negligible relative to the intrinsic absorption loss and – for simplicity - considering only the axial variation, without the lateral and transversal variances, in the optical power, the axial optical power, $P(z)$, along the waveguide can be expressed by Beer's law in the form of Eq. (3.19) [24].

$$P(z) = P_{inc} \exp(-\hat{a} \cdot z) \tag{3.19}$$

where P_{inc} and $\hat{a}$ are incident optical power and absorption coefficient, respectively.

Thus, the heat generated in the waveguide by the intrinsic light energy absorption, $q'(z)$, can be determined by the product of the absorption coefficient and the local power, determined from Beer's law.

$$q'(z) = \hat{a} \cdot P_{inc} \exp(-\hat{a} \cdot z) \tag{3.20}$$

The total heat generated in the waveguide can be obtained by integrating Eq. (3.20) over the length, i.e.

$$q = \int_0^{L_c} \hat{a} \cdot P_{inc} \cdot e^{-\hat{a}z} dz \tag{3.21}$$

where L_c is the total length of the waveguide core.

For simplicity, steady state conditions are assumed. The polymer BG waveguide is sitting on the low conductive package. Hence, the bottom surface of the substrate is assumed to be insulated, and other surfaces are assumed to be passively cooled by natural convection and radiation.

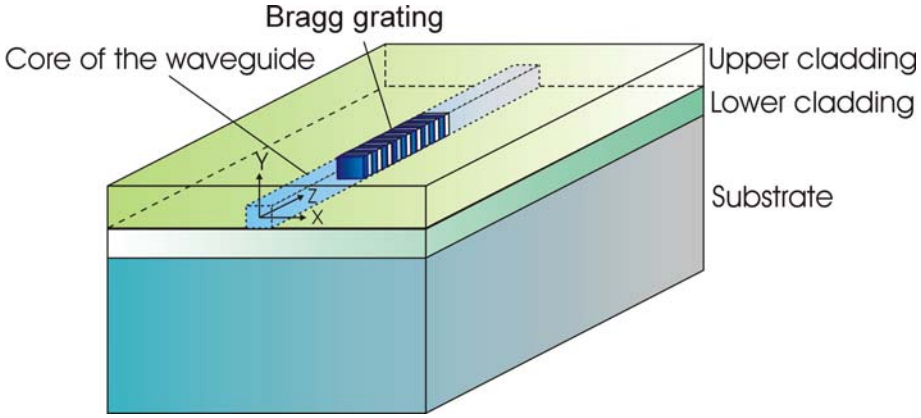

Figure 3.4: The structure of a polymer Bragg grating waveguide

Heat generated in the waveguide can flow directly to the top surface through the upper cladding (the R_{cTop} and R_{Topa} branch in Figure 3.5) or into the substrate through the lower cladding. Due to the small thickness of the claddings, heat spreading in these layers can be ignored [33]. The thermal resistance of the path leading from the waveguide to the substrate, including conduction through the lower cladding and spreading in the substrate, facilitated by the large ratio of substrate depth to waveguide width, can be expressed as

$$R_{cs} = \frac{1}{\pi L_s k_s} \ln\left[\frac{1}{\sin(\pi r_c / 2r_s)}\right] \tag{3.22}$$

where R_{cs} is based on a long strip heat source conducting into a thick rectangular substrate [33], L_s is the total length of the substrate, r_c and r_s are the half- width of the waveguide core and the substrate, respectively, and k_s is the thermal conductivity of the substrate.

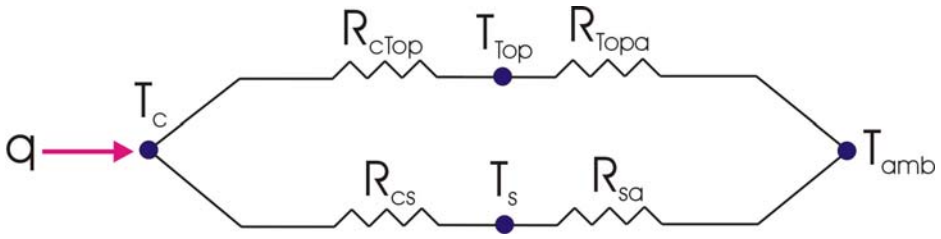

Figure 3.5: Thermal resistance model of a polymer Bragg grating waveguide

With the passively-cooled boundary condition, the Biot number (= *hL/k*) for the substrate is expected to be less than 0.1 for the relatively small dimensions of the substrate. Therefore, it is reasonable to assume that the waveguide substrate is isothermal.

This assumption leads to completion of the thermal resistance model of Figure 3.5 by just adding the external convective resistance, R_{sa}, which accounts for heat flow from all the exposed surfaces except the bottom surface of the substrate as

$$R_{sa} = 1/(hA_s) \tag{3.23}$$

where h is the heat transfer coefficient including both radiation and convection, and A_s is the total area of the exposed surfaces except the bottom surface of the substrate. The resulting thermal resistance, R_{cua} through the upper cladding is now given by

$$R_{cua} = R_{cTop} + R_{Topa} \tag{3.24}$$

R_{cTop} is the conductive resistance from the waveguide core to the top surface of the upper cladding and can be expressed as

$$R_{cTop} = \frac{\Delta x_{cT}}{k_c A_c} \tag{3.25}$$

where Δx_{cT} is the distance from the waveguide core to the top surface to the upper cladding, k_c is the thermal conductivity of the waveguide core, and A_c is the cross sectional area of the waveguide core. Due to the tiny thickness of the upper cladding, heat spreading in the upper cladding would be negligible, and hence, the heat may flow through the small area, approximated to be A_c, to the top surface.

R_{Topa} is the convective resistance from the top surface of the waveguide core to the ambient and can be expressed as

$$R_{Topa} = \frac{1}{hA_c} \tag{3.26}$$

It should be noted that the area for the heat transfer through the top surface of the upper cladding to the ambient is selected to be the same as the cross sectional area of the waveguide core.

The resistance of the path that proceeds through the lower cladding, R_{cla} can be expressed as

$$R_{cla} = R_{cs} + R_{sa} \tag{3.27}$$

, which yields a total resistance, R_T as

$$R_T = (R_{cua}{}^{-1} + R_{cla}{}^{-1})^{-1} \tag{3.28}$$

The specified thermal resistance is used to determine the average excess temperature of the core of the waveguide as

$$\Delta T_c = qR_T \tag{3.29}$$

Thermal resistance through the upper cladding is expected to be extremely high due to the tiny area associated with the heat transfer to the ambient. Thus, heat flow through the upper cladding would be negligible, and average excess temperature of the substrate can be obtained by Eq. (3.30).

$$\Delta T_s = q_{sa} \cdot R_{sa} \tag{3.30}$$

where q_{sa} is heat flow through the substrate to the ambient.

3.3 Analytical Thermo-Structural Model

Since the waveguide and the claddings are thin and assumed to have identical mechanical properties, the polymer Bragg grating waveguide can be considered as a two layer mechanical system; a thin film on a thick substrate (see Figure 3.6). The solutions developed in Ref. [34] are employed to determine the axial stress and strain in the waveguide. The total strain, ε_f, or the axial displacement gradient, du_f / dz', in the waveguide can be expressed as

$$\varepsilon_f = \frac{du_f}{dz'} = \alpha_f \Delta T_f + [(\gamma_f - \psi_f \beta^2) \frac{\cosh(\beta z')}{\cosh(\beta L_s / 2)} - \gamma_f] \times E_{of} t_f [\alpha_f \Delta T_f - \alpha_s \Delta T_s] \tag{3.31}$$

where u_f is the axial displacement of the film, and z' is the axial coordinate, as shown in Figure 3.6. The symbols α_f and α_s represent the thermal expansion coefficients (CTEs), and ΔT_f and ΔT_s are excess temperatures (or the temperature rise relative to the reference temperature), for the film and the substrate, respectively. The first term in Eq. (3.31) represents the thermal expansion of the film, and the second term does the effect of the substrate on the local axial displacement of the film.

A characteristic constant, β which satisfies the displacement compatibility of the film and the substrate is defined as

$$\beta = \sqrt{\gamma / \psi} \tag{3.32}$$

where γ and ψ are the total axial and interfacial compliances. The total axial compliance can be expressed as

$$\gamma = \gamma_f + \gamma_s \tag{3.33}$$

The coefficients of axial compliance for the film and the substrate, γ_f and γ_s, are defined as

$$\gamma_f = \frac{1}{E_{of} t_f} \tag{3.34}$$

$$\gamma_s = \frac{1}{E_{os} t_s} \tag{3.35}$$

where $E_{of} = E_f/(1-\nu_f)$ and $E_{os} = E_s/(1-\nu_s)$ are generalized Young's moduli, ν_f and ν_s are the Poisson's ratios, and E_f and E_s are the Young's moduli, t_f and t_s are the thickness of the film and the substrate, respectively.

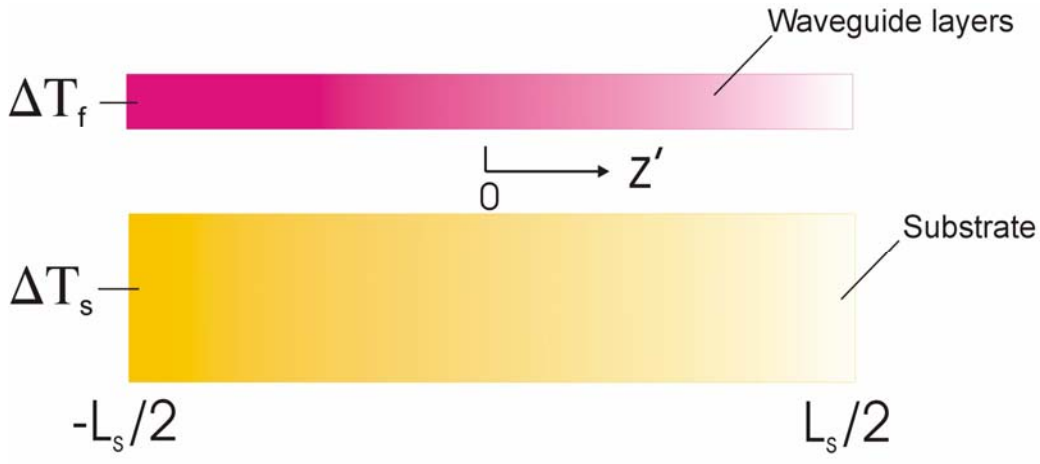

Figure 3.6: Schematic of the thermo-structural model of a waveguide

The total interfacial compliance can be expressed as

$$\psi = \psi_f + \psi_s \tag{3.36}$$

In Eq. (3.36), ψ_f and ψ_s are the coefficients of interfacial compliances for the film and the substrate, and are defined as

$$\psi_f = 2/3(1+\nu_f)/(1-\nu_f)t_f / E_{of} \tag{3.37}$$

$$\psi_s = 2/3(1+\nu_s)/(1-\nu_s)t_s / E_{os} \tag{3.38}$$

Then the axial stress, σ_f, in the film can be defined as

$$\sigma_f(z') = -E_{of}[\alpha_f \Delta T_f - \alpha_s \Delta T_s]\left[1 - \frac{\cosh(\beta z')}{\cosh(\beta L_s/2)}\right] \tag{3.39}$$

3.4 FEA Thermo-Structural Model

A three-dimensional thermo-structural, finite-element model was developed using a commercial code, ANSYS 7.0, [35,36] to obtain the detailed temperature, strain, and stress field. The steady state heat conduction equation with heat generation (volumetric heat source) is employed as the governing equation [35-37] to calculate the temperature field in the 3-D FEA model.

$$\frac{\partial}{\partial x}(k\frac{\partial T}{\partial x}) + \frac{\partial}{\partial y}(k\frac{\partial T}{\partial y}) + \frac{\partial}{\partial z}(k\frac{\partial T}{\partial z}) + q_G = 0 \tag{3.40}$$

where T, k and q_G are temperature, thermal conductivity and the volumetric heat generation rate, respectively.

In this model, thermo-elastic stress and strain relationships in rectangular coordinates, as shown in Eqs. (3.41) to (3.46), are used to calculate the thermally-induced strain and stress fields in the 3-D FEA model [35-38].

Normal stress to the x direction, σ_{xx}, is defined as

$$\sigma_{xx} = \mu e + 2G\varepsilon_{xx} - (3\mu + 2G)\alpha\Delta T \tag{3.41}$$

where α and ΔT are CTE and temperature difference relative to the reference temperature, respectively, and ε_{xx} and G are normal strain to the x direction and shear modulus, respectively.

Dilatation, e is

$$e = \varepsilon_{xx} + \varepsilon_{yy} + \varepsilon_{zz} \tag{3.42}$$

where ε_{yy} and ε_{zz} are the normal strains in the y and z directions, respectively.

The elastic constant, μ, is expressed in terms of the Poisson's ratio, ν and Young's Modulus, E,

$$\mu = \frac{\nu E}{(1+\nu)(1-2\nu)} \tag{3.43}$$

Normal stress in the y and z directions (σ_{yy} and σ_{zz}) are defined as

$$\sigma_{yy} = \mu e + 2G\varepsilon_{yy} - (3\mu + 2G)\alpha\Delta T \tag{3.44}$$

$$\sigma_{zz} = \mu e + 2G\varepsilon_{zz} - (3\mu + 2G)\alpha\Delta T \tag{3.45}$$

Shear stresses (σ_{xy}, σ_{yz} and σ_{zx}) are defined as

$$\sigma_{xy} = 2G\varepsilon_{xy}; \sigma_{yz} = 2G\varepsilon_{yz}; \sigma_{zx} = 2G\varepsilon_{zx} \tag{3.46}$$

For simplicity, the analytical thermal model assumed a uniform heat generation rate, based on the total intrinsic light energy absorption divided by the volume of the core. However, the spatial power distribution of a typical broad band light source, such as

a Light Emitting Diode (LED), is often represented by a Gaussian radial distribution. Considering the intrinsic absorption associated with a Gaussian light source, the internal heat generation rate in the waveguide core can be expressed by a physically more appropriate Gaussian profile, i.e. .

$$q_G = \frac{2P_{inc}}{\pi\omega_o} \cdot \hat{a} \cdot \exp\left[-\hat{a} \cdot z - \frac{2(x^2 + y^2)}{\omega_o^{\,2}} \right] \tag{3.47}$$

where P_{inc}, $\hat{a}$, and ω_o are an incident optical power, an intrinsic absorption coefficient, and a light beam radius, respectively.

In order to effectively utilize this Gaussian volumetric heat generation rate in the extremely small volume of the waveguide core, a substructuring (global/local modeling) approach was utilized [35,36]. In addition, the sequentially coupled field method [35,36], which enables the use of the temperature field generated by the thermal model for the body load of the structural model, was used to accurately obtain the thermally-induced strain and stress. The flow chart of the combined thermal-structural numerical solution procedure is shown in Figure 3.7.

The obtained temperature and stress/strain solutions are based on the use of 3-D global and local models and 3-D meshes created in half-symmetry, as shown in Figure 3.8(a). W_s, W_c, H_s, and H_c are the widths and the heights for the substrate and the waveguide core, respectively. The dimensions of the global model were set to equal half of the entire waveguide, and – for accuracy - the local model extends beyond the confines of the waveguide core to twice the core height. The heat generation in the core and the boundary conditions were applied to the global thermal model, as shown in Figure 3.8(a), and the temperature field for the entire waveguide was obtained. The temperature field,

generated by the global thermal model, was used as the external boundary conditions for the local thermal model associated with the Gaussian heat generation rate (see Figure 3.8 (b)). For the structural global analysis, the temperature field obtained from the global thermal model was applied as a thermal loading (sequentially coupled field method) and the displacements were calculated. For the local structural analysis, the displacement field obtained from the global structural model was used as the boundary conditions, and the temperature distribution obtained from the local thermal model was employed as the thermal load (sequentially coupled field method), as shown in Figure 3.8(b).

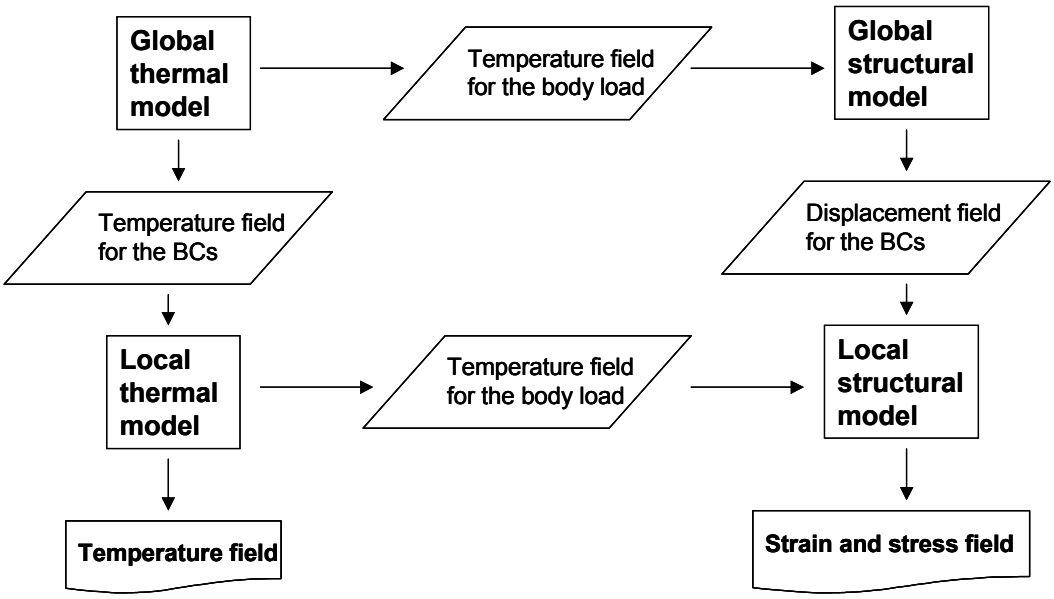

Figure 3.7: Flowchart of 3-D FEA analysis

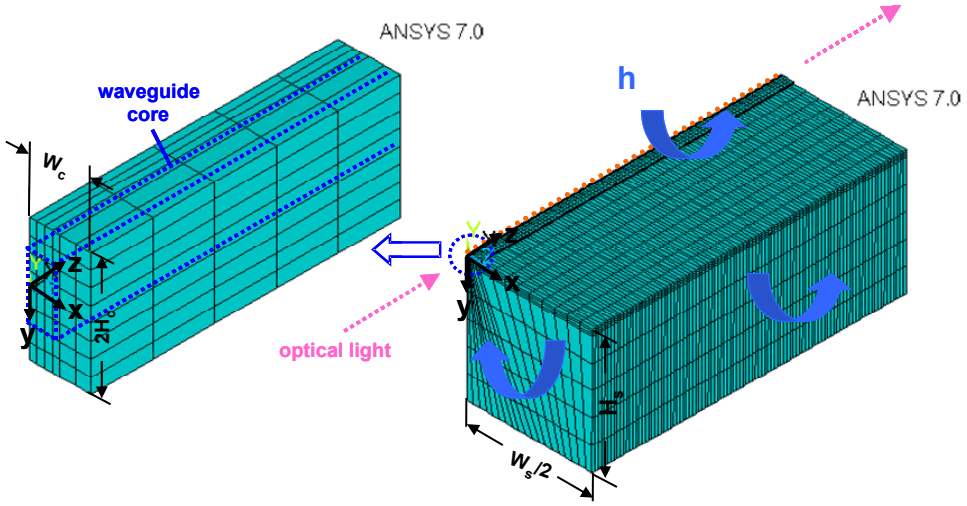

(a)

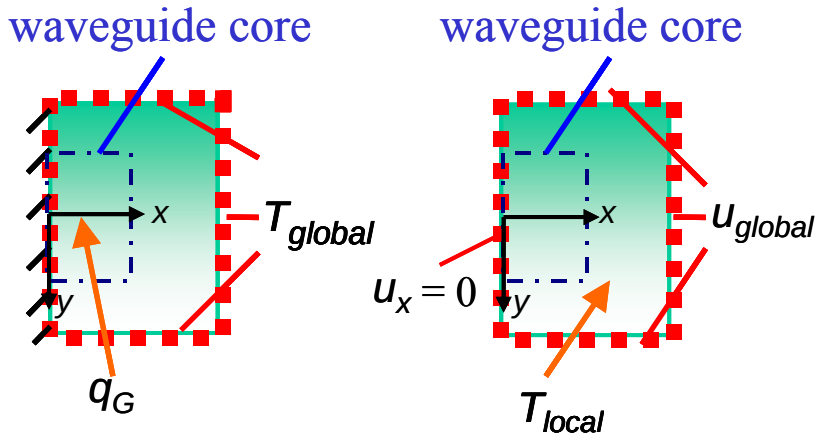

(b)

Figure 3.8: (a) 3-D FEA models (global and local) of a waveguide (b) Boundary conditions of 3-D FEA local models

3.5 First Order Thermo-Optical Analysis of PMMA Bragg Grating

3.5.1 Description of PMMA Bragg Grating Waveguide

Polymethylmethacrylate (PMMA) has been widely used in integrated optics systems, specifically as a waveguide material [39, 40], due to its favorable optical characteristic (good transparency in the visible range of wavelengths) and simple fabrication process. However, most bulk polymer materials, including PMMA, have poor optical transmissivity, ranging from 0.1dB/cm to 2dB/cm [1], around 1550 nm compared to silica glass. Recently, new polymeric materials such as Perfluorocyclobutane (PFCB), Polycyanurates, Cytop, and Cyclotene (BCB) have been introduced [41], along with new techniques for doping the classical polymer materials such as PMMA, polyimide, and polysiloxane (PS) with fluorine or chlorine [1] in order to reduce the optical loss of passive polymer materials in this 1550 nm window. Despite the availability of these new polymeric optical materials, doped PMMA is still widely used. Consequently, in this study, the core of the waveguide, as well as the upper and lower claddings, is assumed to be PMMA, and for the simplicity, all the layers are assumed to possess the same mechanical and thermal properties.

The PMMA Bragg grating waveguide, shown in Figure 3.4, serves as the vehicle for the present modeling and analysis of thermo-optic effects in polymer Bragg gratings. The core of the waveguide is 10×10 μm. The upper and lower claddings are assumed to be 20 μm and 10 μm thick, respectively. A total grating length of 1cm, a maximum reflectivity of 70 %, and Bragg wavelength of 1550 nm are chosen. At this wavelength, the bulk PMMA has an intrinsic absorption coefficient of about 11.513 m^{-1} (0.5 dB/cm) [26]. Two substrate materials, silicon and PMMA, are considered in the analysis to

investigate the effect of the substrate on the thermo-optic behavior of the waveguide. Basic parameters of the PMMA Bragg grating waveguide and the thermal and mechanical properties of the materials used in the analysis are listed in Table 3.1.

Table 3.1: Properties and geometry of a PMMA Bragg grating waveguide

(a) Basic parameters

Parameter	Symbol	Value
Width of waveguide core	W_c	10 μm
Height of waveguide core	H_c	10 μm
Total grating length	L	1 cm
Grating period	Λ	520.8 nm
Width of substrate	W_s	0.4 cm
Height of substrate	H_s	0.2 cm
Length of substrate	L_s	2 cm
Height of upper cladding	H_{ucl}	20 μm
Height of lower cladding	L_{lcl}	10 μm
Bragg wavelength	λ_B	1550 nm
Maximum reflectivity without absorption	ρ'_{max}	0.7
Effective refractive index	n_{eff}	1.488

(b) Material properties of PMMA

Parameter	Symbol	Value
Thermal conductivity	K	0.2 $Wm^{-1}K$
Coefficient of thermal expansion	α	73 x 10^{-6} K^{-1}
Young's modulus	E	3.2 GPa
Absorption coefficient	$\hat{a}$	11.513 m^{-1}
Thermo-optical coefficient	dn/dT	-1.1 x 10^{-4} K^{-1}

(c) Material properties of Si

Parameter	Symbol	Value
Thermal conductivity	k	148 $Wm^{-1}K$
Coefficient of thermal expansion	α	2.5 x 10^{-6} K^{-1}
Young's modulus	E	112.4 GPa

3.5.2 Thermal Analysis

The effects of various incident optical powers and substrate materials (Si and PMMA) on the temperature field of the waveguide were investigated in the subsequent parametric study. Temperatures along the waveguide core were evaluated by the 3-D FE model presented in section 3.4. The heat generation rate, given by Eq. (3.47), was applied to the volume of the waveguide core in the 3-D FE model, and the beam width, ω_o was chosen to be 2.5 μm. The combined convection and radiation heat transfer coefficient, h, on the uninsulated external surfaces of the waveguide was assumed to be 10 $Wm^{-2}K^{-1}$.

In Figures 3.9(a) and (b), present the predicted temperature fields of the entire PMMA waveguide, shown in (a) and the grating in the core of the waveguide, shown in (b) when the incident optical power and the ambient temperature are 0.3 W and 25 °C. It is to be noted that when the PMMA grating is illuminated with 0.3W of light, it can be expected to absorb some 0.03W, for a volumetric heat generation rate of 15kW/cm^3 in the core region. The resulting temperature distribution is quite non-uniform, particularly in the vicinity of the grating or core of the waveguide, where the maximum temperature gradient is nearly 0.6 K/μm. The non-unifomity is also reflected in a temperature difference of roughly 25 K from the waveguide core to the bottom of the substrate. This significant temperature gradient and difference can be explained by the high volumetric heat generation rate and the relatively poor heat spreading in the PMMA substrate.

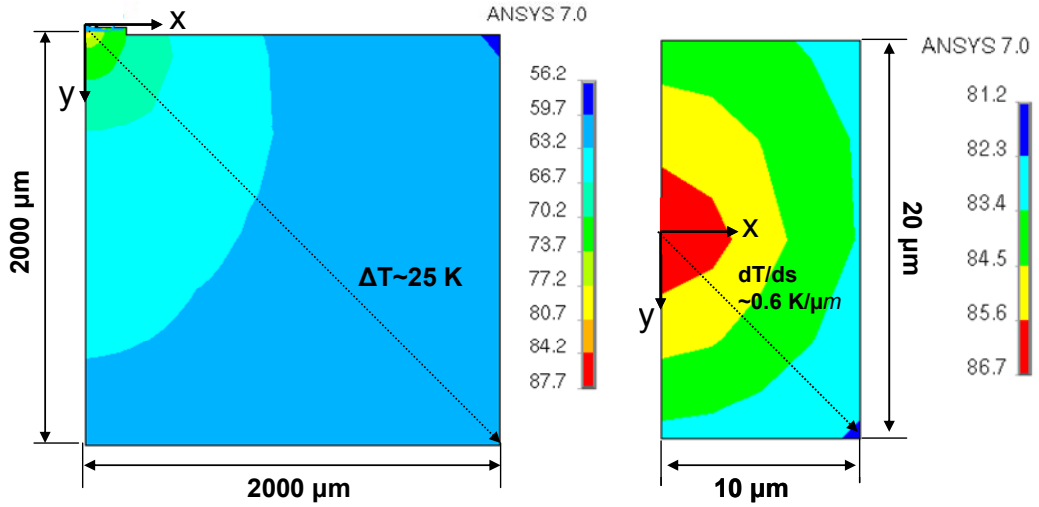

Figure 3.9: Temperature fields of (a) the entire waveguide and (b) the grating in the waveguide core on a PMMA substrate at an incident optical power of 0.3W and an ambient temperature of 25°C

Figure 3.10 shows the excess temperatures along the grating in the waveguide core as well as the core relative to ambient temperature (25 °C) for various incident optical powers. It should be noted that the 1cm long Bragg grating is chosen to be inscribed in the center of the waveguide core to the axial direction (z axis); the grating starts at z =0.5 cm and ends at z =1.5cm along the waveguide core. The temperature variation in a PMMA grating attached to a silicon substrate is nearly negligible, while a grating attached to a PMMA substrate displays a more complex temperature variation and is approximately 20 K warmer than that with the Si substrate at an incident optical power of 0.3 W.

Figure 3.11 presents the average excess temperatures of the substrate and the Bragg grating relative to the reference temperature (25 °C) for various incident optical

powers, i.e. 0.01W to 0.3W. Absorption of these incident powers result in a significant volumetric heat generation rate of 0.5 kW/cm^3 to 15 kW/cm^3 in the core region.

The analytically estimated average temperature rises (excess temperatures), using the previously described thermal network (see Figure 3.5) ,reasonably agrees with the 3-D FEA results with a typical discrepancy of 7%. However, the discrepancy of the analytical prediction for the temperature of the Bragg grating with Si substrate is higher with a maximum discrepancy of 14% than others. This might be explained by lower grating temperatures due to the neglected spreading resistance in the PMMA claddings in the analytical calculation.

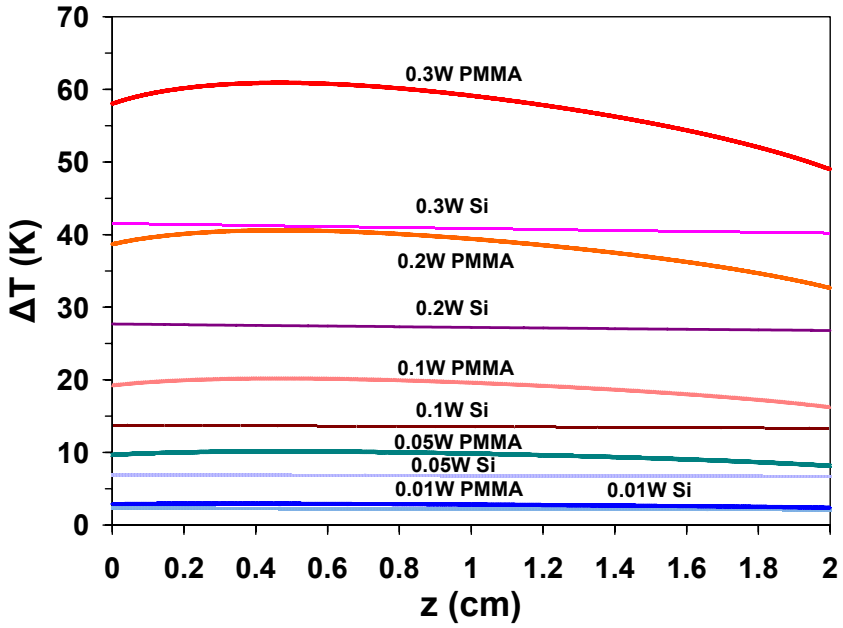

Figure 3.10: Excess temperatures in a PMMA Bragg Grating, associated with PMMA and Si substrate, as well as the waveguide core for various incident optical powers from 0.01W to 0.3W and T_{amb} = 25°C. Bragg grating is inscribed from z= 0.5cm to z=1.5 cm along the waveguide core.

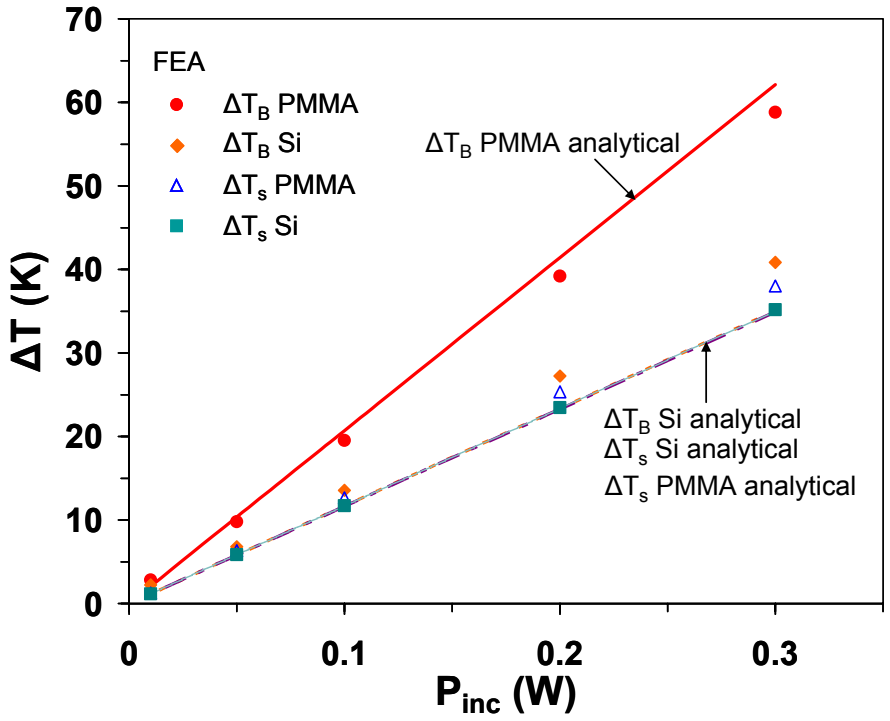

Figure 3.11: Average excess temperatures in the Bragg grating and the substrate of the waveguide for various optical powers from 0.01W to 0.3W (T_{amb} = 25°C)

3.5.3 Thermo-Structural Analysis

Temperatures obtained by the 3-D FE thermal analysis were utilized for the 3-D FE structural model by the sequentially coupled method explained in section 3.4. Thermally-induced strains and stresses in the waveguide core were computed by the substructuring (global/local modeling) approach. Figure 3.12 shows the axial strain (in %) profiles, i.e. the local displacement gradients, in the PMMA grating for the various incident optical powers of 0.01 to 0.3 W and for both the silicon and PMMA substrates. In the polymer

BG on a silicon substrate, the maximum axial strain is approximately 0.009 %, and axial strain is almost uniform at the incident optical power of 0.3 W.

The axial strain in the grating attached to the PMMA substrate is about 30 times greater than that of the Si substrate. This quantitative difference is caused primarily by the difference in the bulk coefficient of thermal expansion (CTE) of silicon (2.5 ppm/K) and PMMA (73 ppm/K). Furthermore, when the polymer BG is attached to a PMMA substrate, a significant axial variation is encountered in the grating temperature and, hence, the local strain shows a more complex profile than that of the grating on a silicon substrate. Other than at the edges, the strain profile follows the temperature profile – which shows a peak and then axially decreasing temperatures. This is much less visible in the case of the silicon substrate due to the nearly uniform grating temperature. Rapidly reducing stress-induced compressive strains in the vicinity of the edges may explain the sharply increasing total strains at the edges.

Equation (3.31) was utilized to verify the FEA predicted axial strains in the waveguide core and the comparison between the numerical and analytical results is shown in Figure 3.12. The discrepancy between the analytical and FEA axial strains is relatively small **(**typically 0.2%**)** for the case involving the silicon substrate and greater **(**typically 7%) for the PMMA substrate. Analytically predicted total strains are very close to the substrate's thermal expansion. The greater discrepancy in the analytical prediction of the PMMA substrate temperature (~7%) may result in the greater difference. In addition, more complicated temperature profiles in the PMMA substrate waveguide might explain this greater discrepancy and a higher degree of non-linearity in strain.

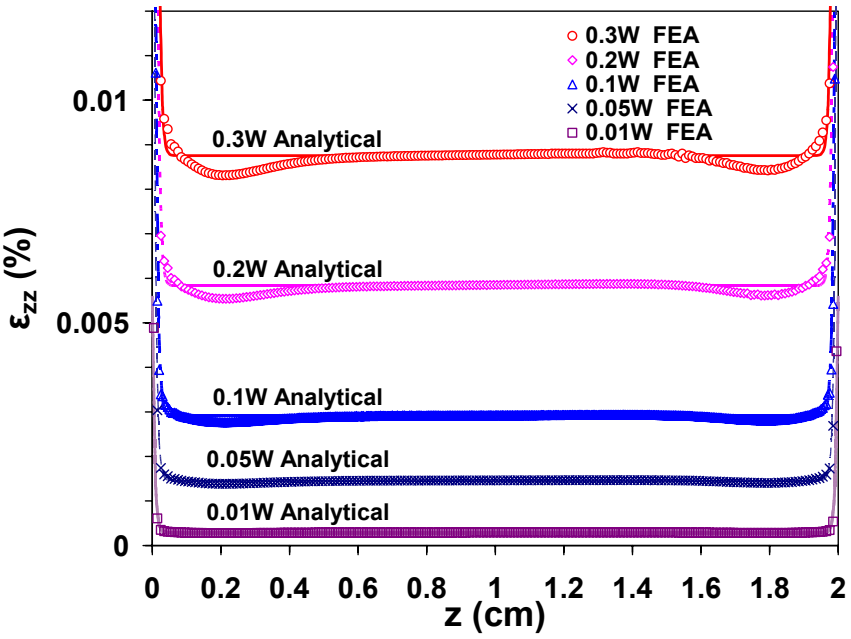

(a)

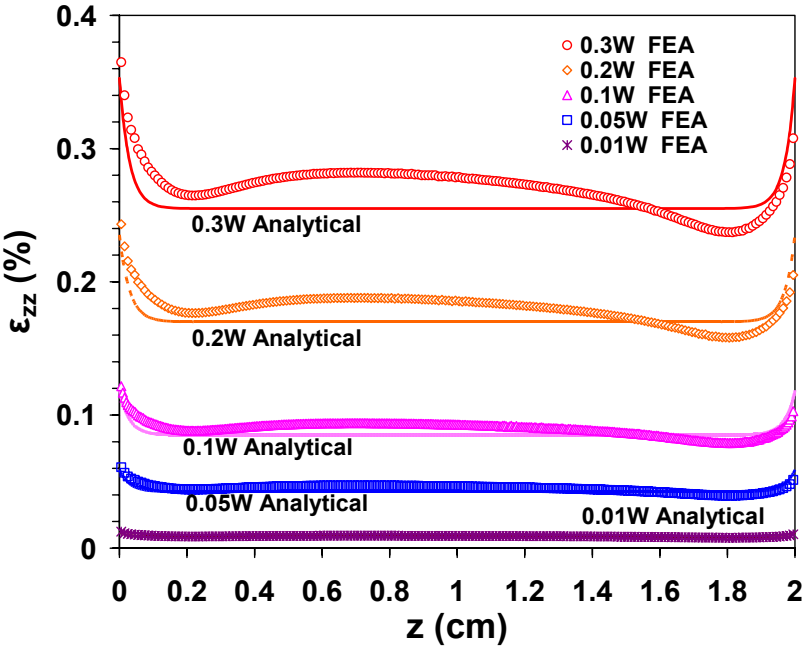

(b)

Figure 3.12: Axial strains in the core of the waveguide associated with (a) Si and (b) PMMA substrate. Bragg grating is inscribed from z= 0.5cm to z=1.5 cm along the waveguide core.

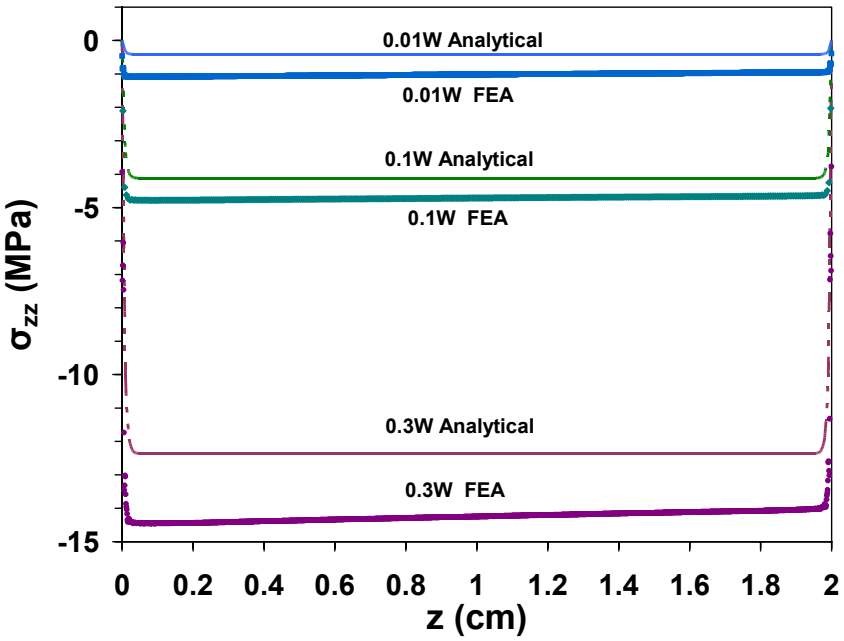

(a)

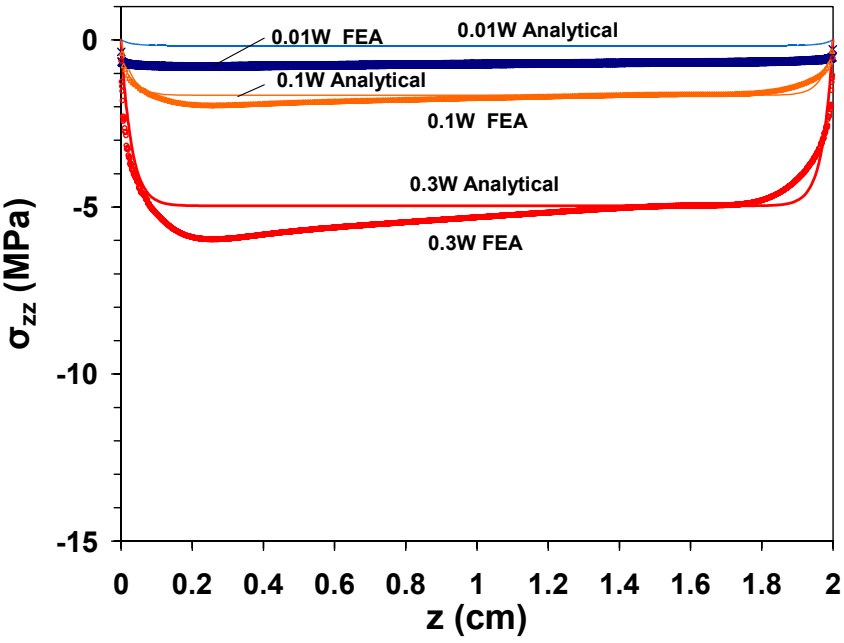

(b)

Figure 3.13: Axial stresses in the core of the waveguide associated with (a) Si and (b) PMMA substrate. Bragg grating is inscribed from z= 0.5cm to z=1.5 cm along the waveguide core.

Figure 3.13 shows the axial stresses in the core of the waveguide for the various incident optical powers of 0.01 to 0.3 W. The magnitude of the axial stress induced in the PMMA grating by the silicon substrate is about two and half times greater than that encountered when the grating is attached to a PMMA substrate; maximum stress in the core with a silicon substrate is nearly -14.5 MPa and that with PMMA substrate is approximately –6 MPa. The CTE mismatch between the waveguide layers and the Si substrate can explain about 2.5 times greater stresses in the PMMA grating on the Si substrate.

Figure 3.13 also shows that the stress profiles in the Bragg grating with the PMMA substrate are very complicated, while those in the Bragg gratings with the Si substrate are almost linear. It should be noted that maximum stress in the grating on the PMMA substrate occurs in the vicinity of the place in which the maximum temperature occurs, and the magnitudes of stresses along the grating on the PMMA substrate are seen to follow the temperature profile.

Eq. (3.39) was utilized to verify the FEA predicted axial stresses in the waveguide core. A relatively larger discrepancy (typically 13%) between the analytical and numerical predictions is observed for the Si substrate waveguide while the discrepancy for the PMMA substrate is typically less than 10 %.

This difference appears to show that the effect of the CTE mismatch of the silicon substrate on the axial stress is greater than the effect of the temperature gradient encountered in the use of the PMMA substrate. The non-uniform axial stress in Figure 3.13 confirms that the effect of temperature variations is not negligible even in the silicon substrate waveguide.

3.5.4 Thermo-Optical Analysis

As discussed in detail in section 3.1, the Bragg wavelength shift can be decomposed into the shifts associated with the individual effects (i.e., the thermally-driven index shift, the stress-induced index shift, and the grating pitch change), and the effects of the second-order terms involving the products of the thermally-driven index shift and the grating pitch change, and the stress-induced index shift and the grating pitch change, respectively. Equations (3.14) to (3.18) can be used to predict these individual components of the Bragg shifts for the PMMA grating attached alternately to a silicon or PMMA substrate.

Figure 3.14 show the three primary effects (the thermally-driven index shift, the grating pitch change, and the stress-induced index shift) and two secondary effects (the product of the thermally-driven index shift and the grating pitch change, the product of the grating pitch change and the stress-driven index shift) on the Bragg wavelength shift. It is to be noted that the Bragg wavelength shifts associated with the second-order terms are far smaller than the smallest one of the primary individual shifts. Moreover, the effect of the thermally-driven index shift on the Bragg wavelength change is greatest for both substrates. It was found that for the silicon substrate the effects of the grating pitch change and the stress-driven index shift on the wavelength change are very small compared to the effect of the temperature-induced index shift.

Interestingly, there is a little compensation for the temperature-driven negative Bragg wavelength shift in the PMMA grating by the positive shift of the wavelength induced by the grating pitch change and the stress-induced index shift. However, the negative shift is much larger than the positive shift, so that the compensation is not significant for the silicon substrate.

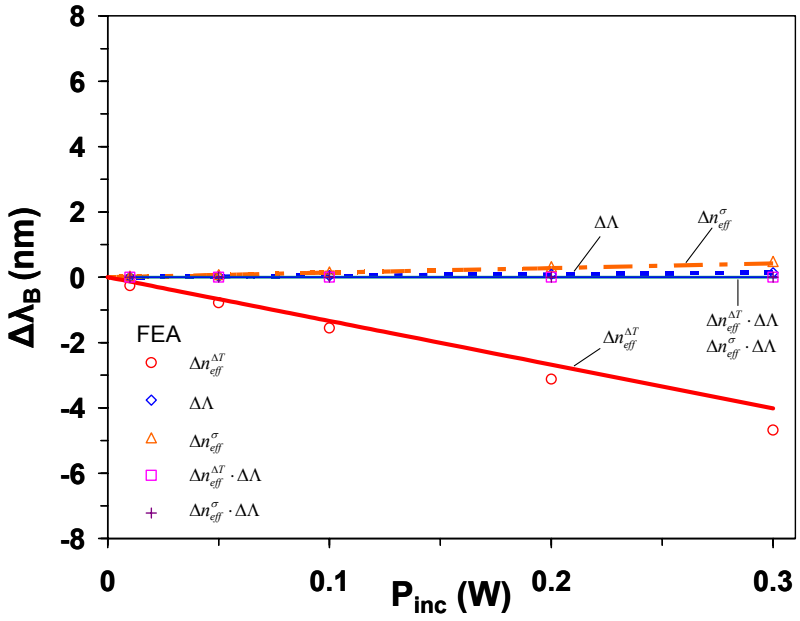

(a)

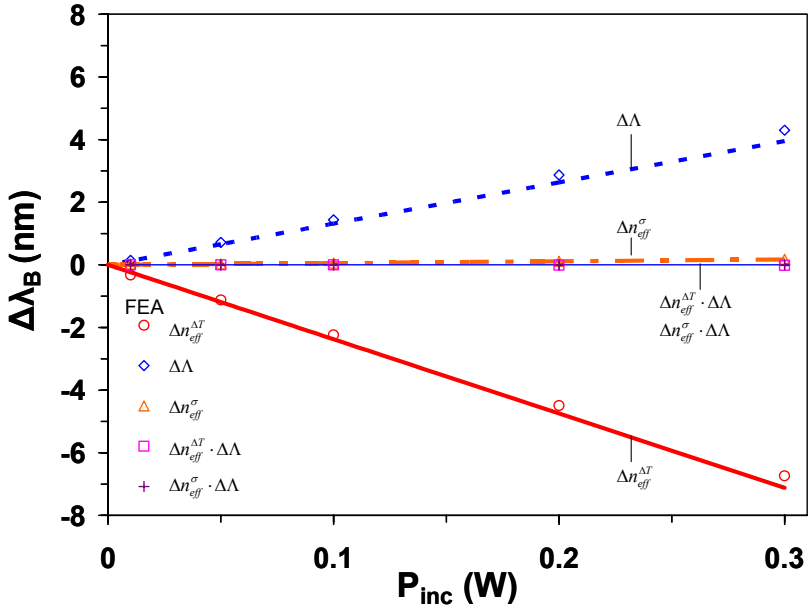

(b)

Figure 3.14: Individual Bragg wavelength shifts vs. incident optical powers in the (a) Si and (b) PMMA substrate

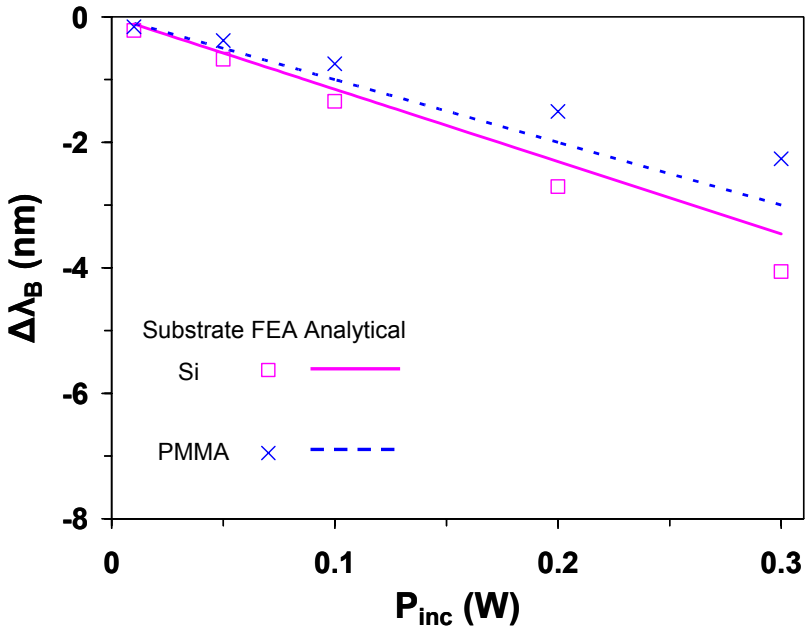

Figure 3.15: Bragg wavelength shifts vs. incident optical powers in the Si and PMMA substrates

Even for the PMMA substrate waveguide, the positive shift is about 40% less than the negative shift. Thus, while a considerable Bragg wavelength shift is expected even with the use of the PMMA substrate, it is to be seen that the shifts are approximately half those attained with a silicon substrate.

Figure 3.15 shows the total Bragg wavelength shifts for various incident optical powers. Interestingly, the Bragg wavelength shifts, predicted using analytically obtained thermo-structural results show general agreements with the predicted values using numerically obtained thermo-structural results.

The discrepancy between two predictions using the FEA and the analytical thermo-structural results may be caused by the assumptions inherent in the thermo-structural model. For the grating on the PMMA substrate, the spreading resistance in the thermal

model and the assumption of the uniform temperature in the thermo-structural model predict the higher average excess temperatures and lower total strain in the Bragg grating. This intrinsic limitation causes higher shifts in Bragg wavelengths. For the grating on the Si substrate, the spreading resistance in the PMMA cladding layers

are not included in the thermal model, and it result in the less prediction of the temperature in the grating. Consequently, it predicts a less shift in Bragg wavelength. However, it is also likely that the observed complicated behavior of temperature, strain, and stress could affect this discrepancy.

It is noteworthy that the use of the PMMA substrate has a beneficial effect, reducing the Bragg wavelength shift by 50 % relative to the use of the silicon substrate. This beneficial effect is mainly due to the net reduction in the Bragg shift caused by adding the negative Bragg wavelength shift, induced by the thermally-driven index shift, and the positive shift, caused by the grating pitch change and the stress-driven index shift. Figures 3.14(a) and (b) demonstrates the significant compensation which is mainly benefit of the large CTE, generating the large strain, of the PMMA substrate while the Si substrate produces much smaller strain due to the approximately two orders of magnitude smaller CTE.

Chapter 4

Detailed Thermo-Optical Modeling of Polymer Fiber Bragg Grating

In the proceeding chapter, it is shown that the polymer Bragg gratings may produce small Bragg wavelength shifts due to the compensation effect despite the relatively high absorption rate. It suggests that the polymer BGs could be successfully used to replace glass BGs for the short distance photonic data transmission. To concrete the possible usage of the polymer BGs, thermo-optical behaviors of the polymer BGs, including the effects of non-uniform temperature (thermal "chirp") along the BG, need to be studied more rigorously.

This chapter presents a methodology for thermo-optical modeling of a polymer fiber Bragg grating (PFBG) associated with the intrinsic absorption of light energy. An analytical formulation based on a modified coupled-mode theory is described, which determines the power variation induced by the coupling between counter-directional light waves within the PFBG. An analytical description for absorption-induced heat generation is provided and a semi-numerical thermo-optical model, using the modified Transfer Matrix Method (TMM), along with a simple analytical thermo-optical model, is also given. A methodology, models, results will serve to define the behavior of the PFBG, and it will then be a building block for a more complete analysis of an attached fiber or a planar BG.

4.1 Light Absorption in PFBG

4.1.1 Power spectrums of light sources

The radial variation of the power irradiance, $I(r)$, of a light source, can be assumed to follow a Gausssian profile, and to be given by [22]

$$I(r) = \frac{2P_{inc}}{\pi w^2} e^{-2r^2/w^2} \tag{4.1}$$

where P_{inc} is the incident optical power and w is the beam radius. The beam radius, w, can be defined as [42]

$$w = \sqrt{\frac{-2r_{co}^2}{ln(1-\Gamma)}} \tag{4.2}$$

where r_{co} is the radius of the core of the fiber and Γ is the power confinement factor; which determines the fraction of the incident optical power, which actually enters the core of the fiber. The power confinement factor, Γ, is defined as [42]

$$\Gamma = \frac{P_{co}}{P_{tot}} \tag{4.3}$$

where P_{co} is the power in the core , and P_{tot} is the total power illuminating the fiber. The confinement factor [42] is governed by various optical parameters. Using a Bessel function formulation, the confinement factor is found to be [42]

$$\Gamma = b\left(1 - \frac{J_0{}^2(V\sqrt{1-b})}{J_1(V\sqrt{1-b})J_{-1}(V\sqrt{1-b})}\right) \tag{4.4}$$

where V and b are the previously defined generalized frequency (see Eq. (2.4)) and generalized guide index (see Eq. (2.5)) of the fiber.

Engineering data [43, 44] for typical light sources of interest, suggests that the power spectrums of both Single Mode Laser Diodes (SMLD's) and Light Emitting Diodes (LED's) often follow a Gaussian distribution. The normalized spectral power density, $\overline{P(\lambda)}$, for these light sources can, thus, be expressed as

$$\overline{P(\lambda)} = Be^{4\ln 0.5((\lambda-\lambda_c)/FWHM)^2}$$
$$B = \frac{1}{2\int_0^{\delta\lambda} e^{4\ln 0.5((\lambda-\lambda_c)/FWHM)^2} d(\lambda)} \tag{4.5}$$

where $\delta\lambda$ is half of the total spectral bandwidth and FWHM is the "full width half maximum", which defines the spectral bandwidth at half of the maximum power. The central wavelength of the light source is given by λ_c. Figure 4.1 illustrates the power spectrums of a typical LED and a SMLD.

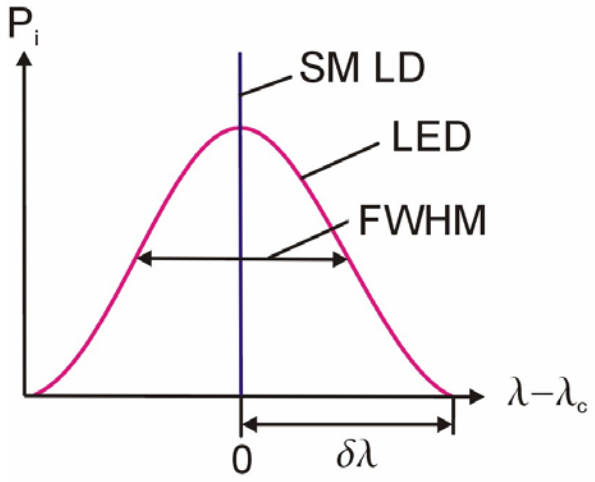

Figure 4.1: Power spectrums of a light emitting diode and a single mode laser diode

4.1.2 Optical coupling zones

The Bragg wavelength, λ_B, is the defining characteristic of a Bragg grating and serves as the reference value for three distinct zones of wavelength-related grating behavior. These three zones are shown in Figure 4.2 and seen to consist of: the "Bragg zone" (I) at and close to the Bragg wavelength – in which strong coupling occurs between the forward and backward moving waves leading to high grating reflectivity, the "weak interaction" zone (II) for modest values of λ - λ_B – for which diminishing coupling is observed at wavelengths that are progressively further away from λ_B , and a "waveguide" zone (III) in which no coupling occurs between the incident and reflected waves and the grating behaves simply as a waveguide. The defining wavelengths and the specific relations to be used in each zone are presented below.

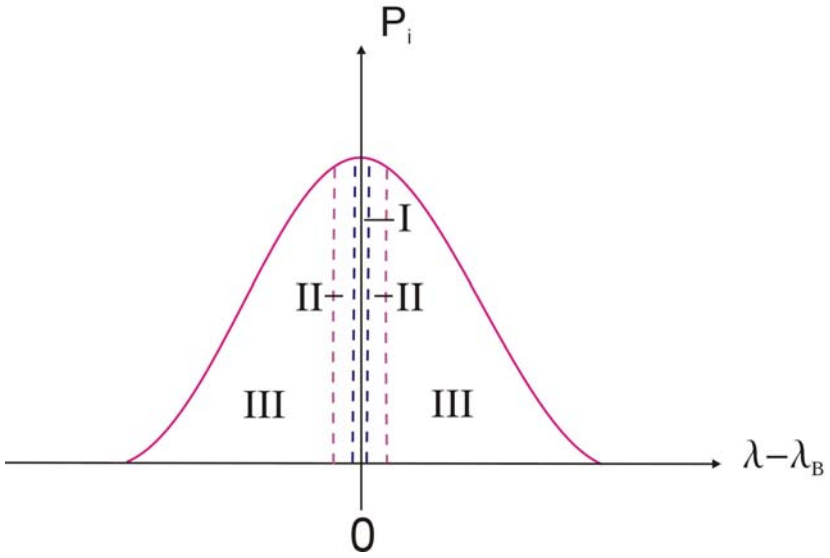

Figure 4.2: Zones of Bragg grating behavior: I – Bragg zone, II – weak interaction zone, III – waveguide zone

The optical characteristics of the Bragg Grating in the Bragg zone (I), including the reflection spectrum and the reflectivity, can be explained well by the coupled-mode

theory [45-47]. Wave propagation in the BG can be described by the scalar wave equation [45] as

$$\frac{\partial^2 E}{\partial z^2} + k_c{}^2 E = 0 \tag{4.6}$$

where E is the complex amplitude of the electrical field and k_c is the wave number in a lossy medium [45], as follows

$$k_c{}^2 = \beta^2 - i \cdot \hat{a}\beta + 4\kappa\beta \cos(2\beta_B z) \tag{4.7}$$

where the propagation constant β is defined as [45]

$$\beta = \frac{2\pi n_{eff}}{\lambda} \tag{4.8}$$

In Eq. (4.7), β_B is the propagation constant at the Bragg condition, $\hat{a}$ is the intrinsic absorption coefficient, and κ is the coupling coefficient. It is to be noted that the absorption coefficient, $\hat{a}$ (m^{-1}), used in the present analysis is related to the more common dB-based absorption coefficient, a (dB/cm) by

$$\hat{a} = 10 \cdot a \ln(10) \tag{4.9}$$

For example, an absorption coefficient of 11.513 m^{-1} is equal to 0.5dB/cm, and it represents about 10 % of optical power loss along 1 cm of propagation.

Following the approach proposed by Kogelnik [45], the electrical field in a FBG can be written as

$$E(z) = R(z)e^{-i\beta_B z} + S(z)e^{i\beta_B z} \tag{4.10}$$

where $R(z)$ and $S(z)$ are the amplitudes of the forward traveling and backward traveling waves, respectively. Substituting Eqs. (4.7), (4.8) and (4.10) into (4.6), we obtain

$$\frac{\partial^2 E}{\partial z^2} + k_c{}^2 E =$$
$$e^{-i\beta_B z} R'' - \left(2i\beta_B e^{-i\beta_B z}\right) R' - R\left[e^{-i\beta_B z}\left(-\beta^2 + i\cdot\hat{a}\beta + \beta_B^2\right) - 2\kappa\beta\left(e^{i\beta_B z} + e^{-i\cdot 3\beta_B z}\right)\right] \tag{4.11}$$
$$e^{i\beta_B z} S'' + \left(2i\beta_B e^{i\beta_B z}\right) S' + S\left[e^{i\beta_B z}\left(-\beta^2 - i\cdot\hat{a}\beta + \beta_B^2\right) + 2\kappa\beta\left(e^{-i\beta_B z} + e^{i\cdot 3\beta_B z}\right)\right] = 0$$

Assuming the amplitudes (*R* and *S*) vary slowly, R'' and S'' can be neglected in Eq. (4.11) [45]. Furthermore, as can be seen in Eq. (4.8), β is extremely large, and thus oscillating terms with much higher frequency than the Bragg frequency, i.e., $e^{i\cdot 3\beta_B z}$ and $e^{-i\cdot 3\beta_B z}$ can be also neglected [45]. Equation (4.11) can then be rewritten as

$$\begin{aligned} &-\left(2i\beta_B e^{-i\beta_B z}\right)R' - R\left[e^{-i\beta_B z}\left(-\beta^2 + i\cdot\hat{a}\beta + \beta_B^2\right) - 2\kappa\beta e^{i\beta_B z}\right] \\ &+\left(2i\beta_B e^{i\beta_B z}\right)S' + S\left[e^{i\beta_B z}\left(-\beta^2 - i\cdot\hat{a}\beta + \beta_B^2\right) + 2\kappa\beta e^{-i\beta_B z}\right] = 0 \end{aligned} \tag{4.12}$$

Comparing terms with equal exponentials in Eq. (4.12), the following coupled differential equations are obtained.

$$\begin{aligned} \frac{dR}{dz} &= -\left(\frac{\beta}{\beta_B}\frac{\hat{a}}{2} - \frac{\beta^2 - \beta_B{}^2}{i\cdot 2\beta_B}\right)R + \frac{\beta}{i\beta_B}\kappa S \\ \frac{dS}{dz} &= \left(\frac{\beta}{\beta_B}\frac{\hat{a}}{2} - \frac{\beta^2 - \beta_B{}^2}{i\cdot 2\beta_B}\right)S - \frac{\beta}{i\beta_B}\kappa R \end{aligned} \tag{4.13}$$

Assuming departures from Bragg wavelength are very small, i.e., $\left(\beta^2 - \beta_B{}^2\right)/(2\beta_B) \approx \beta - \beta_B$ and $\beta/\beta_B \approx 1$, Eq. (4.13) can be rewritten as the following coupled differential equations, which are frequently referred to as the **"***coupled-mode***"** equations, [21, 45]

$$\frac{dR}{dz} = -i\hat{\sigma}R(z) - i\kappa S(z)$$

$$\frac{dS}{dz} = i\hat{\sigma}S(z) + i\kappa R(z) \tag{4.14}$$

where $R(z)$ and $S(z)$ are the amplitudes of the forward traveling and backward traveling waves, respectively, the 'dc' self coupling coefficient, $\hat{\sigma}$, is related to the detuning, δ, and the intrinsic absorption coefficient $\hat{a}$ according to

$$\hat{\sigma} = \delta - \frac{\hat{a}}{2} i \tag{4.15}$$

and κ is the coupling coefficient [21].

The detuning value is a measure of the spectral proximity of the incident light to the Bragg wavelength, and is defined as [21]

$$\delta = \frac{2\pi n_{eff}}{\lambda} - \frac{\pi}{\Lambda} \tag{4.16}$$

For small values of δ much of the incident light will be reflected by the BG, creating a backward moving wave and transferring a significant amount of energy into the reflected wave, while for large detuning values nearly all the incident light will pass through the waveguide with little energy exchange between the counter directional waves.

The closed form solutions of the coupled-mode equations can be written as

$$\begin{aligned} R(z) &= r_1 e^{mz} + r_2 e^{-mz} \\ S(z) &= s_1 e^{mz} + s_2 e^{-mz} \end{aligned} \tag{4.17}$$

where the Eigen value, m, of the coupled-mode equations is given by

$$m = \sqrt{\kappa^2 - \hat{\sigma}^2} \tag{4.18}$$

and is, thus, dependent on the absorption coefficient, the detuning value, and the coupling coefficient. It should be notified that the absorption and the detuning enter this relation through the dc coupling equation presented in Eq. (4.15)

In solving these equations use is made of the boundary conditions, which set the amplitude of the forward wave at the inlet to unity and the amplitude of the backward

moving wave at the outlet to zero $\left(R(0)=1 \text{ and } S(L)=0\right)$. A detailed mathematical procedure to obtain the four coefficients in Eq. (4.17), using the above boundary conditions, is shown in Appendix A.

Using the DeMoivre's formula [48], the Eigen value can be expressed as a complex variable, i.e.,

$$m = m_1 + im_2 \tag{4.19}$$

where m_1 and m_2 are real numbers defined as

$$m_1 = \sqrt{\left[\sqrt{\xi^2 + (\hat{a}\delta)^2} + \xi\right]/2} \tag{4.20}$$

$$m_2 = \sqrt{\left[\sqrt{\xi^2 + (\hat{a}\delta)^2} - \xi\right]/2} \tag{4.21}$$

and where $\xi = (\hat{a}/2)^2 - \delta^2 + \kappa^2$.

Substituting Eq. (4.19) into Eq. (4.17), the amplitudes of the two waves (i.e., general solutions of the coupled-mode equations) can be rewritten as

$$R = 2r_1 e^{m_2 z}(\sinh(m_1 z)) + e^{-m_1 z}(r_1 e^{im_2 z} - r_1 e^{-im_2 z} + e^{-im_2 z}) \tag{4.22}$$

$$S = 2(e^{im_2 z} s_1 e^{m_1 L})\sinh(m_1(z-L)) + s_1 e^{-m_1 z}(e^{im_2 z} - e^{im_2(2L-z)})e^{2m_1 L} \tag{4.23}$$

By multiplying the conjugates of the complex amplitudes of two waves, the axial power of the forward and backward moving waves, respectively, can be expressed as

$$|R|^2 = \frac{c_1 e^{2m_1 z} + c_2 e^{2m_1(2L-z)} + c_3 \cos\left[2m_2(z-L)\right] + c_4 \sin\left[2m_2(z-L)\right]}{c_1 + c_5 + c_2 e^{4m_1 L}} \tag{4.24}$$

$$|S|^2 = \frac{c_6\left\{e^{2m_1 z} + e^{2m_1(2L-z)} - 2e^{2Lm_1}\cos\left[2m_2(z-L)\right]\right\}}{c_2\kappa^2 e^{4m_1 L} + c_1\kappa^2 + c_7} \tag{4.25}$$

The complete mathematical descriptions of the coefficients can be also found in Appendix A.

Graphs of the axial power variation for the forward and backward moving waves in the Bragg grating for several distinct values of $|\lambda - \lambda_B|$ generated via Eqs. (4.24) and (4.25) with 0.001nm steps for a PMMA FBG with the properties shown in Table 4.1, are displayed in Figure 4.3**.** The graphs reveal the expected "classic" behavior at the Bragg wavelength and show the effects of diminished coupling - on the slope and magnitude of the power graphs - for increasing values of $|\lambda - \lambda_B|$. However, at light wavelengths that are more than 0.058 nm from λ_B, the power of the forward moving and the backward moving waves are seen to increase in the axial direction. Given the restrictions imposed on the coupled-mode equations [45], this anomalous behavior may represent a departure from the coupled-mode theory. Since the optical coupling between the incident and reflected waves is expected to transfer light energy from the forward moving to the backward moving wave, it was anticipated that the power of both waves would decrease in the axial direction and that both $d\left(|S|^2\right)/dz$ and the axial derivative of $|R|^2$ would be uniformly negative, as seen at the Bragg wavelength and small detuning values. However, a rigorous re-derivation of the coupled-mode equations for large de-tuning values – which was beyond the scope of this work – may reveal that this behavior is consistent with the coupled-mode equations.

Nevertheless, to avoid the use of implausible power values and hence heating rates in the Bragg grating, the wavelength at which the axial slopes of the powers of the forward and backward moving waves become positive,

i.e. $d\left(|R|^2\right)/dz > 0$ and $d\left(|S|^2\right)/dz > 0$, are defined in this study as the boundary of the **"***Bragg zone***"** and the beginning of the **"***weak interaction***"** zone. For a PMMA grating with the properties shown in Table 4.1**,** this transition occurs at a λ - λ_B of ± 0.058 nm.

To extend the prediction of axial power variation in the grating into the "weak interaction" zone, and in the absence of a more rigorous approach in the literature, an approximate solution of the coupled mode equations is offered. As previously noted, due to the energy transfer between the two light waves, the power of both the incident and the reflected waves is anticipated to decrease along the axis of the BG. Considering this engineering assertion, the local axial gradients of the optical powers of the two waves can be assumed to be negative, i.e. $\frac{d\left(|R|^2\right)}{dz} < 0$ and $\frac{d\left(|S|^2\right)}{dz} < 0$. In addition, the fundamental assumption underpinning the coupled-mode equations, i.e. slowly varying amplitudes of the two waves, suggests that the local gradients of the optical power must vary smoothly along the grating. This implies the second derivatives of the forward and backward moving optical powers should be small, i.e. $\frac{d^2\left\{|R|^2\right\}}{dz^2} \approx 0 \quad and \quad \frac{d^2\left\{|S|^2\right\}}{dz^2} \approx 0$

Table 4.1: Properties and geometry of a PMMA Polymer Fiber Bragg Grating

(a) Basic parameters [49-51]

Parameter	Symbol	Value
Radius of core	r_{co}	3.5 *um*
Length	L	1 cm
Grating period	Λ	530.7 nm
Refractive index of core	n_{co}	1.49
Refractive index of cladding	n_{cl}	1.48

Bragg wavelength	λ_B	1576.5 nm
Maximum reflectivity without absorption	$\rho'_{\max}$	0.8

(b) Derived parameters

Parameter	Symbol	Value
Effective refractive index	n_{eff}	1.4853
Coupling coefficient at Bragg wavelength	κ_B	144.36 m^{-1}
Index modulation	δn_{eff}	7.244 x 10^{-5}
Maximum reflectivity with absorption	$\rho_{\max}$	0.745
Beam radius	w	3.7402 *um*

(c) Material properties of PMMA [26]

Parameter	Symbol	Value
Thermal conductivity	k	0.2 $Wm^{-1}K$
Coefficient of thermal expansion	α	73 x 10^{-6} K^{-1}
Absorption coefficient	$\hat{a}$	11.513 m^{-1}
Thermo-optical coefficient	dn/dT	-1.1 x 10^{-4} K^{-1}

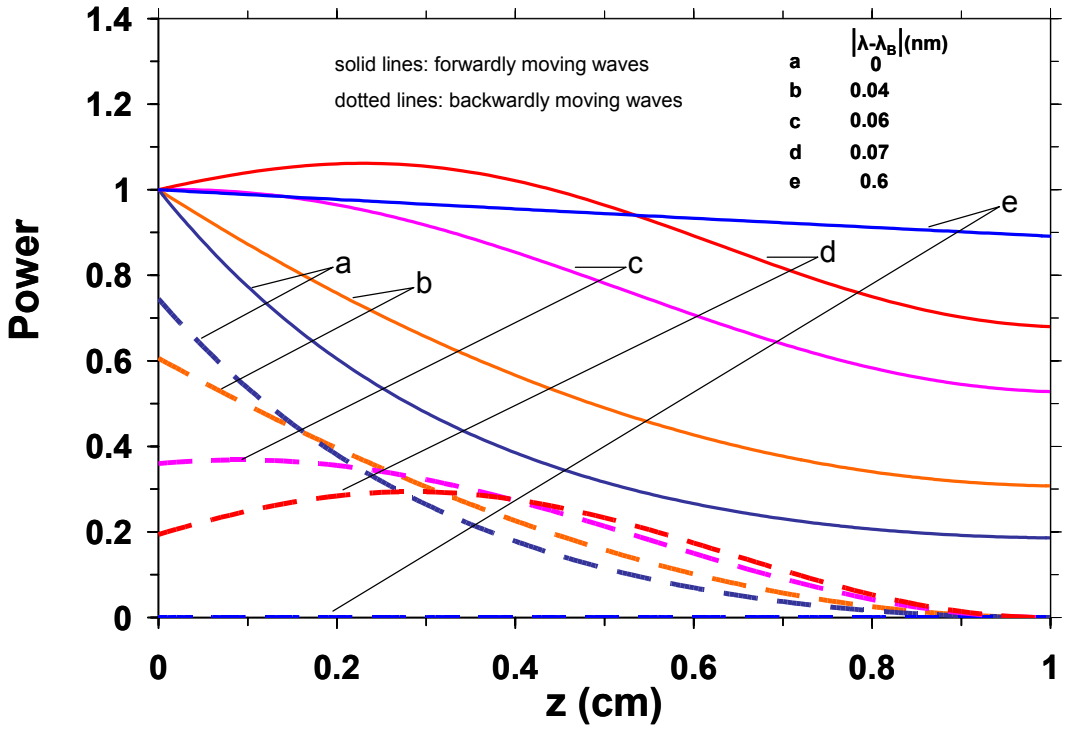

Figure 4.3: Coupled-Mode solutions for incident and reflected powers along a PMMA Fiber Bragg Grating

To satisfy these conditions, oscillating terms (cosine and sine terms) in Eqs. (4.24) and (4.25) were modified to the linear equations satisfying the values at the boundary, i.e. z = 0 and z = L. Consequently, the modified equations follow as

$$|R|^2 = \frac{c_1 e^{2m_1 z} + c_2 e^{2m_1(2L-z)} + c_3\left[\frac{(1-\cos 2m_2 L)}{L} z + \cos 2m_2 L\right] + c_4\left[\frac{(\sin 2m_2 L)}{L} z - \sin 2m_2 L\right]}{c_1 + c_5 + c_2 e^{4m_1 L}} \tag{4.26}$$

$$|S|^2 = \frac{c_6\left(e^{2m_1 z} + e^{2m_1(2L-z)} - 2e^{2Lm_1}\left[\frac{(1-\cos 2m_2 L)}{L} z + \cos 2m_2 L\right]\right)}{c_2\kappa^2 e^{4m_1 L} + c_1\kappa^2 + c_7} \tag{4.27}$$

Applying the power boundary conditions at the inlet ($\left|R\right|^2\Big|_{z=0}$=1) and the outlet of the grating ($\left|S\right|^2\Big|_{z=L}$ = 0) to the Eqs. (4.26) and (4.27), it is possible to approximate the axial power variation in the forward moving and the backward moving waves for the *weak interaction* zone. It should be noted again that these modified coupled-mode solutions (Eqs. 4.26 and 4.27) reflect the engineering assertion that due to the energy coupling between the forward and backward moving waves, the local axial gradients of both powers should be negative.

For light wavelengths sufficiently removed from the Bragg wavelength, i.e. large values of $\left|\lambda - \lambda_B\right|$, the BG reverts to a simple waveguide, producing no reflection. Under these circumstances, the axial power of the wave incident on the grating follows the exponential decay represented by Beer's law [22]. Consequently, the power of the forward moving wave at the end of the grating can be expressed as

$$\left|R\right|^2\Big|_{z=L} \approx e^{-\hat{a}L} \tag{4.28}$$

By setting the value of $\left|R\right|^2$ from Eq. (4.26) to that given by Eq. (4.28), a simple criterion for determining the effective bandwidth of the grating can be obtained. For wavelengths greater (and smaller) than the $\lambda - \lambda_B$ needed to match these two values, Beer's law can be employed to describe the optical power variations through the grating. In this region, the optical powers of the two waves becomes

$$\left|R\right|^2 = e^{-\hat{a}z} \tag{4.29}$$

$$\left|S\right|^2 = 0 \tag{4.30}$$

To determine the power propagating in a BG illuminated by a specified light source, it is, thus, necessary to integrate the optical power, $P(\lambda, r, z)$ across all three wavelength zones, i.e.

$$P(r,z) = \int P(\lambda,r,z)d\lambda = \int_{I} I(r)\overline{P(\lambda)}\left[|R(\lambda,z)|^2 + |S(\lambda,z)|^2\right]d\lambda$$

$$+ \int_{II} I(r)\overline{P(\lambda)}\left[|R(\lambda,z)|^2 + |S(\lambda,z)|^2\right]d\lambda + \left[I(r)e^{-\hat{a}z}\right]_{III} \tag{4.31}$$

It should be noted that the contribution of each zone to power propagation in the BG depends on the bandwidth of the light source used in the particular application. While a broad-band LED (with a FWHM of 50 nm) would distribute light across all three zones of the BG, a typical narrow-band SMLD, with a FWHM of 20 pm, may operate entirely in the Bragg zone (zone I). Moreover, for a broad-band LED light source, it is likely that the beam power contained in the Bragg and "weak interaction" zones would be negligible compared to the power transmitted in the "waveguide" zone. Determination of the boundaries of each BG zone, using the methodology described above, can serve to guide the selection of the most appropriate propagating power relation(s) from among those derived.

4.1.3 Heat generation in PFBG

Having established the power variation in the Bragg grating, it is now possible to determine the heating rate induced by the intrinsic absorption in the fiber, by an appropriate convolution of the power functions and absorption coefficients. Accordingly, heat generation at each wavelength and location in the PFBG can be expressed as

$$q_G(\lambda,r,z) = P(\lambda,r,z)\cdot\hat{a}(\lambda,r,z) \cong P(\lambda,r,z)\cdot\hat{a} \tag{4.32}$$

The latter equality applies if the absorption coefficient can be assumed to be constant along the length and radius of the grating, as well as to be invariant with wavelength.

In the range of interest, heat generation produced by the full spectrum of incident light can be obtained by integrating the spectral heat generation over the three zones of grating behavior, spanning the full spectral bandwidth, as

$$\begin{aligned} q_G(r,z) &= \left[\int_I q_G(\lambda,r,z)d\lambda + \int_{II} q_G(\lambda,r,z)d\lambda + \int_{III} q_G(\lambda,r,z)d\lambda \right] \\ &= \hat{a} \cdot \begin{Bmatrix} \int_I I(r)\overline{P(\lambda)}\left[|R(\lambda,z)|^2 + |S(\lambda,z)|^2 \right] d\lambda + \int_{II} I(r)\overline{P(\lambda)}\left[|R(\lambda,z)|^2 + |S(\lambda,z)|^2 \right] d\lambda \\ + \left[I(r)e^{-\hat{a}z} \right]_{III} \end{Bmatrix} \end{aligned} \quad (4.33)$$

where zone I is the central "Bragg zone" – given by the solutions of the coupled-mode equations, Eqs. (4.24) and (4.25), zone II is the "weak interaction zone" given approximately by Eqs. (4.26) and (4.27), and zone III is the "waveguide zone" for which Beer's law Eqs. (4.29) and (4.30) can be used.

A broadband light source, such as a LED with a central wavelength of 1550 nm, typically displays 50-100 nm of FWHM [44], some 50-100 times larger than the grating bandwidth of the specific case considered in the previous section; i.e., Zone III is much greater than Zones I and II. Consequently, the contribution of the reflected (or backward moving) wave to energy flow in the grating is very small and heat generation in a PFBG is primarily associated with simple absorption across the full bandwidth of the source, and can be expressed in a simple form as

$$q_G(r,z)\big|_{LED} = I(r)e^{-\hat{a}z} \cdot \hat{a} \quad (4.34)$$

A typical SMLD has a narrow spectral bandwidth, which is almost always less than 0.3 nm [43]. Thus, for the specific case cited above, the spectrum of such a SMLD

would be wholly or substantially contained within the grating bandwidth of the BG. Consequently, much of the light energy entering a PFBG in the forward moving wave will be transferred to the backward moving wave, leading to strong and spectrally complex axial variations in the propagating waves. Hence, the spatial variation of heat generation in a PFBG, under these circumstances, should be determined using Eq. (4.33).

4.2 Analytical Thermal Model of PFBG

Determination of the steady-state temperature field in the intrinsically-heated PFBG requires a solution of the heat conduction equation with non-uniform heat generation. In cylindrical coordinates, the governing equation for the temperature field can be expressed as [37].

$$\frac{\partial^2 \theta}{\partial r^2} + \frac{1}{r}\frac{\partial \theta}{\partial r} + \frac{\partial^2 \theta}{\partial z^2} + \frac{1}{k} q_G(r,z) = 0 \tag{4.35}$$

where θ is the excess temperature above ambient, and k is the thermal conductivity.

A schematic of the domain and symbols used for the analytical thermal model are shown in Figure 4.4, where r_{cl} is the radius of the entire fiber including its cladding, r_o was set to contain 99.9% of the incident optical power for the analytical thermal model, and consequently defines the boundary of the thermal model, Λ is the grating period, and L is the total length of the grating.

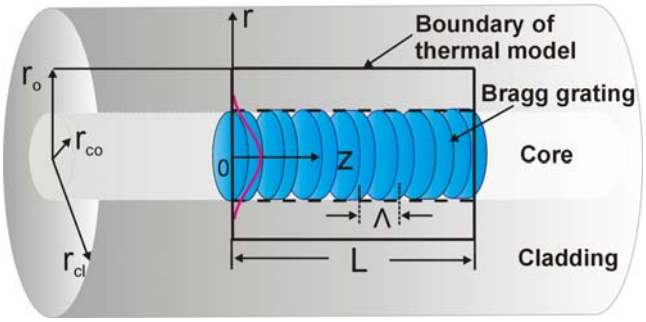

Figure 4.4: Geometry of a Polymer Fiber Bragg Grating thermal model

The fiber axial dimension is much larger than the core diameter of the BG, with a typical aspect ratio greater than 100:1. It is thus reasonable to assume uniform heat generation in the radial direction and reduce the above equation to a one-dimensional heat conduction equation. Inserting the relation for the internal heat generation (Eq. (4.34)) for the broad-band LED light source, the one-dimensional heat conduction equation takes the form of

$$\frac{d^2\theta}{dz^2} - p^2\theta = \frac{-P_{inc}}{k\pi r_o^{\,2}} \cdot e^{-\hat{a}z} \cdot \hat{a} \tag{4.36}$$

where $p = \sqrt{\frac{2h}{kr_o}}$.

In the above equation, h is the effective heat transfer coefficient on the outer surface of the modeled volume, reflecting the resistance to heat flow through the cladding and then into the ambient, which can be expressed as

$$h = \frac{1}{\frac{r_o}{k} ln\frac{r_{cl}}{r_o} + \frac{r_o}{h_{cl} r_{cl}}} \cong \frac{r_{cl}}{r_o} h_{cl} \tag{4.37}$$

where h_{cl} is the total combined (convection and radiation) heat transfer coefficient at the optical fiber surface. For the dimensions and conductivity of typical polymer optical

fibers, the conductive term ($r_o / k \cdot \ln(r_{cl} / r_o)$) can be neglected relative to the convective term ($r_o /(h_{cl} r_{cl})$) in the denominator of Eq. (4.37), yielding the approximation shown. For example, when r_o , r_{cl} , and k are 7 μm, 50 μm, and 0.2 W/m-K, respectively, $r_o /(h_{cl} r_{cl})$ (= 14 x 10^{-3}) is about two orders of magnitude greater than $r_o / k \cdot \ln(r_{cl} / r_o)$ (= 7 x 10^{-5}).

The general solution of Eq. (4.36) can be written as

$$\theta = g_1 e^{pz} + g_2 e^{-pz} + \theta_s \tag{4.38}$$

The particular solution can be expected to take the form of

$$\theta_s = De^{-\hat{a}z} \tag{4.39}$$

The procedure used to solve this equation and the derivation of the particular solution are presented in Appendix B.1. The solution is based on the assumptions that all heat loss occurs from the surface of the fiber, and that heat loss at the fiber BG ends can be neglected , i.e., assuming that both ends of the PFBG are adiabatic, i.e.,

$$\left.\frac{d\theta}{dz}\right|_{z=0} = 0 \quad \text{and} \quad \left.\frac{d\theta}{dz}\right|_{z=L} = 0 \tag{4.40}$$

The axial temperature variation in the PFBG is found as

$$\theta = \frac{P_{inc}\hat{a}^2}{\pi r_o{}^2 k \cdot (p^2 - \hat{a}^2)} \left\{ \frac{e^{-\hat{a}L}\cosh(pz) - \cosh[p(z-L)]}{p\sinh(pL)} + \frac{e^{-\hat{a}z}}{\hat{a}} \right\} \tag{4.41}$$

Examining Eq. (4.41), it may be seen that the temperature can be expected to decay exponentially in the axial direction, increase with incident power and the absorption coefficient, and decrease with thermal conductivity. It is to be noted that for polymer optical fibers, p (see Eq. 4.36) is typically two orders of magnitude greater than $\hat{a}$ due to the micron-size diameter of the fiber core.

The heat conduction model associated with a moderately narrow-band SMLD, for which light propagation is expected to occur primarily within zone I and II (ruled by the coupled mode equations) requires use of the more complex internal heat generation relation (Eq. (4.33)), i.e.,

$$\frac{d^2\theta}{dz^2} - p^2\theta + \frac{1}{k}\cdot\frac{P_{inc}}{\pi {r_o}^2}\cdot\int_{\lambda_1}^{\lambda_4}\overline{P(\lambda)}\left(\left|R(\lambda,z)\right|^2 + \left|S(\lambda,z)\right|^2\right)d\lambda\cdot\hat{a} = 0 \tag{4.42}$$

Applying the convective boundary condition on the surface of the fiber, the general solution of Eq. (4.42) can be expressed as

$$\theta = d_1 e^{pz} + d_2 e^{-pz} + \theta_p \tag{4.43}$$

where θ_p is a particular solution for the above conduction equation. The particular solution follows as

$$\begin{aligned}\theta_p = &\int_{\lambda_1}^{\lambda_4} F(\lambda)e^{2m_1(\lambda)z}d\lambda + \int_{\lambda_1}^{\lambda_4} G(\lambda)e^{-2m_1(\lambda)z}d\lambda + \int_{\lambda_2}^{\lambda_3} H(\lambda)\cos\left(M(\lambda)(z-L)\right)d\lambda \\ &+ \int_{\lambda_2}^{\lambda_3} N(\lambda)\sin\left(U(\lambda)(z-L)\right)d\lambda + \int_{\lambda_1}^{\lambda_2} V(\lambda)z + W(\lambda)d\lambda + \int_{\lambda_3}^{\lambda_4} V(\lambda)z + W(\lambda)d\lambda \\ &+ \int_{\lambda_1}^{\lambda_2} X(\lambda)z + Y(\lambda)d\lambda + \int_{\lambda_3}^{\lambda_4} X(\lambda)z + Y(\lambda)d\lambda\end{aligned} \tag{4.44}$$

It should be noted that the above particular solution is for a SMLD, whose spectral window ($\lambda_1 \le \lambda \le \lambda_4$) lies within zones I and II. More specifically, $\lambda_2 \le \lambda \le \lambda_3$ defines zone I, where the closed-form solution of the power variations (Eqs. (4.24) and (4.25)) should be used. However, in the spectral window, $\lambda_1 \le \lambda < \lambda_2$ or $\lambda_3 < \lambda \le \lambda_4$, which lies within zone II, the modified solutions of the power variations (Eqs. (4.26) and (4.27)) should be employed. Appendix B.2 shows a detailed procedure to obtain the two coefficients $\left(d_1 \text{ and } d_2\right)$ for the general solution, using the above boundary conditions (see Eq. (4.40)) as well as the particular solution.

4.3 FEA Thermal Model of PFBG

The foregoing analytical thermal model served to capture the salient features of the absorption-induced temperature profile in the polymer FBG, but neglected any radial temperature variations that might develop. A Finite Element thermal analysis was conducted to address this issue. Figure 4.5 shows a segment of the solution domain for the two-dimensional axi-symmetric finite-element model. The dimensions and the boundary conditions are the same as those used in the analytical model. The model had approximately 40,000 elements and the volumetric heat sources, $q_G(r,z)$, induced by light absorption in the grating, were applied to the model. In recognition of the high aspect ratio of the fiber and in order to simplify the model, the small heat losses from the ends of the PFBG were again ignored, and these surfaces were considered as adiabatic. The numerical simulation was conducted with the PCG solver of ANSYS 8.0 [35, 36].

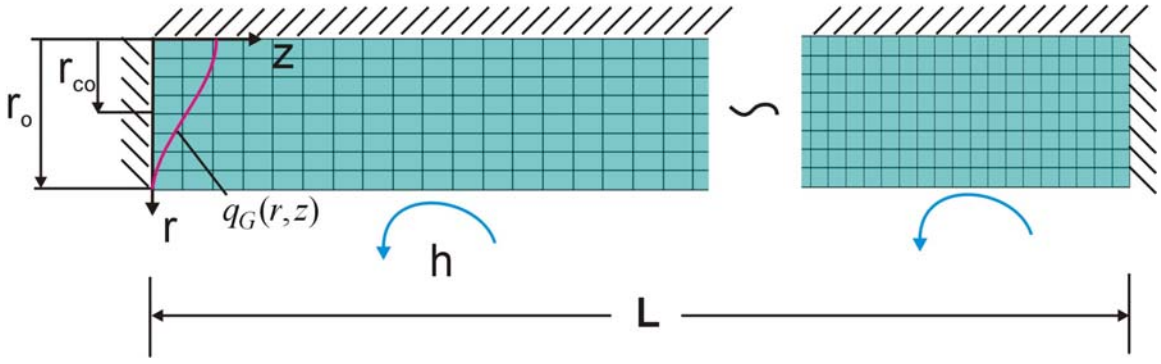

Figure 4.5: Geometry of the Finite Element model for a Polymer Fiber Bragg Grating

4.4 Thermo-Optical Model of PFBG

4.4.1. Isothermal grating

Thermally-induced changes of the refractive index and the grating period in the PFBG produce a shift in the Bragg wavelength of the grating. A thermo-optical equation, predicting the Bragg wavelength shift for the isothermal grating can be simply obtained from the general expression, Eq. (3.13), for the Bragg wavelength shift induced by the temperature change and stress by ignoring the stress effect on the index and the grating pitch. Consequently, the thermo-optical equation for the isothermal PFBG follows as

$$\frac{\Delta\lambda_B}{\lambda_{B1}} = \left(\frac{1}{n_{eff_1}} \frac{dn}{dT} + \alpha \right) \Delta T + \left(\frac{1}{n_{eff_1}} \frac{dn}{dT} \cdot \alpha \right) \Delta T^2 \tag{4.45}$$

where $\Delta\lambda_B = \lambda_{B2} - \lambda_{B1}$.

Equation (4.45) provides a two-term relation for the normalized Bragg wavelength shift; the first involving a linear dependence and the second a quadratic dependence on the temperature rise. For typical glassy polymers used for optical fibers operating at 1550 nm with an index of refraction of 1.5, the *dn*/*dT* is negative and falls in the range of 100 to 200 $\times 10^{-6}$/K, while the thermal expansion coefficient, α, is positive and can be expected to range from 60 to 80 $\times 10^{-6}$/K [26]. Due to the relatively large thermal expansion coefficient of the PFBG and the relatively small difference between the negative thermo-optic effect and positive grating period effect in the linear ΔT term, this quadratic term cannot generally be neglected in the analysis of PFBG.

4.4.2. Non-isothermal grating

As previously noted in Section 4.2, the inherently high absorption coefficients of optical polymers can be expected to produce an axially varying temperature profile in the

polymer Bragg grating, and necessitate some modification in the solution of the governing optical equations. Several methods for determining the optical field in a non-uniform BG can be found in the literatures [21, 51-53]. They include the Transfer Matrix Method (TMM) [21, 51-52], direct numerical method [21], and Rouard Method [53]. These methods were developed originally to analyze mechanically "chirped" gratings, in which the grating period varies along the optical path. The TMM was also used to analyze the thermally "chirped" gratings [54]. Under the influence of non-uniform light absorption and the consequent non-uniform heating, a uniform grating period may become "chirped," thus making these classical approaches suitable for the thermo-optic analysis of a PFBG. Of the choices available, the Transfer Matrix Method was chosen for implementation since it is relatively simple but appears to offer the desired accuracy.

The Transfer Matrix Method employs an analytical matrix solution to relate any two pairs of intensities (e.g., incident and reflected at the entrance) to any other two intensities (e.g., the transmitted and entering at the outlet), and is most often used to determine the reflectivity of a specified BG. As illustrated in Figure 4.6, the optical characteristics of each small segment, F_j, of a BG can be linearly-coupled to the next segment and can be represented in matrix form as

$$\begin{bmatrix} R_M(\lambda) \\ S_M(\lambda) \end{bmatrix} = F(\lambda) \begin{bmatrix} R(L) \\ S(L) \end{bmatrix}; \; F(\lambda) = F_M(\lambda) \cdot F_{M-1}(\lambda) \cdot \cdot F_j(\lambda) \cdot \cdot F_1(\lambda) \tag{4.46}$$

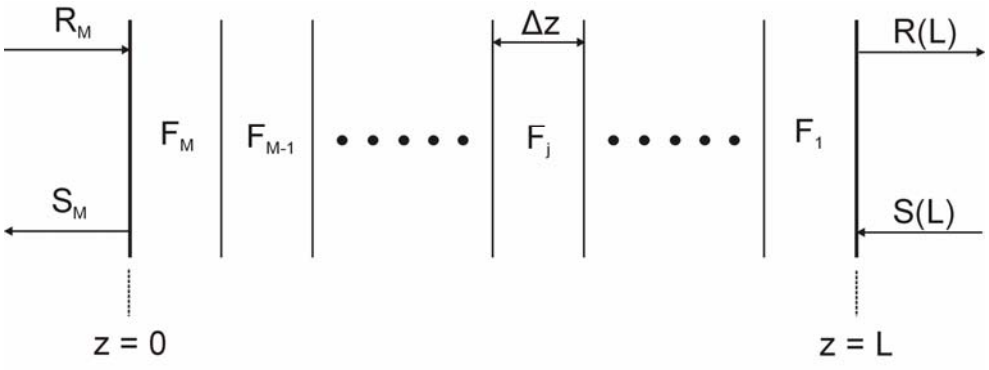

Figure 4.6: Illustration of Transfer Matrix Method (TMM)

In the TMM, at the end of the grating, unity and zero are assumed for the amplitude of the forward and the backward moving waves, respectively, i.e. $R(L) = 1$ and $S(L) = 0$, to obtain the amplitudes of both waves at the inlet of the grating. Each of the divided segments, $F_j(\lambda)$, with a grating length of Δz, must satisfy the coupled-mode theory, which results in the following mathematical description [21, 51].

$$F_j(\lambda) = \begin{bmatrix} -\cosh(m_j(\lambda)\Delta z) - i\dfrac{\hat{\sigma}_j(\lambda)}{m_j(\lambda)}\sinh(m_j(\lambda)\Delta z) & -i\dfrac{\kappa(\lambda)}{m_j(\lambda)}\sinh(m_j(\lambda)\Delta z) \\ i\dfrac{\kappa(\lambda)}{m_j(\lambda)}\sinh(m_j(\lambda)\Delta z) & -\cosh(m_j(\lambda)\Delta z) + i\dfrac{\hat{\sigma}_j(\lambda)}{m_j(\lambda)}\sinh(m_j(\lambda)\Delta z) \end{bmatrix} \tag{4.47}$$

where the coupling coefficient, $\kappa(\lambda)$, is again equal to $\pi \cdot \Delta n_{eff} / \lambda$, and Δn_{eff} to the index modulation of the grating. Applying TMM to an uniformly-pitched or isothermal BG, with the assumption of $R(L) = 1$ and $S(L) = 0$, the reflectivity spectrum, $\dfrac{|S|^2}{|R|^2}$, can be shown to be identical to that determined by the coupled-mode solutions. While $F_j(\lambda)$ is fundamentally identical to the transfer matrix presented in [21], it should be noted that

components of $F_j(\lambda)$ were formulated to satisfy the present nomenclature and coordinate system.

The absorption-induced self-heating of the PFBG generates an axially exponential temperature profile, and results in non-uniform index and grating period along the PFBG. Consequently, the F-matrix, F_j, in the transfer matrix must be modified to include the effect of these thermally-induced non-uniformities on the optical behavior of the PFBG.

A typical index modulation for a BG, δn_{eff}, is approximately 0.01 % of the refractive index of the fiber core [6]. In addition, in a bulk index grating, the materials of the alternating layers differ by little else than the small difference in index, and the thermo-optic coefficients, *dn/dT*, of the two layers can be expected to be nearly identical. Hence, it is reasonable to assume that the index modulation is invariant with temperature and that any possible change in the modulation is negligible compared to the thermally-driven change of the fiber core index material.

Considering the thermally-driven index shift, the "new" index of refraction for each segment of the grating, $n_{eff\,2,j}$ can be expressed as

$$n_{eff\,2,j} = n_{eff\,1} + \frac{dn}{dT}\Delta T_j \tag{4.48}$$

Similarly, the "new" period of the grating element caused by thermal expansion is

$$\Lambda_{2,j} = \Lambda_1\left(1 + \alpha\Delta T_j\right) \tag{4.49}$$

Using Eqs. (4.48) and (4.49), the 'dc' coupling coefficient for a specified element, $\hat{\sigma}_j$, can be written as

$$\hat{\sigma}_j(\lambda) = \frac{2\pi n_{eff_j}}{\lambda} - \frac{\pi}{\Lambda_j} - i\frac{\hat{a}}{2} = \frac{2\pi}{\lambda}\left(n_{eff\,1} + \frac{dn}{dT}\Delta T_j\right) - \frac{\pi}{\Lambda_1\left(1+\alpha\Delta T_j\right)} - i\frac{\hat{a}}{2} \tag{4.50}$$

and the Eigen value of coupled-mode equations , m_j , can be expressed as

$$m_j(\lambda) = \sqrt{\kappa^2(\lambda) - \hat{\sigma}_j{}^2(\lambda)} = \sqrt{\left(\frac{\pi}{\lambda}\Delta n_{eff}\right)^2 - \left(\frac{2\pi}{\lambda}\left(n_{eff\,1} + \frac{dn}{dT}\Delta T_j\right) - \frac{\pi}{\Lambda_1\left(1+\alpha\Delta T_j\right)} - i\frac{\hat{a}}{2}\right)^2} \tag{4.51}$$

Substituting $\hat{\sigma}_j$ and m_j into Eq. (4.47), defines all the terms of the matrix, F_j .

Using the boundary condition ($R(L) = 1$ and $S(L) = 0$) [21, 51], the amplitude of the forward moving wave, $R_M(\lambda)$, and backward moving wave, $S_M(\lambda)$, at the inlet of the PFBG can now be obtained. The reflectivity spectrum can then be found as

$$\rho(\lambda) = \frac{|S_M(\lambda)|^2}{|R_M(\lambda)|^2} \tag{4.52}$$

With the reflectivity determined, it is possible to obtain the reflected power spectrum, $P_{ref}(\lambda)$, as the product of the incident optical power and the reflectivity. Mathematically, it can be expressed in a simple form as

$$P_{ref}(\lambda) = P_{inc}\overline{P(\lambda)}\rho(\lambda) \tag{4.53}$$

Chapter 5

Experimental Verification of Thermo-Optical Model

An experiment is conducted to verify validity of the thermo-optic modeling proposed in the previous chapter. A commercial PMMA FBG was not available at the time of this study, and a commercial glass FBG was used for verification instead. After calibrating the experimental setup using an isothermal loading, an axially decaying temperature field is produced artificially in the glass FBG using natural convection. The temperature field simulates the expected large temperature gradient in a PMMA FBG, caused by the intrinsic absorption of light energy.

Although producing an extreme temperature gradient within a glass FBG is not a trivial task, use of the glass FBG offers an important advantage for verification since the experiment measures only the Bragg wavelength shift. A preliminary analysis revealed that, in a PMMA FBG, spectral compensation, which results from the opposite contributions of thermo-optic and thermal expansion, dominates and thus produces only a tiny shift in the Bragg wavelength shift. The analysis also revealed that a temperature gradient has virtually no effect on the Bragg wavelength shift. With a glass FBG, the compensation does not exist and the effect of the temperature gradient is clearly evident, which is more suitable for verification of the model that was developed for temperature fields with strong gradients.

5.1 Experimental Setup

Bragg grating was inscribed on an optical fiber (corning SMF-28e) by Avensys Inc. The diameter of core (SiO_2) is 8.2 μm, and the total diameter of the fiber, including a

cladding (SiO_2) and a coating (polyimide), is 155 μm. The total grating length is 1 cm, and the reflectivity of the FBG is 80 %.

The optical parameters and material properties of the FBG are presented in Table 5.1. The Bragg wavelength (λ_B), the grating period (Λ), the effective index (n_{eff}), and the maximum reflectivity ($\rho_{\max}$) are 1550 nm, 532 nm, 1.4567, and 0.8, respectively.

Table 5.1: Properties and geometry of a Fiber Bragg Grating

(a) Optical parameters [55, 56]

Parameter	Symbol	Value
Radius of core	r_{co}	4.1 μm
Length	L	1 cm
Mask grating pitch	Λ_g	1064 nm
Refractive index of core	n_{co}	1.46
Numerical Aperture	NA	0.14
Bragg wavelength	λ_B	1550 nm
Maximum reflectivity	$\rho_{\max}$	0.8
Effective refractive index	n_{eff}	1.4567
Coupling coefficient at Bragg wavelength	κ_B	144.36 m^{-1}
Index modulation	δn_{eff}	7.123 x 10^{-5}
Grating period	Λ	532 nm

(b) Material properties [26]

Parameter	Symbol	Value
Thermal conductivity	k	1.4 $Wm^{-1}K$
Coefficient of thermal expansion	α	0.55 x 10^{-6} K^{-1}
Thermo-optical coefficient	dn/dT	8.6 x 10^{-6} K^{-1}

A heating system to produce the temperature profile within a Bragg grating is shown in Figures 5.1(a) and (b). The heating system consists of an aluminum stage (40 × 10 × 6.4 mm), a copper heat sink (40 × 40 × 13 mm), a thermo-electric (TE) heater

(Melcor CP1.4-127-10L-1-W6), and an aluminum plate. The temperature of the copper heat sink was controlled by the TE heater, and the heat sink acted as an isothermal block. A 25 μm-deep groove was made on the Al stage to support the fiber mechanically. A temperature control with 0.1K accuracy was archived routinely.

For an isothermal loading, the BG portion of the fiber was placed on the groove of the Al stage (Figure 5.1a). In order to produce a temperature profile simulating a self-heated PFBG, the BG portion of the fiber was repositioned so that its edge was in contact with the Al stage (Figure 5.1b). The temperature of the end of the FBG was maintained isothermally by the Al stage, and the temperatures along the FBG decayed exponentially due to natural convection; it acted as a passively-cooled thermal fin. Precise positioning of the FBG with respect to the Al stage was achieved by a high precision micrometer stage (J.A. Noll Co.).

The apparatus for the spectral analysis is shown schematically in Figure 5.1(c). A superluminescent light emitting diode (SLED: Exalos ESL1510-2111) was used as a broadband light source. The SLED was controlled by a laser diode controller (ILX Lightwave LDC-3724) through a laser diode mount (ILX Lightwave LDM-4980). A 3-dB coupler (Gould fiber optics) was used as an interconnect to transmit the light from the SLED to the FBG and to transfer the reflected light from the FBG to the optical spectrum analyzer (OSA) that collects the reflected optical signals from the FBG. Other components include a DC power supply for the TE heater (Agilent 6038A) and a 5 channel data logger unit (Agilent 34970A) to document temperatures of the Al stage and the ambient air. The actual test setup is shown in Figures 5.2 (a) and (b).

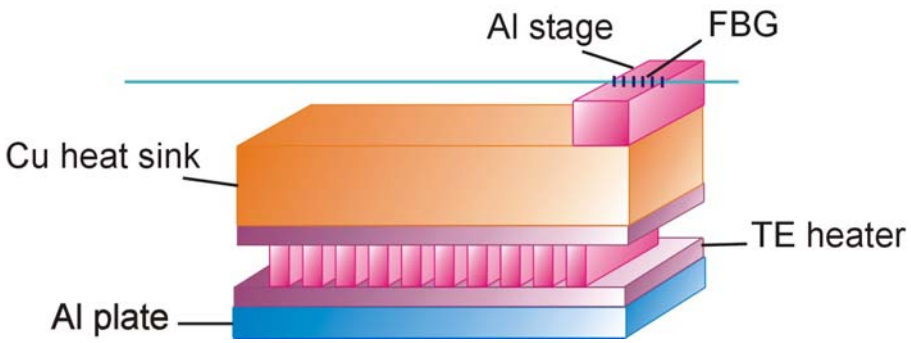

(a)

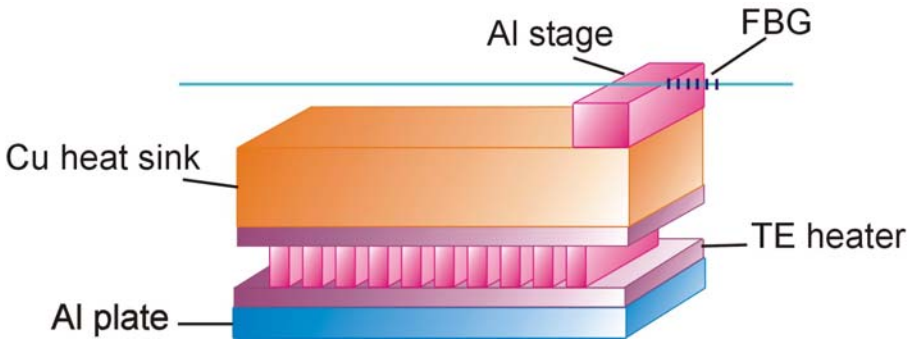

(b)

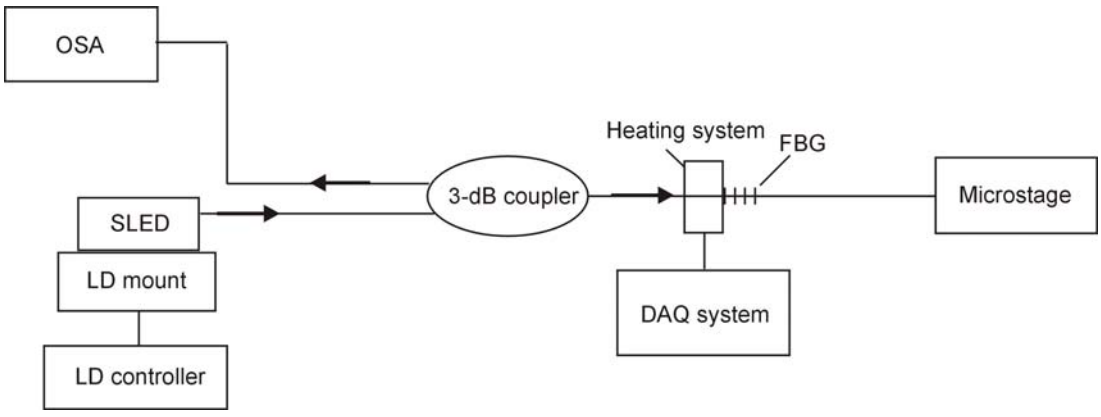

(c)

Figure 5.1: Heating system for (a) uniform temperature distribution and (b) exponentially decaying temperature distribution. (c) Schematic diagram of the measurement system for the spectral analysis.

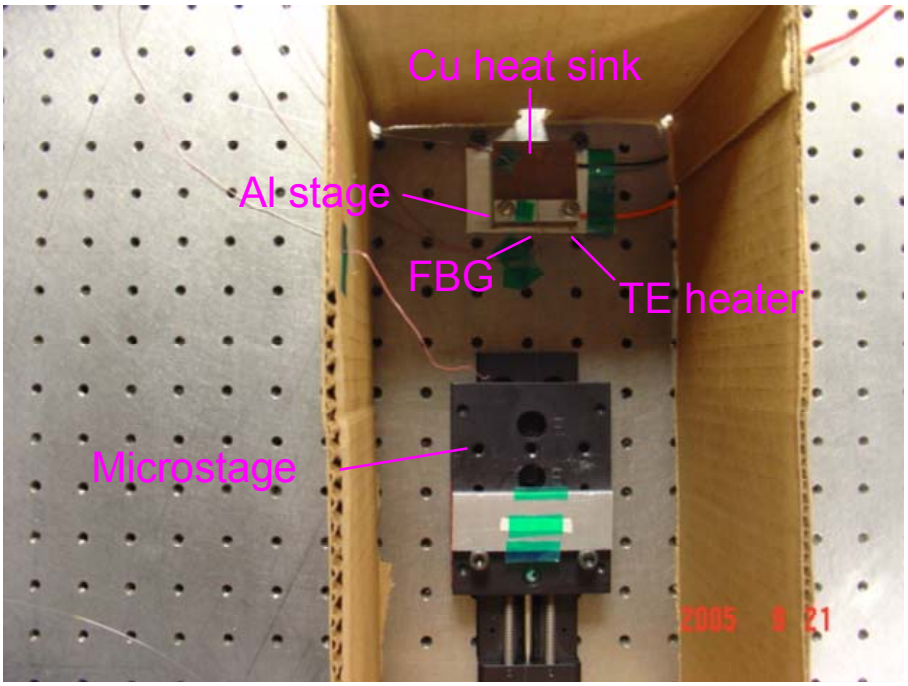

(a)

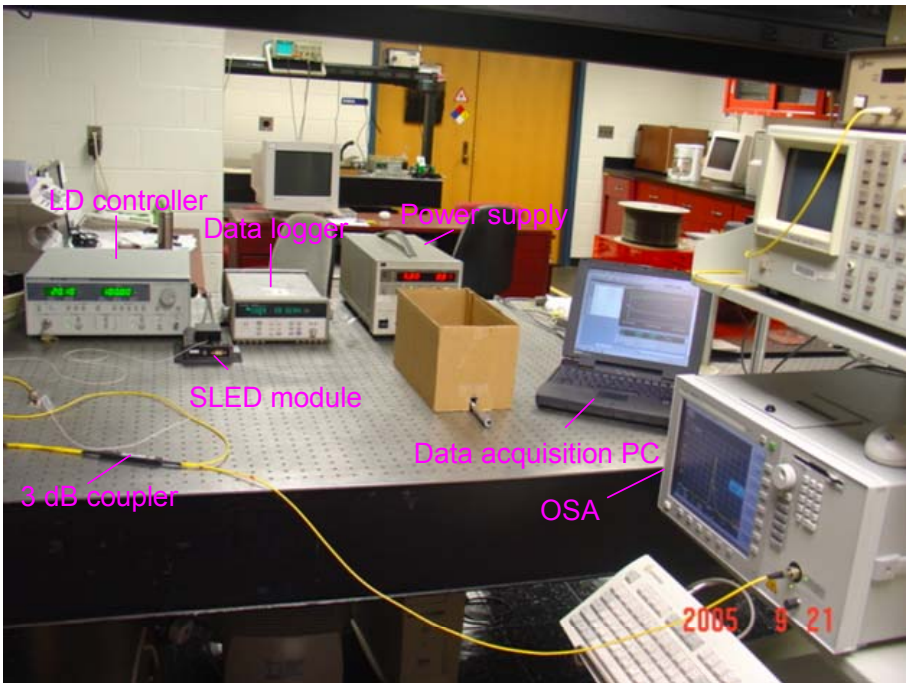

(b)

Figure 5.2: Pictures of (a) the test section for the spectral analysis of a FBG (b) the measurement system for the spectral analysis of a FBG

5.2 Isothermal Distribution

An isothermal loading was used first to check the integrity of the measurement system. The Bragg wavelength shifts were measured at excess temperatures, to the reference of 25°C, of 25 K, 35 K, and 45 K. The measured values are plotted in Figure 5.3 with those predicted by the analytical solution (Eq. 3.1). The experimental data are in good agreements with the predicted values, which confirms the integrity of the measurement system. It is to be noted that the measured Bragg wavelength shift is approximately 0.01 nm/K, which is very close to the reported value in the literature [25].

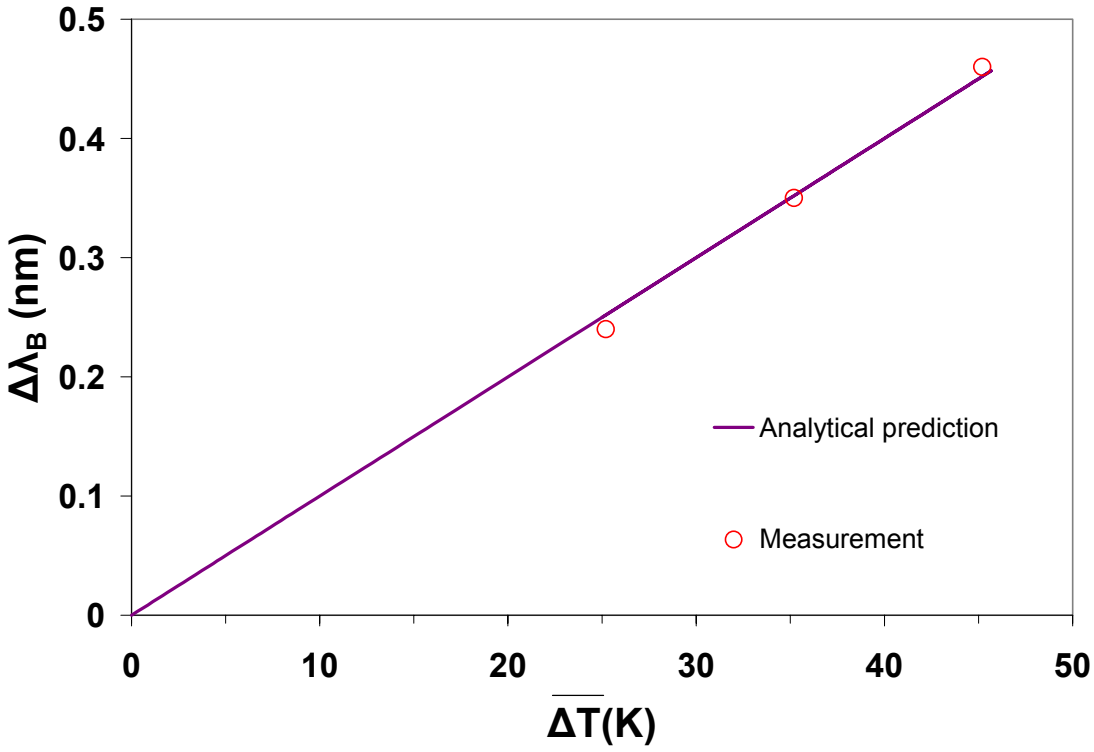

Figure 5.3: Bragg wavelength shifts of an isothermal FBG

The spectra of reflected powers were also documented at the excess temperatures. They were normalized by the maximum reference power and are compared with the

spectra predicted numerically by the TMM (Eqs. 4.46 and 4.47) in Figure 5.4. The predicted normalized reflected powers show excellent agreements with the measured values except minor discrepancies in the side lobes. More specifically, the predicted spectra display a perfect symmetry while the measured ones show an asymmetry; side lobes at the right hand side are greater than those at the left hand side. It is speculated that these asymmetric side lobes might be attributed to imperfect index modulation along the FBG.

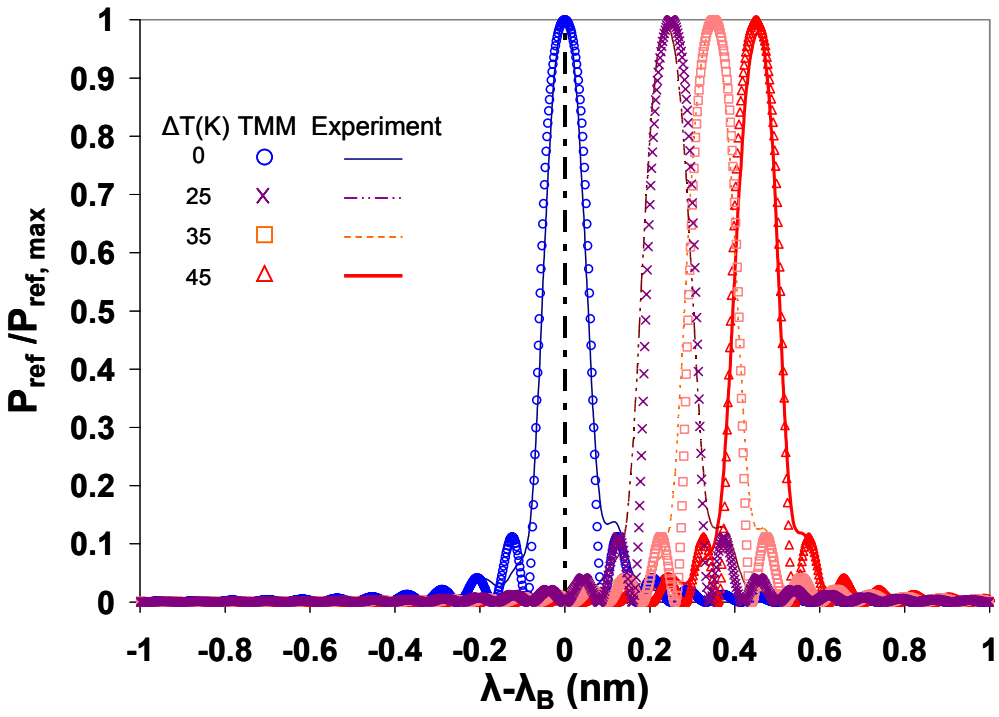

Figure 5.4: Normalized reflected power spectra of an isothermal FBG

5.3 Non-uniform Temperature Distribution

5.3.1 Determination of temperature distribution

The non-uniform temperature profile simulating a self-heated PFBG was produced by edge heating and natural convection, but it was difficult to measure the actual temperature distribution along the FBG due to the small dimension of the FBG. The following analytical approach based on the steady state 1-D thermal fin-analysis was adopted to predict the temperature distribution.

Using a 1-D thermal fin equation [33], excess temperatures along the FBG can be expressed as

$$\theta(z) = \theta_b \cdot e^{-\psi z} \tag{5.1}$$

where $\Psi = \sqrt{2\bar{h}/kr_o}$; θ_b is the excess temperature of the FBG base; $\bar{h}$, k, and r_o are the average heat transfer coefficient, the thermal conductivity, and the radius of the fiber, respectively.

Numerous correlations to estimate the average heat transfer coefficient for the horizontal cylinder under the natural convection can be found in the literature [57]. The correlations have the form of

$$\overline{Nu}_D = A + B \cdot \left(\overline{Ra}_D\right)^C \tag{5.2}$$

where $\overline{Nu}_D$ and $\overline{Ra}_D$ are an average Nusselt number and a Raleigh number, and A, B, and C are empirically determined constants. The empirical correlation constants available in the literature are shown in Table 6.2 [57]. In Eq. (5.2), the average Raleigh number is defined as [58]

$$\overline{Ra}_D = \frac{g\beta'\bar{\theta}D_o^{\,3}}{\nu'\alpha'} \tag{5.3}$$

where $g, \beta', \nu', \alpha', \bar{\theta}$, and D_o are the gravitational acceleration, the volumetric thermal expansion coefficient, the kinematic viscosity, the thermal diffusivity, the average excess temperature, and the cylinder diameter, respectively.

The correlations defined by Eq. (5.2) were developed originally for long and thin hot wires. If the aspect ratio of the wire (length/width = l/D_o) is not sufficiently large (< 10^5), the effect of the axial conduction losses becomes significant and Nusselt numbers can be overestimated substantially. The length of the heated FBG and the fiber diameter are 1 cm and 155 μm, respectively, which yields l/D_o of only 64.5. A correction factor was proposed to compensate the effect of the aspect ratio [57]. The corrected Nusselt numbers can be expressed as

$$\overline{Nu}_{D,C} = \frac{\overline{Nu}_D}{1+f} \tag{5.4}$$

where f is a correction factor defined as $\frac{7.5}{(l/D_o)^{1/2}} + \frac{3.5\times10^4}{(l/D_o)^2}$. Using Eq. (5.4), the average heat transfer coefficient can be determined as

$$\bar{h} = \frac{k_f}{D_o}\overline{Nu}_{D,C} \tag{5.5}$$

where k_f is the thermal conductivity of the ambient air at the film temperature.

It is to be noted that the average excess temperature should be known to determine an average Nusselt number using the correlation function (Eq. 5.2). The average heat transfer coefficient, $\bar{h}$, for the initial condition, θ_b of 25K was determined by the following iteration process; (1) the average heat transfer coefficient, $\bar{h}$, is assumed

first for the initial condition, θ_b of 25K (e.g. 10W/m^2-K), (2) the temperature distribution, θ, and subsequently the average temperature, $\bar{\theta}$, are determined with the assumed $\bar{h}$ using Eq. (5.1), (3) using the average temperature, $\bar{\theta}$, an average Raleigh number was evaluated using Eq. (5.3), (4) an average Nusselt numbers is evaluated using Eqs. (5.2) and (5.4), (5) the average heat transfer coefficient $\bar{h}$ is determined using Eq. (5.5), and (6) repeat steps (2)-(5) using the average heat transfer coefficient $\bar{h}$ determined in step (5). The process continues until the value of $\bar{h}$ converges. The values of $\bar{h}$ and $\bar{\theta}$ obtained for the initial condition, θ_b of 25K were 9.5 W/m^2-K and 8 K.

The average heat transfer coefficient, $\bar{h}$, can be estimated using the following relationship

$$\bar{h} \propto \left(\bar{\theta}\right)^{1/4} \tag{5.6}$$

The values of $\bar{h}$ for other excess base temperatures of interest were also calculated by the following iteration process; (1) the average heat transfer coefficient, $\bar{h}$ (e.g. 10.5W/m^2-K), is assumed first for a condition, e.g., θ_b of 40 K, (2) the temperature distribution, θ, and subsequently the average temperature, $\bar{\theta}$, are determined with the assumed $\bar{h}$ using Eq. (5.1), (3) the average heat transfer coefficient, $\bar{h}$ for θ_b of 40 K is determined with the determined average temperatures, $\bar{\theta}$ for θ_b of 40 K and $\bar{\theta}$ for θ_b of 25K using Eq. (5.6), and (4) repeat steps (2)-(3) using the average heat transfer coefficient $\bar{h}$ determined in step (3). The process continues until the value of $\bar{h}$ converges. The value of $\bar{h}$ for θ_b of 40 K was 12.3 W/m^2-K.

Table 5.2: Constants for Eq. (5.2) [57]

Author	A	B	C
Langmuir	0	0.81	0.065
Mikheyev	0	1.18	0.125
Beckers et al.	0	0.95	0.08
Mabuchi and Tanaka	0	1.02	0.1
Hatton et al.	0.525	0.422	0.315

Representative temperature profiles along the FBG are shown in Figure 5.5, where the FBG base temperatures are 85, 65, 45, and 25K. Exponential decay is evident.

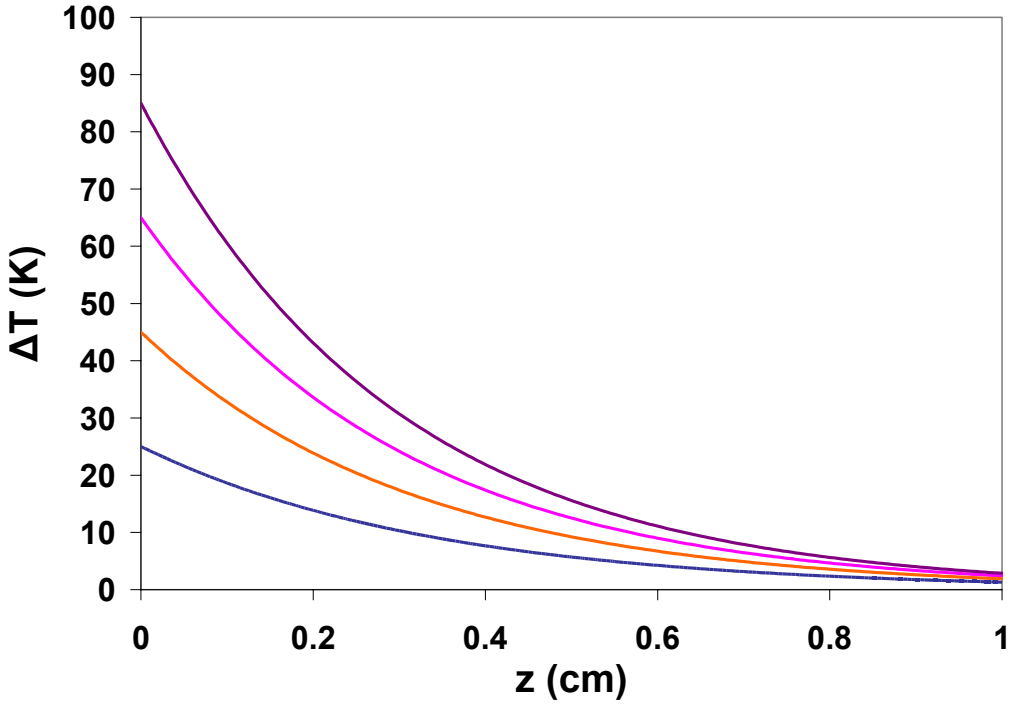

Figure 5.5: Representative excess temperature profiles along the FBG for the excess base temperatures of 85, 65, 45, and 25K

5.3.2 Results and discussion

Bragg wavelength shifts were calculated by the TMM (Eqs. 4.46 and 4.47) using the temperature distributions obtained in the previous section. The results are compared

with the experimental data, obtained at 5K interval, in Figure 5.6. The proposed thermo-optical model predicts Bragg wavelength shifts reasonably well. The discrepancy is less than 10%, which falls within experimental uncertainties considering the typical measurement error associated with the OSA of ± 5pm.

The analytical prediction of Bragg wavelength shifts using the average temperature (Eq. 3.1) is also plotted in Figure 5.6. The results deviate significantly from the experimental data, which clearly demonstrates the need for the complex numerical model for the temperature distribution with a large temperature gradient.

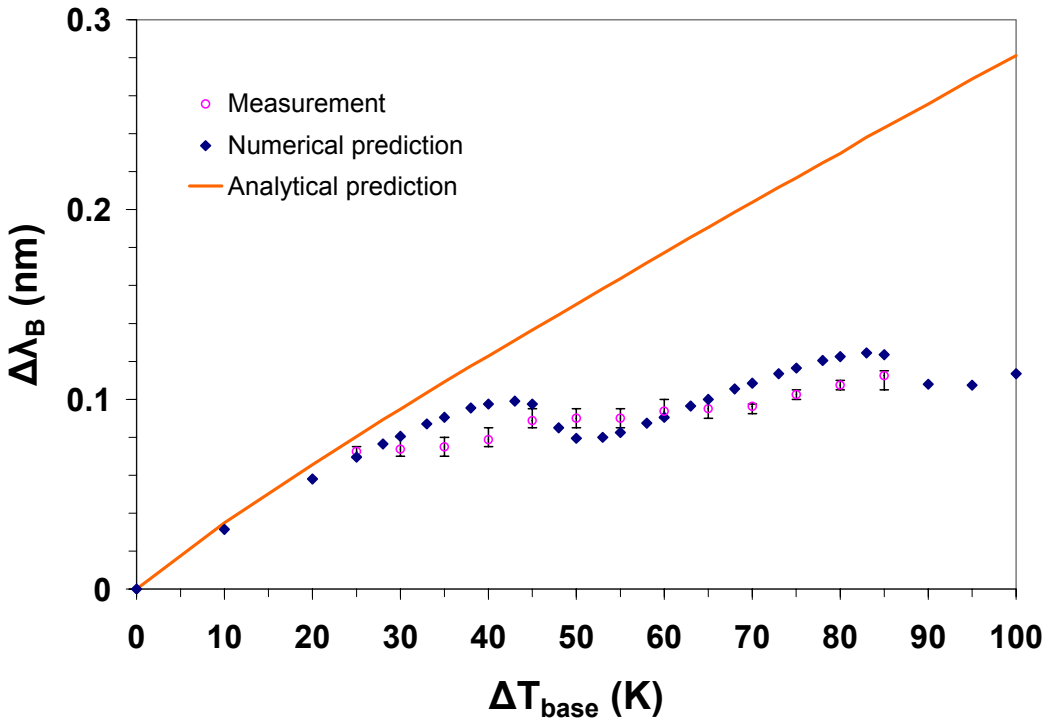

Figure 5.6: Measured/predicted shifts of Bragg wavelengths of a non-isothermal FBG

Figure 5.7 present normalized reflected power spectrums, both measured and predicted numerically, for the FBG base excess temperatures of 25 K to 85 K. The predicted spectrums show reasonably good agreements with the measured spectrums

despite some discrepancies in the higher orders of reflection. These discrepancies might be attributed to the assumptions in the numerical model, including the constant index modulation along the grating, the thermal independence of the index modulation, and the constant thermo-optical coefficient, as well as the possible difference between the temperature distribution used in the model (Figure 5.5) and the actual temperature distribution of the FBG.

It is worth noting that much wider spectral dispersion is observed in Figure 5.7 compared with the results of the isothermal FBG (Figure 5.4), and the degree of dispersion increases as the base temperature increases. Many peaks represent multiple local Bragg conditions, and the wavelength at each peak is the corresponding local Bragg wavelength. The large temperature gradient within the FBG creates the non-uniform index and grating pitch along the FBG, and consequently, results in the multiple Bragg resonances. Each Bragg condition results from the reflection by a certain portion of the total grating. The reflected power should be smaller than the reflected power of a single Bragg condition associated with the whole grating.

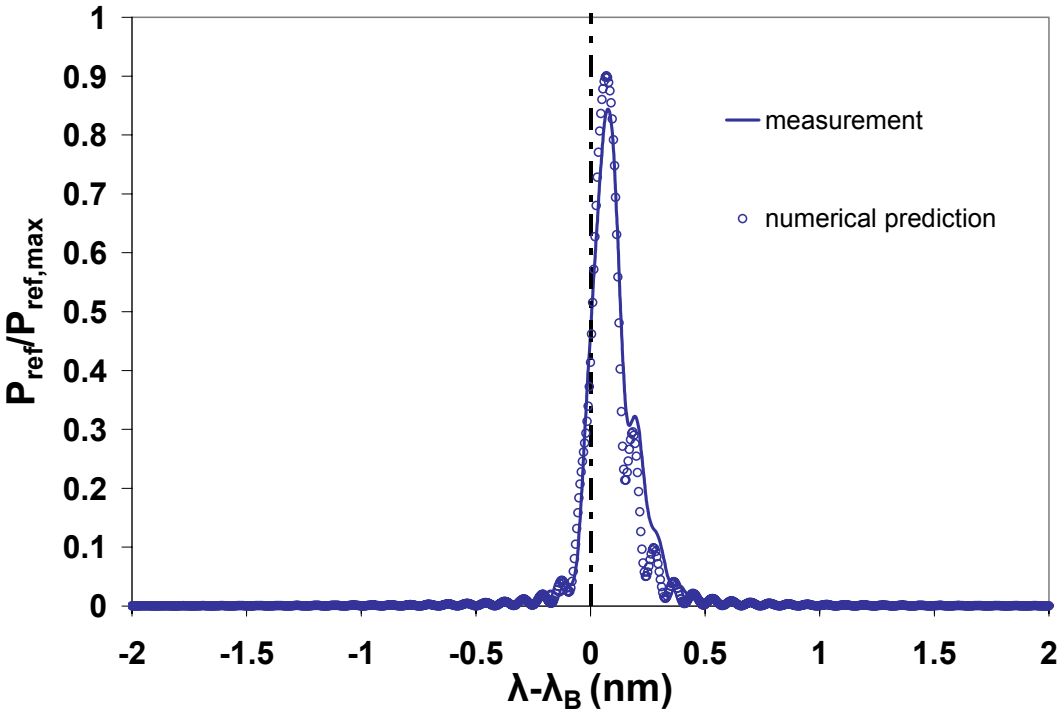
measurement
numerical prediction
$P_{ref}/P_{ref,max}$
$\lambda-\lambda_B$ (nm)
1
0.9
0.8
0.7
0.6
0.5
0.4
0.3
0.2
0.1
0
-2
-1.5
-1
-0.5
0
0.5
1
1.5
2

(a)

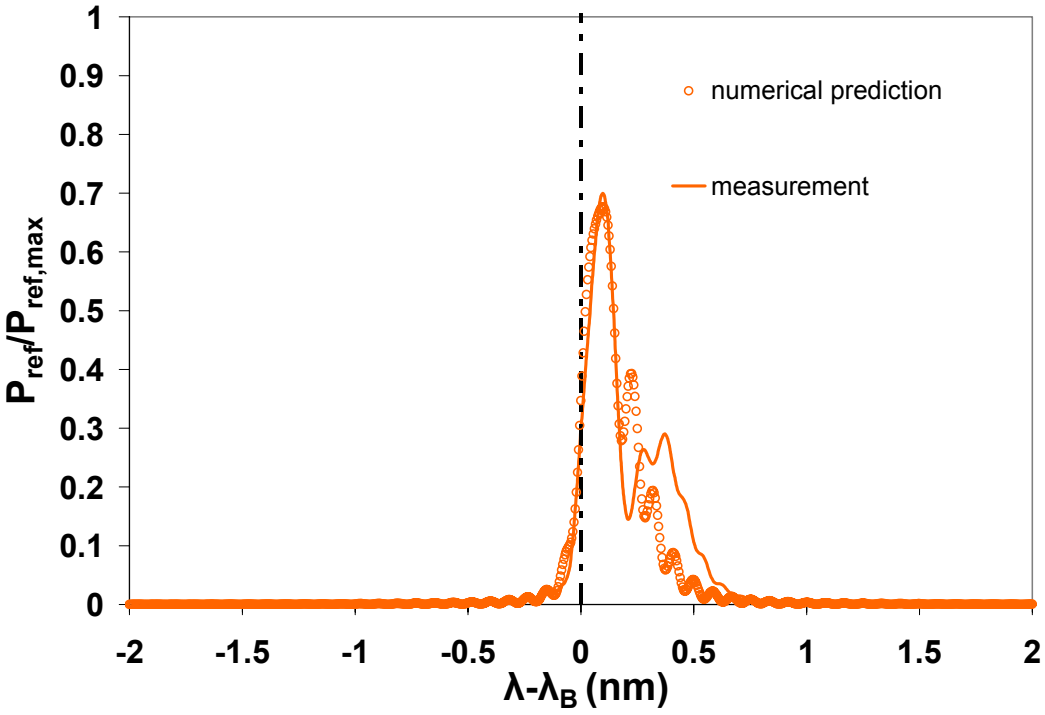
numerical prediction
measurement
$P_{ref}/P_{ref,max}$
$\lambda-\lambda_B$ (nm)
1
0.9
0.8
0.7
0.6
0.5
0.4
0.3
0.2
0.1
0
-2
-1.5
-1
-0.5
0
0.5
1
1.5
2

(b)

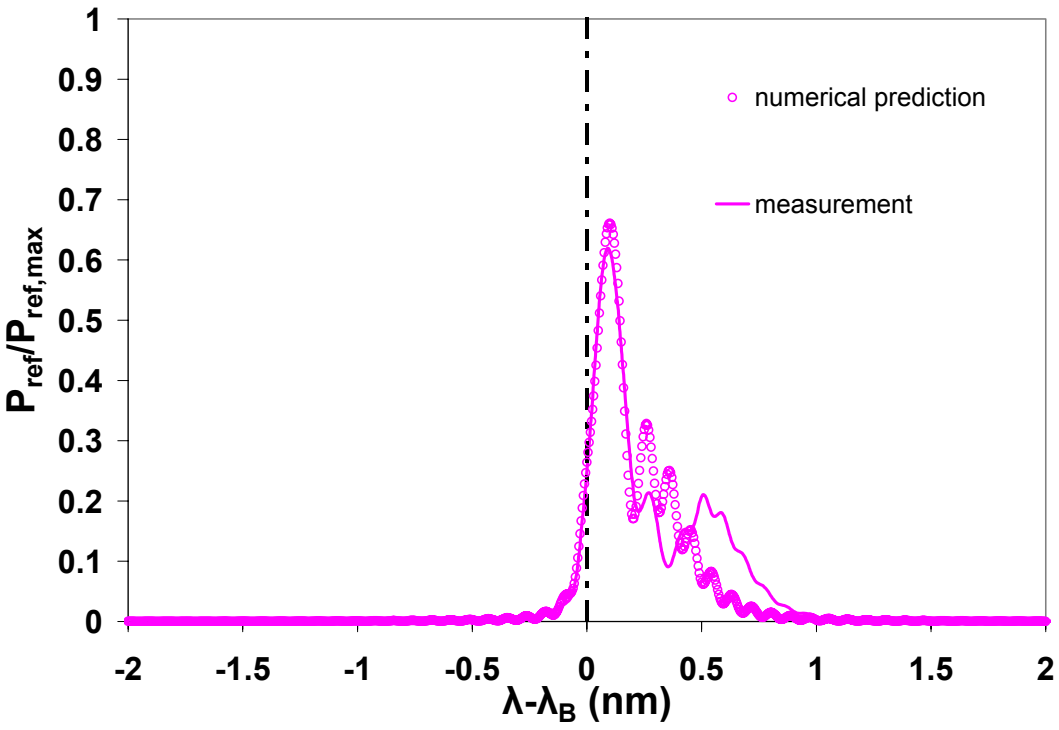

(c)

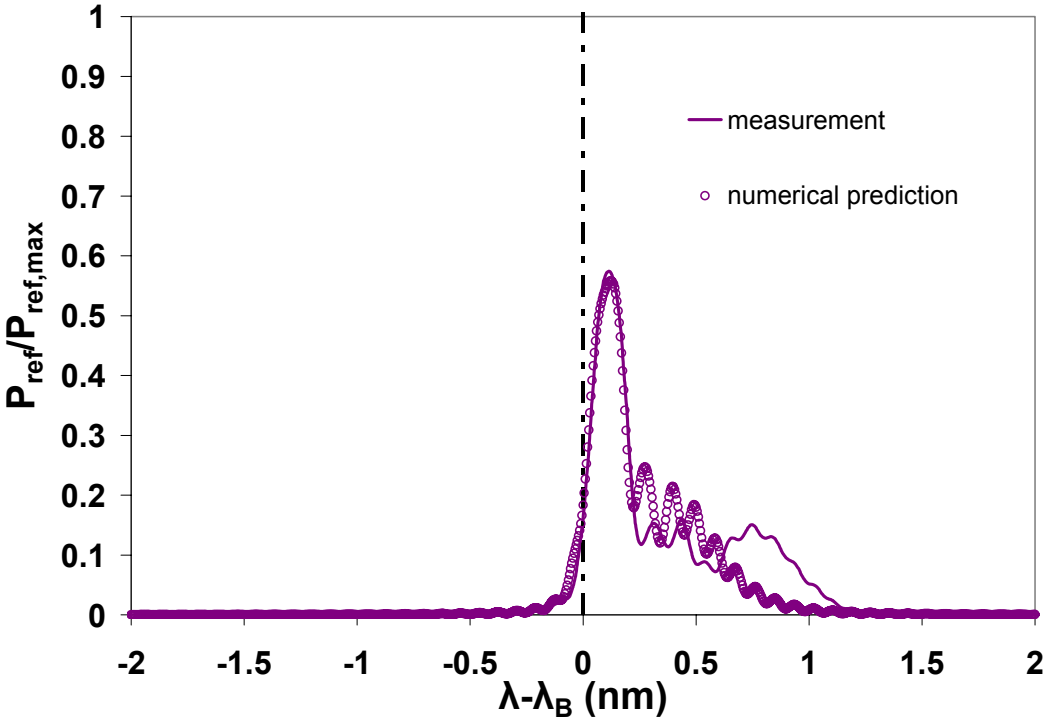

(d)

Figure 5.7: Measured/predicted normalized reflected power spectrums of a non-isothermal FBG at base temperatures of (a) 25, (b) 45, (c) 65, and (d) 85K

Chapter 6

Thermo-Optical Behavior of LED Illuminated PMMA FBG

To illustrate and concretize the polymer BG's thermo-optic behavior analyzed and described in Chapter 4, the present section will focus on the specific characteristics of a PFBG fabricated in Polymethylmetacrylate (PMMA), and illuminated by a broad-band LED. Section 6.1 describes the properties of the selected PMMA-based PFBG and the light sources. Section 6.2 presents the axial optical power variation, determined by the modified coupled-mode equations, through the PMMA FBG. Sections 6.3 and 6.4 apply the previously derived thermo-optic relations to the determination of the thermally-driven optical characteristics of the PMMA FBG with LED illumination.

6.1 Description of PMMA FBG and Light Source

In order to characterize the thermo-optical behavior of a PFBG, a PMMA FBG, described in the literatures [6, 49-50] was chosen. The selected PFBG was fabricated by the phase-mask technique. The detailed fabrication procedure can be found in [6, 49-50]. Table 4.1 shows all the inherent and derived parameters of the chosen PFBG, including the material properties and the structural, as well as optical parameters. The Bragg wavelength (λ_B), the grating period (Λ), the effective index (n_{eff}), and the maximum reflectivity ($\rho_{\max}$) are 1576.5 nm, 530.7 nm, 1.4853, and 0.745, respectively.

Typical power spectrums for a LED and a SMLD light sources were depicted in Figure 6.1. Figure 6.1 shows the specific power spectrums of a LED and a SMLD chosen for this study. The FWHMs for the LED and the SMLD are 50 nm and 0.026 nm,

respectively, and total power is 5 mW for each of the light sources. Consequently, the peak spectral power density for the SMLD, approximately 180 mW/nm, is nearly 2000 times greater than the 0.1 mW/nm peak spectral power density of the LED.

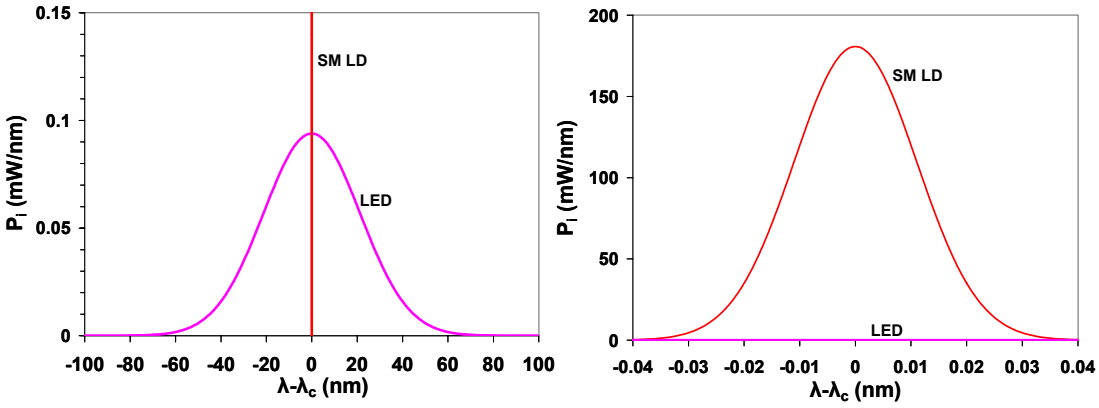

(a) (b)

Figure 6.1: Power spectrums of a light emitting diode and a single mode laser diode - 5 mW illumination (a) full Scale (b) expanded Scale

6.2 Power Variation along PMMA FBG

Equations (4.24) to (4.30), with the waveguide geometry and PMMA optical properties appearing in Table 4.1, were utilized to calculate the axial optical power distributions within the PFBG for various detuning values of $\Delta\lambda$ relative to the Bragg wavelength. The resulting non-dimensional power variations along the axis of the BG were previously discussed and are plotted in Figure 6.2, using the appropriate relations for each zone.

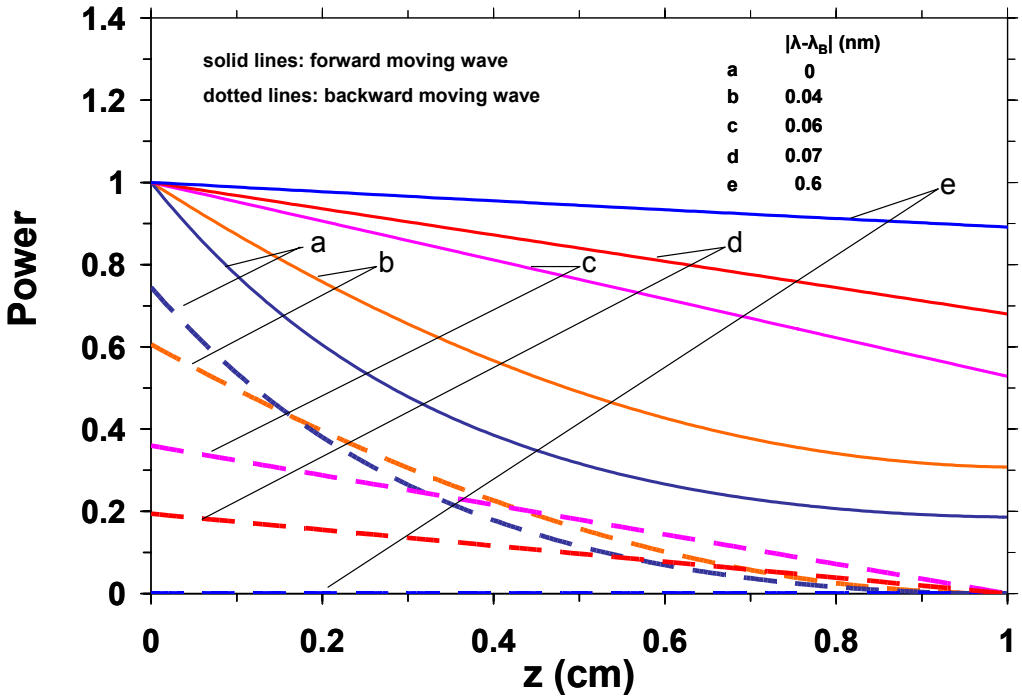

Figure 6.2: Incident and reflected powers along a PMMA Fiber Bragg Grating

The three optical coupling zones, i.e. Bragg, weak interaction, and waveguide, are clearly visible in this figure. At the Bragg condition, where the detuning is zero and the coupling is maximum, a significant power gradient exists in both forward and backward moving waves due to the tight energy coupling between the two waves. As attention is shifted away from the Bragg wavelength, detuning increases, resulting in reduced coupling and a progressive approach to simple light wave propagation along the optical fiber. As discussed before, $d\left(\left|R\right|^2\right)/dz > 0$ and $d\left(\left|S\right|^2\right)/dz > 0$, are used to define the boundary of the "Bragg zone" (zone I) and the beginning of the "weak interaction" zone (zone II) for a PMMA grating with the properties shown in Table 4.1**.** Within this boundary Eqs. (4.24) and (4.25) can be used, while beyond this boundary Eqs. (4.26) and (4.27) need to be used to assure negative axial gradients for $\left|S\right|^2$ and $\left|R\right|^2$.

The limiting detuning value, or grating bandwidth (zones I and II), beyond which the BG produces no significant reflection, was numerically determined by comparing the optical powers of the forward moving wave at the outlet of the grating obtained by the modified coupled-mode solution (Eq. 4.26) with those evaluated by the simple Beer's law (Eq. 4.28). Setting the difference in power at the outlet of the grating obtained with these two light propagation models at 1%, yields an absolute value of detuning, $|\delta|$, equal to or greater than 2.25×10^{-6} nm^{-1} which translates to an effective grating bandwidth of $\lambda - \lambda_B = \pm 0.6$ nm. Consequently, for wavelengths that exceed the Bragg wavelengths by 0.6 nm, i.e. $|\lambda - \lambda_B| \geq 0.6$ nm, the power variation can be found by Eq. (4.29).

6.3 Thermal Analysis

6.3.1 Heat generations

The spectral heat generation density, associated with the illumination of the PFBG by an LED, is shown in Figure 6.3, displaying the assumed symmetric Gaussian distribution with respect to the central wavelength and an FWHM of 50 nm. For incident optical powers of 0.5 to 5 mW, maximum spectral heat generation densities attain values of 0.7 to 7 Wcm^{-3}nm^{-1}.

Due to the broad-band illumination provided by the LED, extending substantially beyond the 0.6 nm bandwidth of the PFBG, to 1576 nm ± 100 nm (for 48 dB down from the peak power), an LED-illuminated Bragg grating operates almost exclusively in Zone III, where there is negligible optical coupling and the light propagates freely through the waveguide.

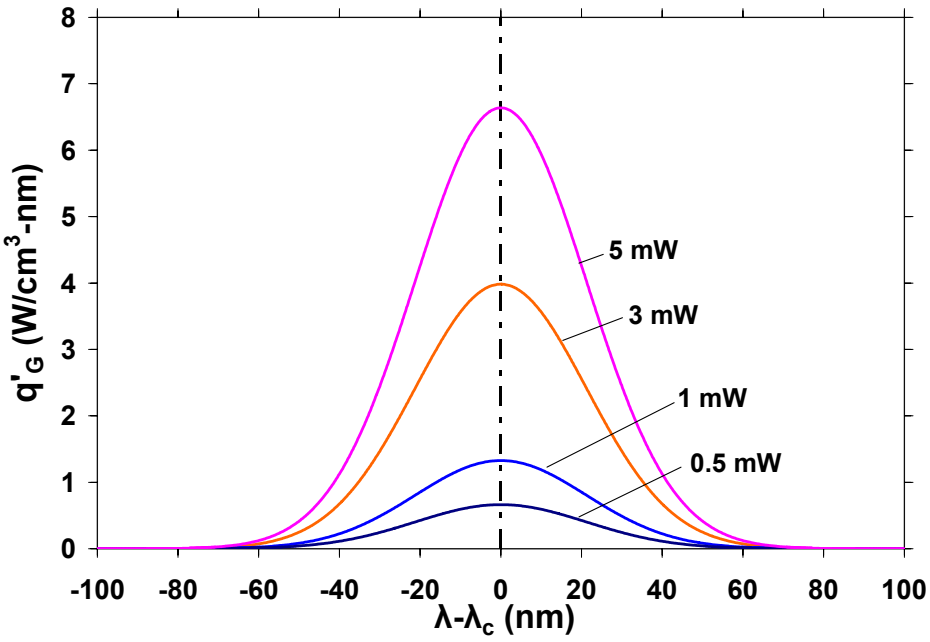

Figure 6.3: Spectral heat generation densities in a PMMA Fiber Bragg Grating illuminated by a light emitting diode

In this "waveguide" zone, heat generation in the fiber can be determined from the inherent absorption of the propagating beam, using Eq. (4.34). The resulting exponentially decaying axial profile of the heat generation along the PFBG is shown in Figure 6.4 for four different incident optical powers of 0.5, 1, 3, and 5 mW, reflecting the impact of the 11% light absorption in the one cm long fiber. It should be noted that the heat generation rates along the PFBG are significant, ranging from 30 W/cm^3 to 370 W/cm^3 for 0.5 to 5 mW of incident optical powers. A more precise calculation of the internal heat generation, using Eq. (4.34), revealed that including the reflected, backward moving light wave in the narrow spectral window of the grating bandwidth, $\left|\lambda - \lambda_B\right| \le 0.6$ nm, produced a negligible amount (< 0.01%) of additional heating in the fiber.

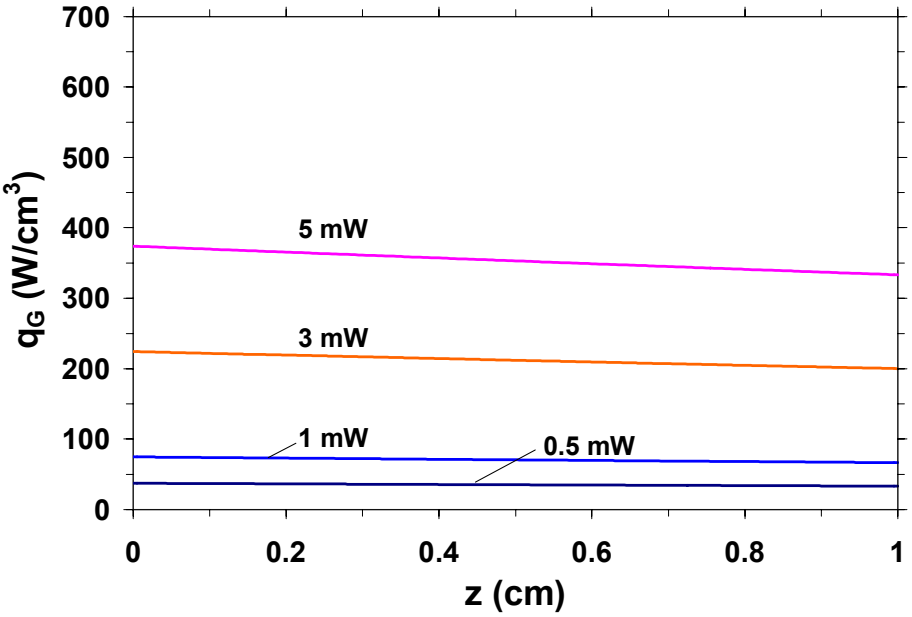

Figure 6.4: Heat generation densities along a PMMA Fiber Bragg Grating illuminated by a light emitting diode

6.3.2 Temperature profiles

The temperature distribution in a passively-cooled PFBG, resulting from LED illumination, was analytically determined using Eq. (4.41) and verified by comparison to results generated by the axisymmetric FEA simulation. The effective heat transfer coefficient, *h*, on the external surface of the volume representing the fiber was obtained by converting the combined convection and radiation heat transfer coefficient (approximately 10 $Wm^{-2}K^{-1}$) on the surface of the fiber, through radial conduction in the cladding and core [33]. The calculated effective heat transfer coefficient, *h*, for the condition described was 71 $Wm^{-2}K^{-1}$, or 335 W/m-K when applied to the length of the fiber in the axi-symmetric FEA model.

Figure 6.5 shows the PFBG axial profiles of the excess temperature (determined relative to a 25ºC ambient) for the four incident optical powers. The fiber excess temperatures vary from 18 K at the inlet of the fiber illuminated with the highest incident power of 5 mW to just 2 K for the 0.5 mW. The analytical and FEA results display the anticipated, though barely discernable, exponential decay and appear to match each other extremely well, typically within 0.7 %.

The finite-element model was further utilized to calculate the radial temperature variations in the PFBG. The results are shown in Figure 6.6, where the axial variation of the temperature difference $(T_c - T_{co})$ between the center of the PFBG core $(T_c)$and the core surface (T_{co}) is plotted. The peak radial temperature differences are seen to range from 0.06 K at 5 mW to 0.01 K at 0.5 mW of incident LED power and thus justify the radially-uniform temperature assumption used in the analytical temperature relations. Figure 6.6 also reveals a slight decrease in the radial temperature difference as the PFBG is traversed from the inlet to the outlet end. It should, nevertheless, be noted that, due to the 7 μm diameter of the PFBG, these radial temperature variations do yield significant temperature gradients.

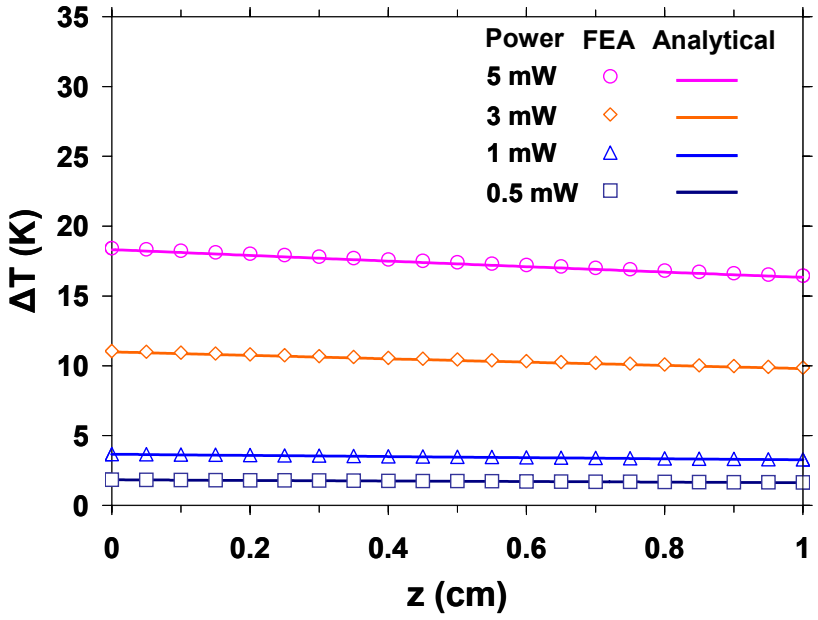

Figure 6.5: Analytical and numerical excess temperatures along a PMMA Fiber Bragg Grating illuminated by a light emitting diode

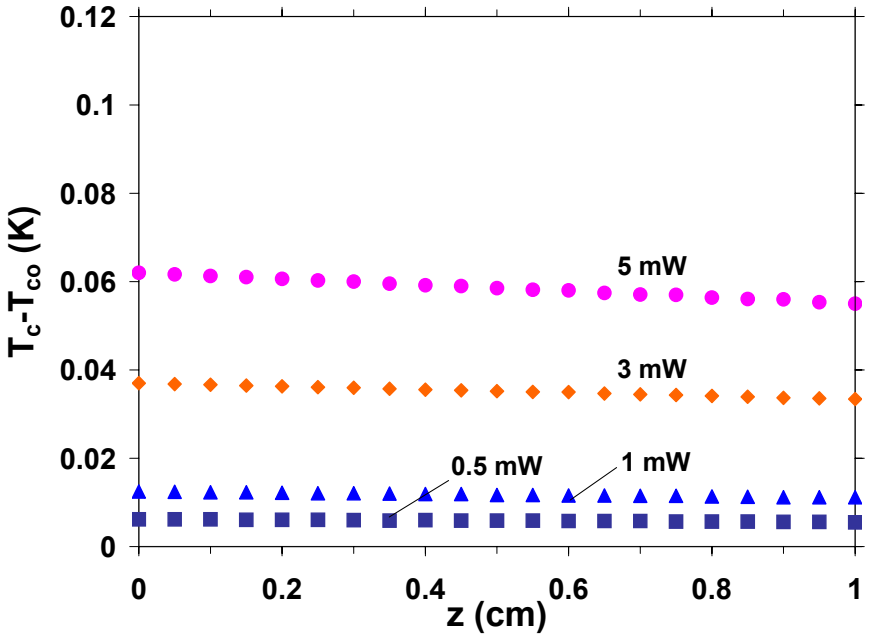

Figure 6.6: Radial temperature differences along a PMMA Fiber Bragg Grating illuminated by a light emitting diode

6.4 Thermo-Optical Analysis

6.4.1 Reflectivity spectra

In order to obtain the reflectivity spectrum of the specified PFBG associated with the LED, the temperature distribution obtained from Eq. (4.41) was integrated with the modified TMM relations (Eqs. 4.46 and 4.47). In the TMM implementation, a total of 200 segments, each 50 μm wide, was used, along with wavelength bands of 0.5 pm. Figure 6.7 displays the thermally-induced shift in the spectral reflectivity of the specified PFBG illuminated with 5 mW to 0.5 mW of LED powers and operating in an ambient temperature of 25°C. The individual effects of the index change with temperature, (dn/dT), and the grating period change with temperature, $(d\Lambda/dT)$, were determined.

The results clearly indicate that the thermally-driven index change produces a negative shift in the reflectivity spectrum, relative to the incident 1576.5 nm-centered LED light. At 5mW of the LED illumination, the dominant "Bragg" wavelength moves lower by -2.03 nm as shown in Figure 6.7(a). The change of the grating period due to thermal expansion results in a positive shift in the reflectivity spectrum, driving the dominant wavelength to higher values by 2.0 nm. The combined reflectivity spectrum for the 5 mW illuminated fiber shows a very small total shift in Bragg wavelength (-0.03 nm), with modest spectral dispersion. Figures 6.7 (b) to (d) show the individual and the combined reflectivity spectrums for 3 mW to 0.5 mW of the LED illuminations. The combined reflectivity spectrums for these illuminations show similarly small total shifts in Bragg wavelength of -0.02 nm, -0.006 nm, and -0.003 nm for 3 mW, 1 mW, and 0.5 mW of the total optical power, respectively.

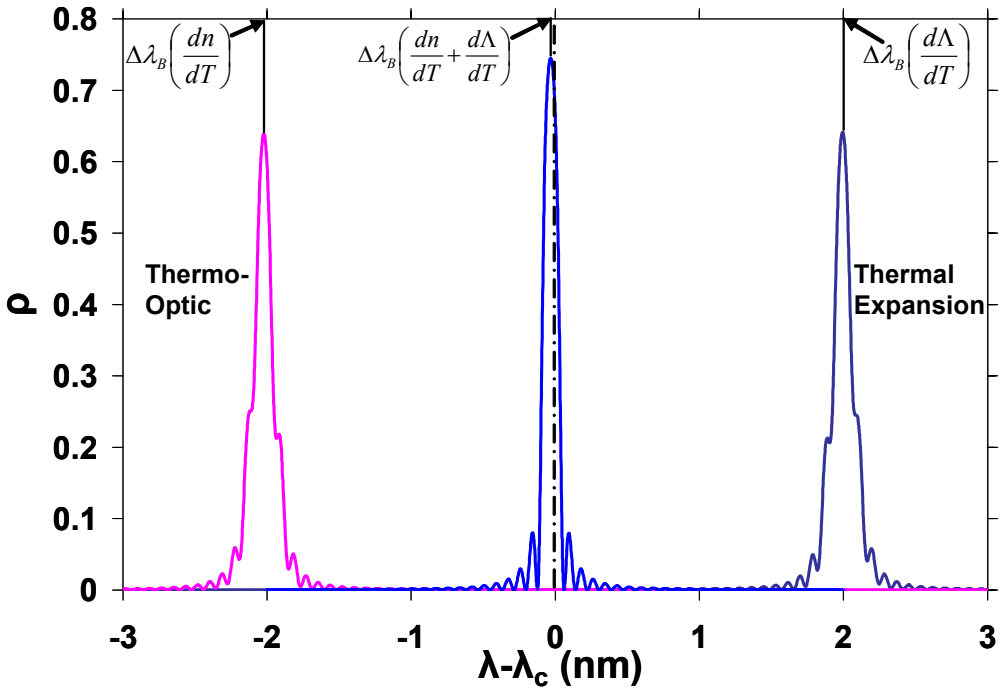

(a)

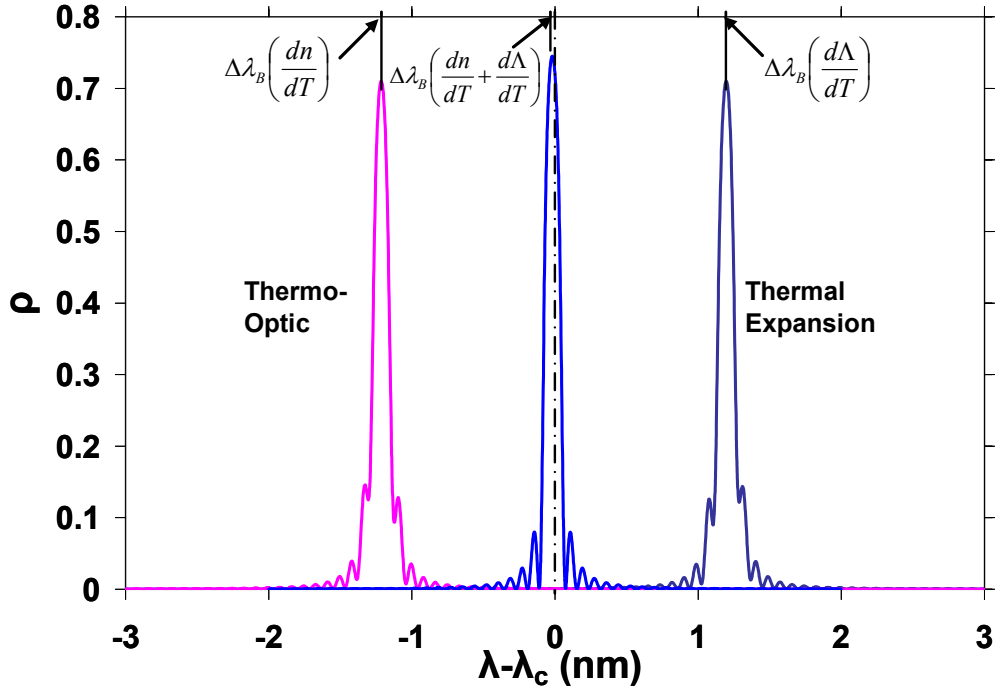

(b)

Figure 6.7 (Con't)

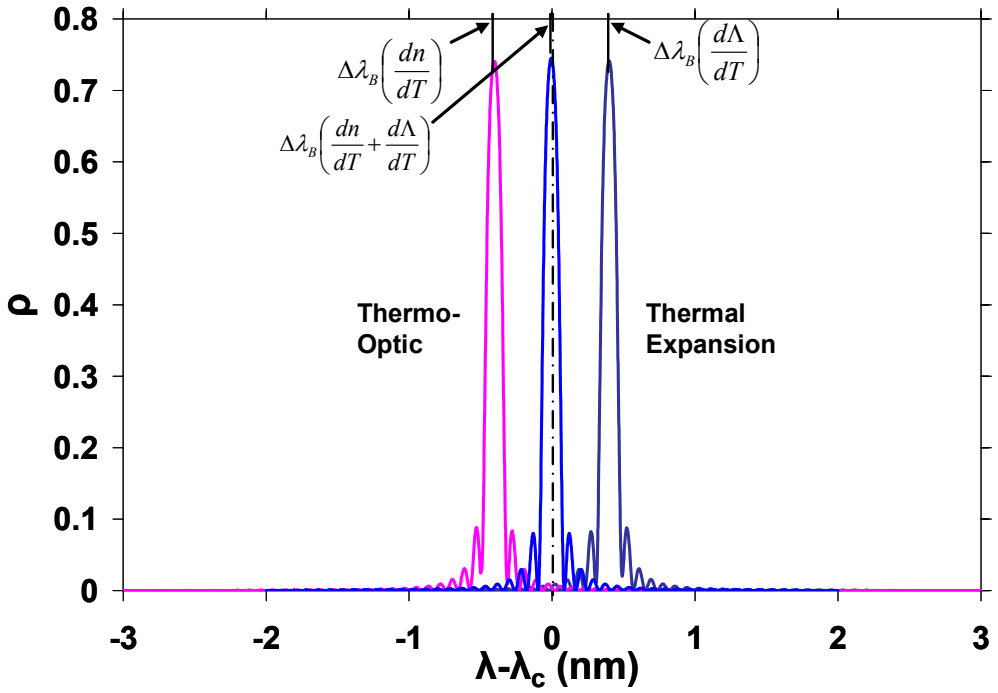

(c)

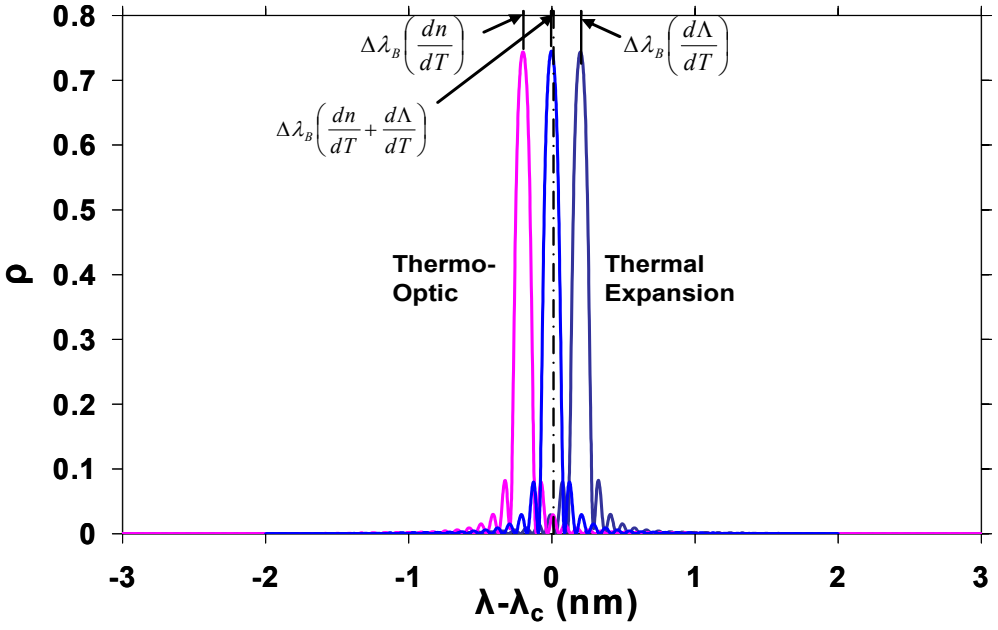

(d)

Figure 6.7: Thermally-induced Bragg wavelength shifts a in PMMA Fiber Bragg Grating illuminated with a light emitting diode – thermo-optic (dn/dT), thermal expansion ($d\Lambda/dT$), and combined effects ($dn/dT + d\Lambda/dT$) for (a) 5 mW, (b) 3 mW, (c) 1 mW, and (d) 0.5 mW of incident optical powers

The previously noted, spectral compensation, which results from the comparable magnitude, though opposite sign, of the two individual effects, is in clear evidence in this reflectivity spectrum. The jagged character of the reflectivity spectrum is associated with the spectral dispersion induced by the axially non-uniform PFBG temperature.

The total reflectivity spectrums, including both the thermal expansion and index change with temperature, are displayed with an expanded wavelength scale in Figure 6.8, for 0.5 mW and 5mW of LED illuminations. The total reflectivity spectrums show a consistent reflectivity shape with the constant FWHM of 0.12 nm, a maximum reflectivity of 0.74, and a small Bragg wavelength shift in the negative direction for each incident optical power.

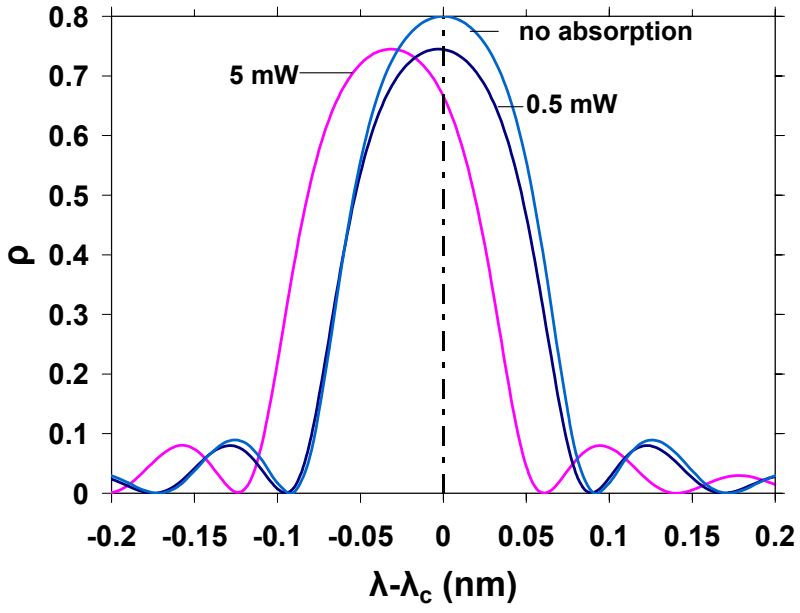

Figure 6.8: Reflectivity spectrums of a PMMA Fiber Bragg Grating for a light emitting diode illumination

6.4.2 Reflected power spectra

Although the rigorously evaluated reflectivity spectra provide useful information on the spectral dependence of the reflectivity and the Bragg wavelength shifts, due to the Gaussian spectral distribution of the incident LED illumination, they may not represent the character of the reflected powers. To obtain reflected power spectra and the power-based Bragg wavelength shift, it is, thus, necessary to perform a convolution of these two distributions (i.e., Gaussian illumination and coupled-mode reflectivity).

Figure 6.9 shows the reflected power spectra for the four incident optical powers, obtained the convolution using Eqs. (4.52) and (4.53) when the ambient temperature is 25 ºC. Due to the wide-band LED source, the reflected power spectrums present similar profiles to those of the reflectivities alone, with nearly identical negative shift in the dominant wavelength.

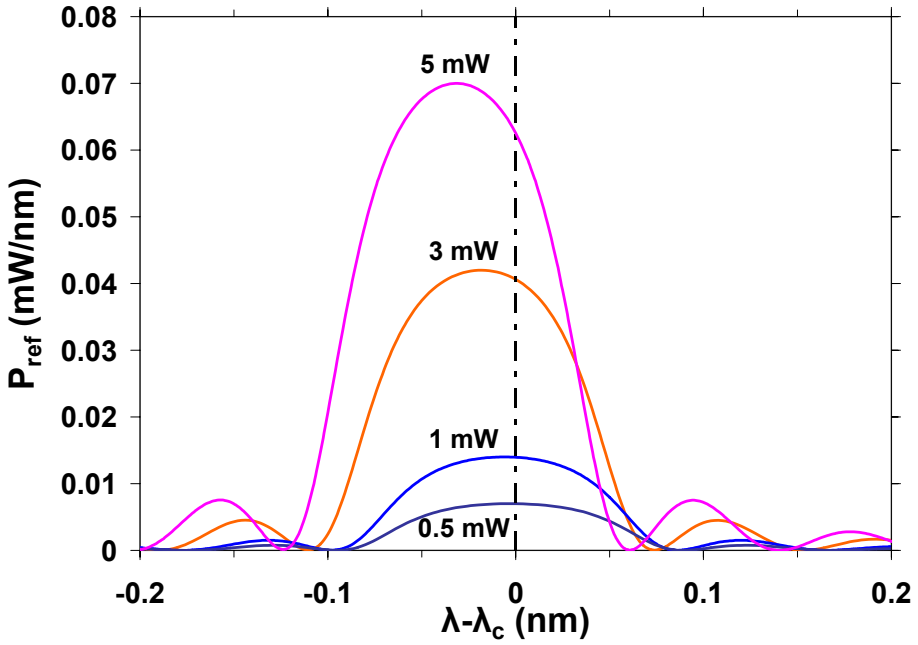

Figure 6.9: Reflected power spectra for the light emitting diode illumination of a PMMA Fiber Bragg Grating

6.4.3 Parametric effects on $\Delta\lambda_B$

The Bragg wavelength shift is, perhaps, the single most important parameter used to characterize the thermo-optical behavior of a PFBG. This Bragg wavelength shift is driven by the temperature change in the PFBG induced by both absorption and the ambient temperature change. Figure 6.10 shows the shifted Bragg wavelengths in an ambient varying from 25 ºC to 45 ºC and for four incident optical powers. The results were obtained using both the modified-TMM (the methodology used to produce the spectral reflectivity variations displayed in Figure 6.8) and Eq. (4.45), with an axially-averaged PFBG temperature.

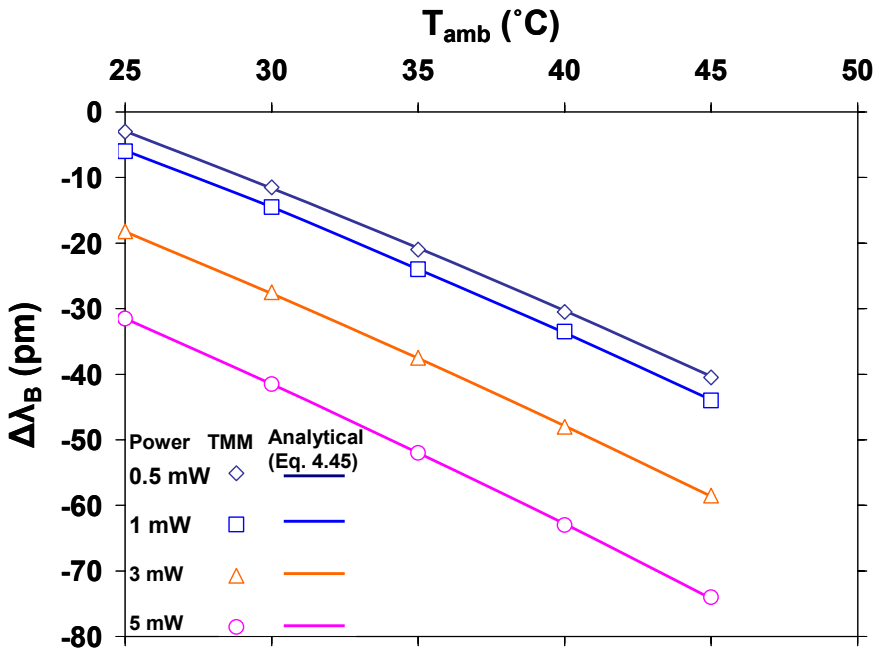

Figure 6.10: Bragg wavelength shifts in a PMMA Fiber Bragg Grating illuminated with a light emitting diode

The analytically determined Bragg wavelength shifts, including the quadratic term in Eq. (4.45) and based on the axially-averaged temperatures, are seen to agree very well (typically to within better than 1 %), with the values extracted from the more detailed

modified TMM methodology. The less accurate linear superposition formulation, given by Eq. (3.1), yields a 2 % to 18 % discrepancy with those determined by the TMM. The Bragg wavelength shifts calculated by all 3 methods are presented in Table 6.1. The significant effect of ambient temperature on the shift in Bragg wavelength is also evident, with a 15 K ambient temperature rise yielding a $\Delta\lambda_B$ almost equivalent to that of the incident power increase from 0.5 mW to 5 mW.

Table 6.1: Bragg wavelength shifts in a PMMA Polymer Fiber Bragg Grating with a light emitting diode illumination

Ambient temperature T_{amb}	Incident optical power, $P_{inc}\ (mW)$	Average excess temperature $\overline{\Delta T}\ (K)$	Transfer Matrix Method (pm)	Quadratic -Eq. 4.45 (pm)	Linear -Eq. 3.1 (pm)
25	0.5	1.73	-3	-2.9	-2.9
25	1	3.46	-6	-5.9	-5.8
25	3	10.38	-18.2	-18.3	-17.3
25	5	17.31	-31.5	-31.5	-28.9
30	0.5	6.73	-11.5	-11.6	-11.2
30	1	8.46	-14.5	-14.5	-14.1
30	3	15.38	-27.5	-27.7	-25.7
30	5	22.31	-41.5	-41.5	-37.3
35	0.5	11.73	-21	-20.8	-19.6
35	1	13.46	-24	-24	-22.5
35	3	20.38	-37.5	-37.6	-34.0
35	5	27.31	-52	-52	-45.6
40	0.5	16.73	-30.5	-30.3	-27.9
40	1	18.46	-33.5	-33.7	-30.8
40	3	25.38	-48	-47.9	-42.4
40	5	32.31	-63	-62.8	-53.9
45	0.5	21.73	-40.5	-40.3	-36.3
45	1	23.46	-44	-43.9	-39.2
45	3	30.38	-58.5	-58.6	-50.7
45	5	37.31	-74	-74.2	-62.3

Figure 6.11 presents the estimated shifts of Bragg wavelengths by the TMM with non-uniform temperature, TMM with uniform temperature, quadratic analytical method, and linear analytical method. The results confirm that the Bragg wavelength shifts are governed mainly by the average temperatures and the temperature gradients have a negligible effect.

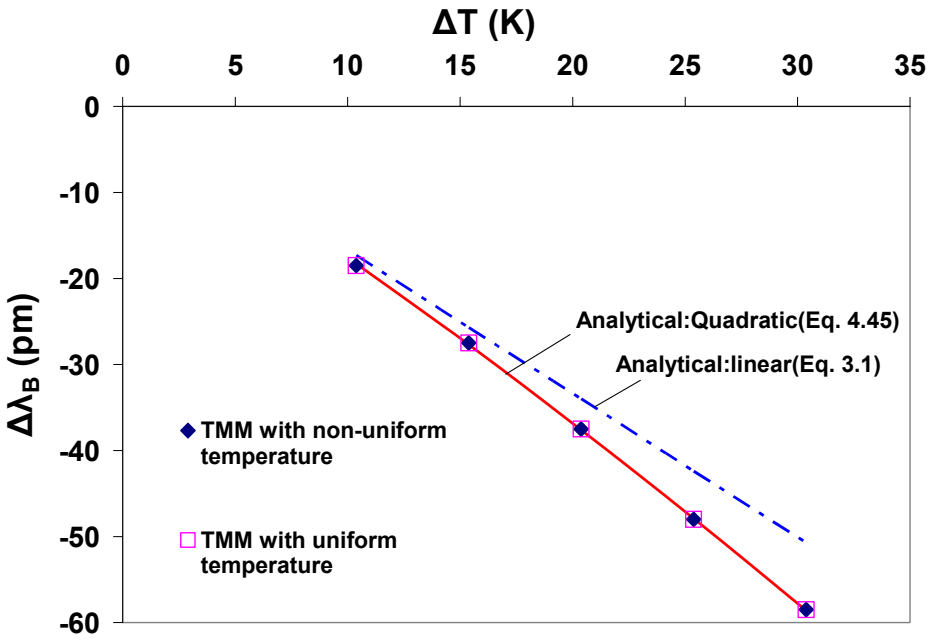

Figure 6.11: Transfer Matrix Method Bragg wavelength shifts – axially uniform and non-uniform temperatures

Chapter 7

Thermo-Optical Behavior of SMLD Illuminated PMMA FBG

7.1 Solution Procedure for Fully Coupled Thermo-Optical Analysis

Unlike a broad-band LED light source studied in the previous chapter, heat generation associated with single mode laser diode (SMLD) illumination (FWHM of less than 0.3 nm) strongly depends on the coupling between the forward and backward moving waves. Furthermore, the Bragg wavelength shift will be of the same magnitude as the FWHM. Consequently, the thermal and thermo-optical analyses must be performed in a fully coupled way.

The spectral bandwidths of the chosen SMLD light sources are 0.001, 0.026, and 0.1 nm. The spectral bandwidths of the first two SMLDs are smaller than the boundary of zone I while the bandwidth of the third one is greater than the boundary of zone I. For the first two SMLDs, the closed-form solutions of the coupled-mode equations (Eqs. 4.24 and 4.25) are employed to complete the analysis. For the third SMLD, however, the modified solutions of the coupled-mode equations (Eqs. 4.26 and 4.27) are needed to handle zone II.

The fully coupled model must satisfy an energy balance, $P_{inc} - P_{out} = P_G$, where P_{inc}, P_{out}, and P_G are the incident total optical power, the total optical power at the outlet, and the generated total heat, respectively. The optical power and the heat generation depend on the Bragg wavelength, which in turn, depends on the temperature. To deal with this additional interdependence, the following iterative procedure, outlined in Figure 7.1, was established to determine the Bragg wavelength at which this energy balance could be attained.

(1) Obtain the heat generation along the FBG by Eq. (4.33) based on the original Bragg wavelength.

(2) Determine the temperature distribution along the FBG by the analytical thermal model (Eqs. 4.43 and 4.44).

(3) Obtain the spectrum of the reflected optical signal by the thermo-optical model (Eqs. 4.46 and 4.47)

(4) Determine the new Bragg wavelength and the Bragg wavelength shift from the reflectivity spectrum.

(5) Repeat (1) to (4) with the new Bragg wavelength until the difference of the used Bragg wavelength from (1) to (3) and the obtained Bragg wavelength at (4) converges virtually to "zero".

Step (5) ensures the energy balance in the FBG. The heat generation, temperature distribution and the spectral information of the reflected optical signals are determined using the converged Bragg wavelength.

7.2 Thermal Analysis

SMLD light sources with three different spectral bandwidths were analyzed: they will be referred to as SMLD I (0.001 nm), II (0.026 nm) and III (0.1 nm). For each SMLD light source, four optical powers were considered for analyses. The results will be presented in the following format; each figure contains three plots which represent the three sources with different spectral bandwidths. Each plot contains results from the cases of four different powers (0.5, 1, 3 and 5 mW). Thermal solutions associated with the

modified closed-form coupled-mode solutions are compared with those associated with the purely closed-form coupled-mode solutions (Eqs. 4.24 and 4.25) for SMLD III.

7.2.1 Heat generations

Spectral heat generation densities, associated with SMLD illuminations, are shown in Figures 7.2. It is to be noted that the results for the 0.1nm SMLD III, displayed in Figure 7.2(c), reflect a greater contribution of the "weak interaction zone" and the modified closed-form coupled-mode solutions than the other two SMLD's considered in this study. For the SMLD with the smallest spectral bandwidth of 0.001 nm, the spectral heat generation densities have perfect symmetry like those with the LED illumination. The spectral distributions of the heat generations become asymmetric as the spectral bandwidth of SMLD increases. These observable shifts in the spectral distribution of generated heat were caused by the reduced coupling between the incident and reflected waves as well as the strong spectral variation of the incident light. Figures 7.2(c) and 7.3 demonstrate that only small discrepancies, with an average discrepancy of 5%, exist in spectral heat generation densities determined by the use of the modified closed-form coupled–mode solutions (solutions for zones I and II) relative to those evaluated by the use of the purely closed-form coupled-mode solution.

Heat generations along the Bragg grating associated with the SMLD illuminations were determined by Eq. (4.33) and the results are shown in Figure 7.4. It may again be noted that the results for the 0.1nm SMLD III, displayed in Figure 7.4(c), reflect a greater contribution of the "weak interaction zone" and the modified closed-form coupled-mode solutions than the other two SMLD's considered in this study. The exponential decay of the heat generation rate is evident. For the same reason (the reduced coupling), SMLD

III shows small but discernable differences in heat generation rate while the heat generations of SMLD I is nearly identical to those of SMLD II.

The heat generation density at the inlet of SMLD III, peaking at 580 W/cm^3 for 5 mW, is approximately 10 % smaller than those of SMLD I and II. The axial heat generation gradients are also smaller. The integrated result of the smoother power spectrum and the smaller reflected power, induced by the less light energy coupling associated with the greater detuning value, can explain the smaller peak heat generation with the less axial gradient for the wider illumination. In addition, it should be noted that the heat generation densities at the inlet of SMLD I and II, peaking at 640 W/cm^3 for 5 mW, are approximately 70 % greater than those of the LED. As a result, the axial heat generation gradients of SMLD illuminations are proportionally larger. Figures 7.4 (c) and 7.5 show a clear evidence that two solutions (the modified and purely closed-form coupled-mode solutions) predict very similar rates of heat generation densities with an average discrepancy of 5 %.

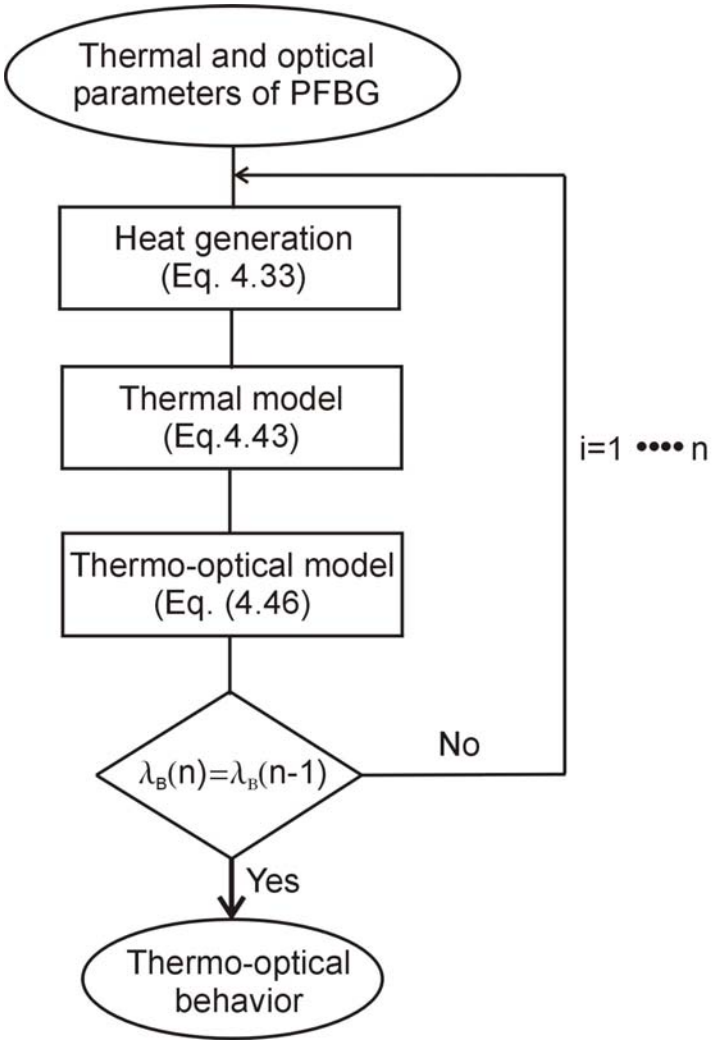

Figure 7.1: Iterative solution procedure - fully coupled thermo-optical analysis

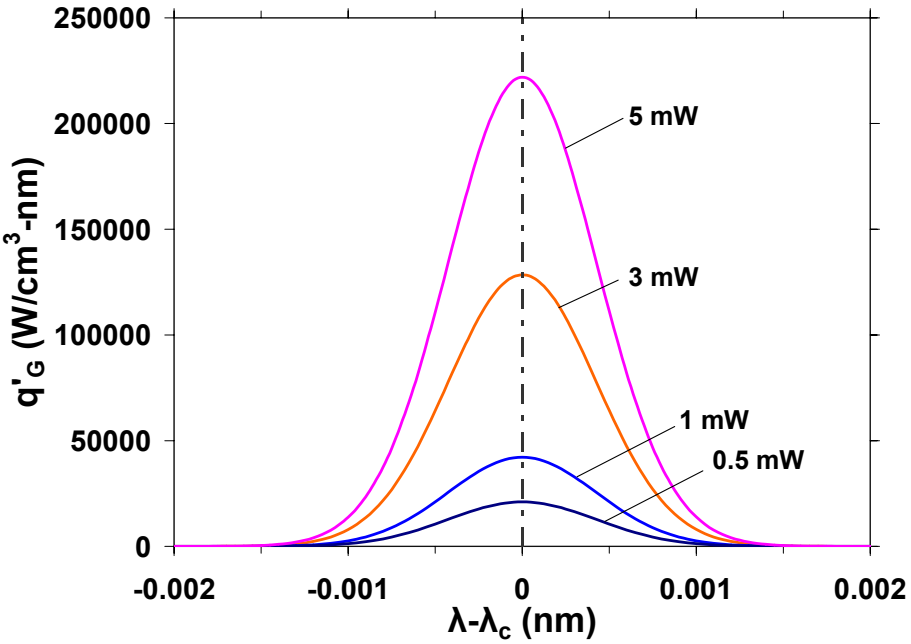
250000
200000
150000
100000
50000
0
-0.002
-0.001
0
0.001
0.002
q'G (W/cm3-nm)
λ-λc (nm)
5 mW
3 mW
1 mW
0.5 mW

(a)

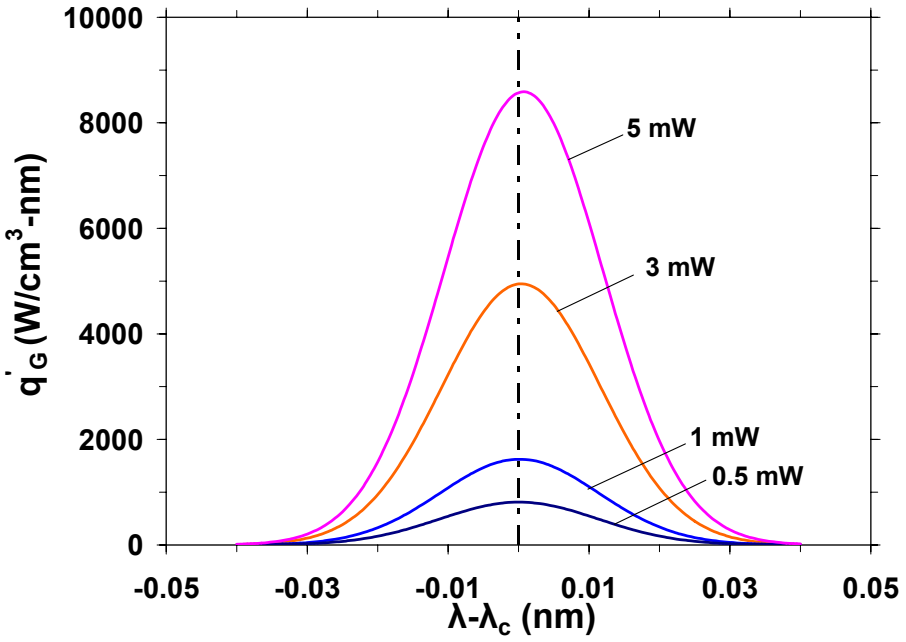
10000
8000
6000
4000
2000
0
-0.05
-0.03
-0.01
0.01
0.03
0.05
q'G (W/cm3-nm)
λ-λc (nm)
5 mW
3 mW
1 mW
0.5 mW

(b)

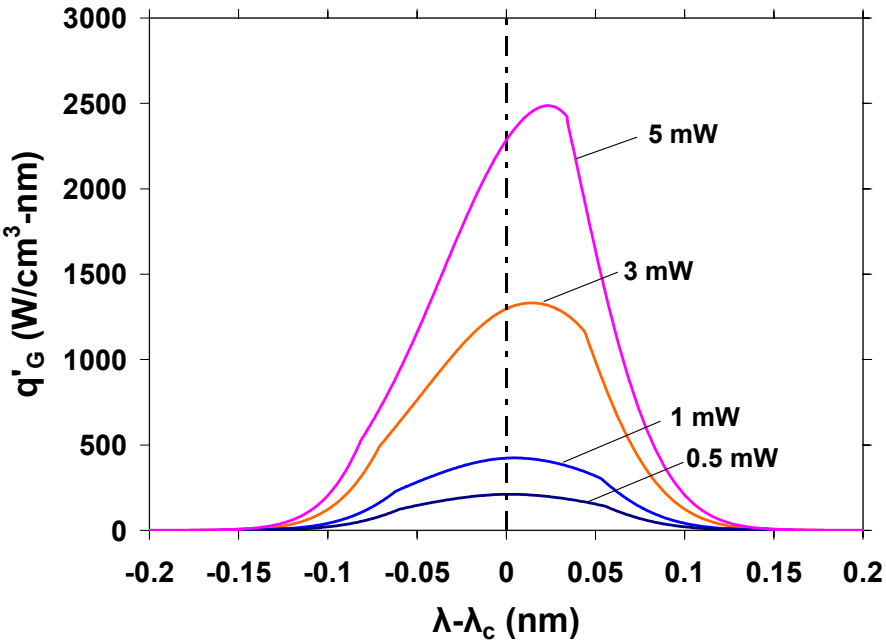

(c)

Figure 7.2: Spectral heat generation densities in a PMMA Fiber Bragg Grating illuminated by single mode laser diodes with spectral bandwidths of (a) 0.001 nm (b) 0.026 nm (c) 0.1 nm at ambient of 25°C

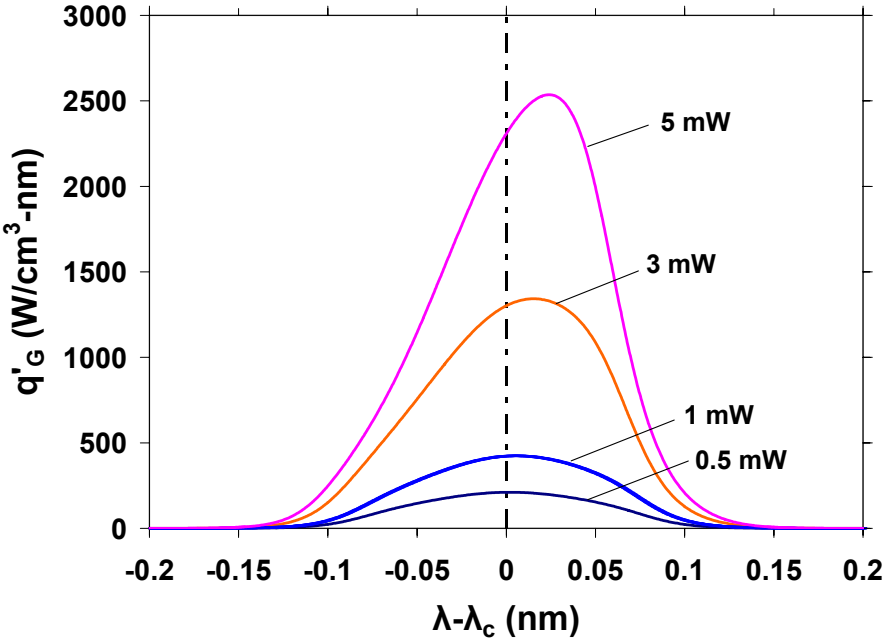

Figure 7.3: Spectral heat generation densities in a PMMA Fiber Bragg Grating illuminated by a single mode laser diode with a spectral bandwidth of 0.1 nm at ambient of 25°C. The solution is associated with the powers, determined by the purely closed-form coupled-mode solutions (Eqs. 4.24 and 4.25), along the grating.

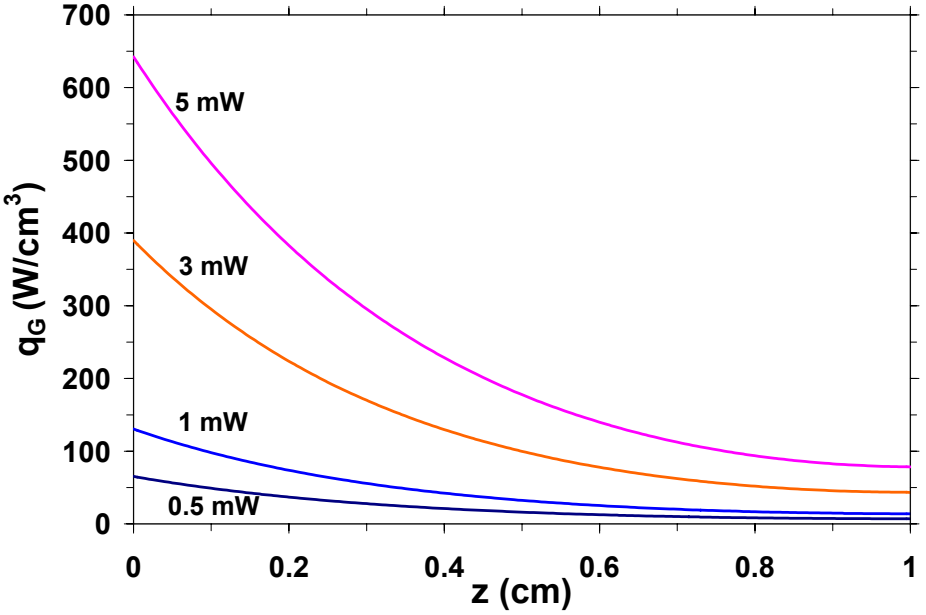
700
600
500
400
300
200
100
0
q_G (W/cm^3)
5 mW
3 mW
1 mW
0.5 mW
0
0.2
0.4
0.6
0.8
1
z (cm)

(a)

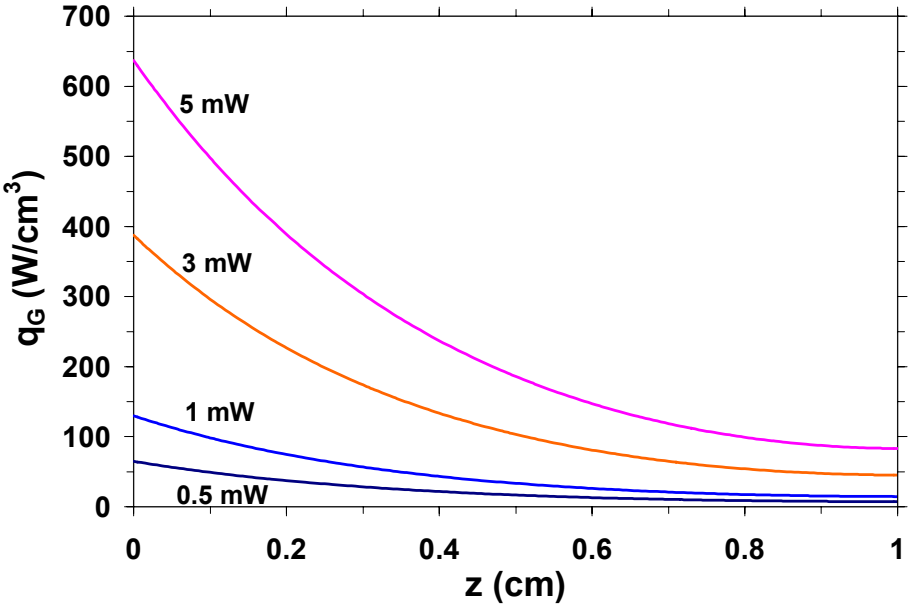
700
600
500
400
300
200
100
0
q_G (W/cm^3)
5 mW
3 mW
1 mW
0.5 mW
0
0.2
0.4
0.6
0.8
1
z (cm)

(b)

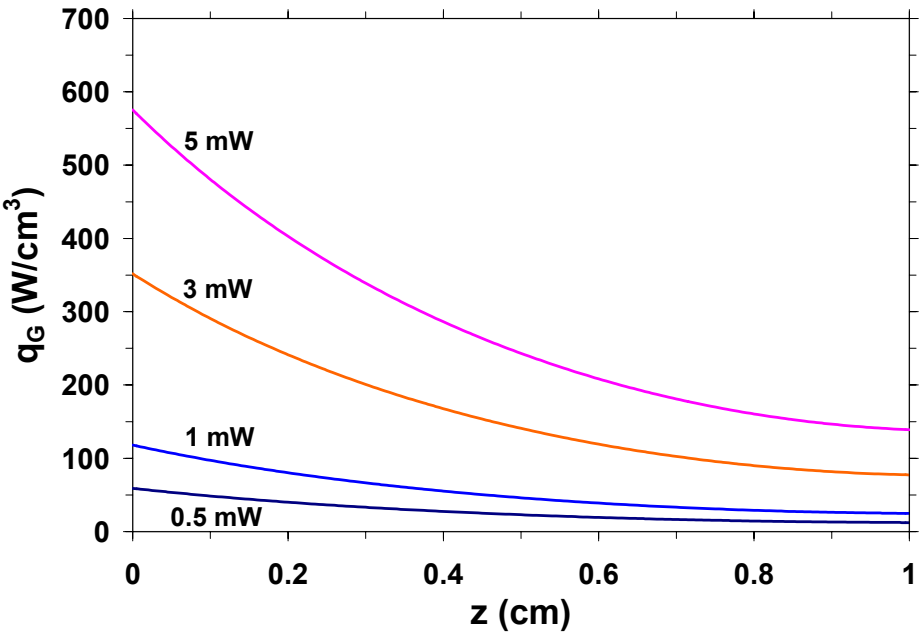

(c)

Figure 7.4: Heat generation densities along a PMMA Fiber Bragg Grating illuminated by single mode laser diodes with spectral bandwidths of (a) 0.001 nm (b) 0.026 nm (c) 0.1 nm at ambient of 25°C

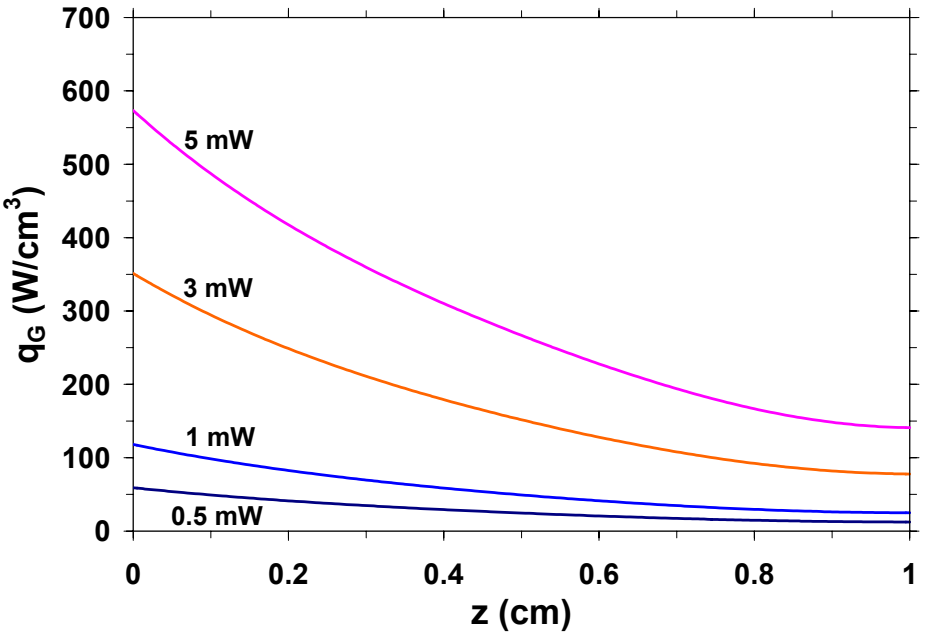

Figure 7.5: Heat generation densities along a PMMA Fiber Bragg Grating illuminated by a single mode laser diode with a spectral bandwidth of 0.1 nm at ambient of 25°C. The solution is associated with the powers, determined by the purely closed-form coupled-mode solutions (Eqs. 4.24 and 4.25), along the grating.

7.2.2 Temperature profiles

Since the powers of SMLD I and II are contained well within the bandwidth of the PFBG, the entire spectrum of the incident wave experiences Bragg reflections from the grating, drastically reducing the amount of light propagating to the outlet end of the grating. Using the internal heat generation profiles, it is now possible to determine the temperature variations within the PMMA FBG using Eqs. (4.43) and (4.44) as well as the previously described finite-element model.

An integral term associated with only $\lambda_2 \le \lambda \le \lambda_3$ (zone I) was evaluated for SMLD I and II. For SMLD III, however, a considerable amount of power is included in zone II. Consequently, temperature solutions of Eqs. (4.43) and (4.44) were obtained utilizing zone I and zone II ($\lambda_1 \le \lambda < \lambda_2$ and $\lambda_3 < \lambda \le \lambda_4$).

Figure 7.6 shows the PMMA FBG axial profiles of the excess temperatures (relative to 25ºC ambient). The results for SMLD III in Figure 7.6(c) are most reflective of the contribution of the weak interactions encountered for large detuning values and incorporated into the modified closed-form coupled-mode solutions. As expected from the degree of coupling, the excess temperature profiles of SMLD I are almost identical to those of SMLD II. Peak temperatures of SMLD III are about 10 % lower than those of SMLD I and II.

The results reveal that the inlet of the SMLD illuminated PMMA FBG experiences significant heating, reaching excess temperatures of 31 K to 28 K at 5 mW and 7 K to 3 K even at just 0.5 mW of incident power. They are significantly higher than the peak temperatures induced by the LED illumination. Further reinforcing the strong optical coupling between the incident and reflected waves, however, the average

temperature rises of the specified PMMA PFBG induced by SMLD illuminations are lower than the comparable values for the LED illumination; approximately 20 % for SMLD III and 30 % for SMLD I and II.

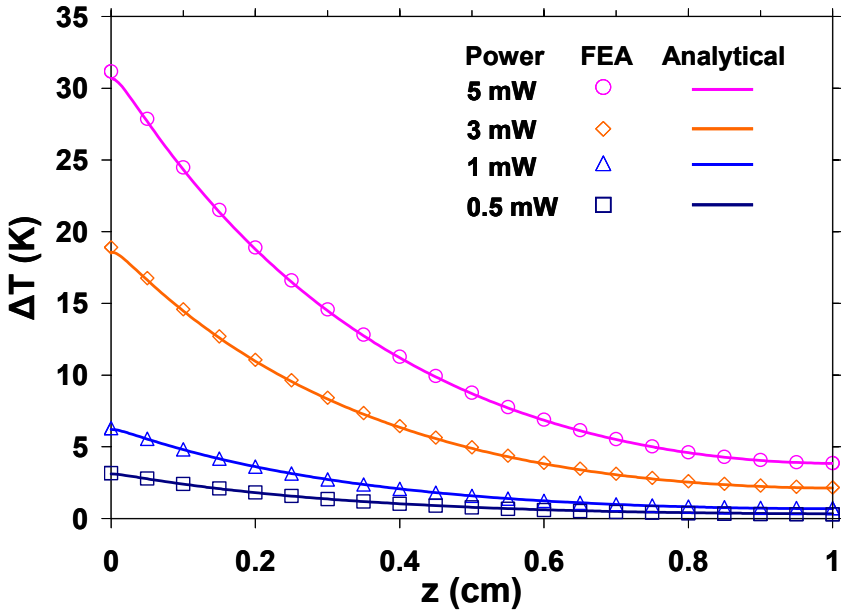

(a)

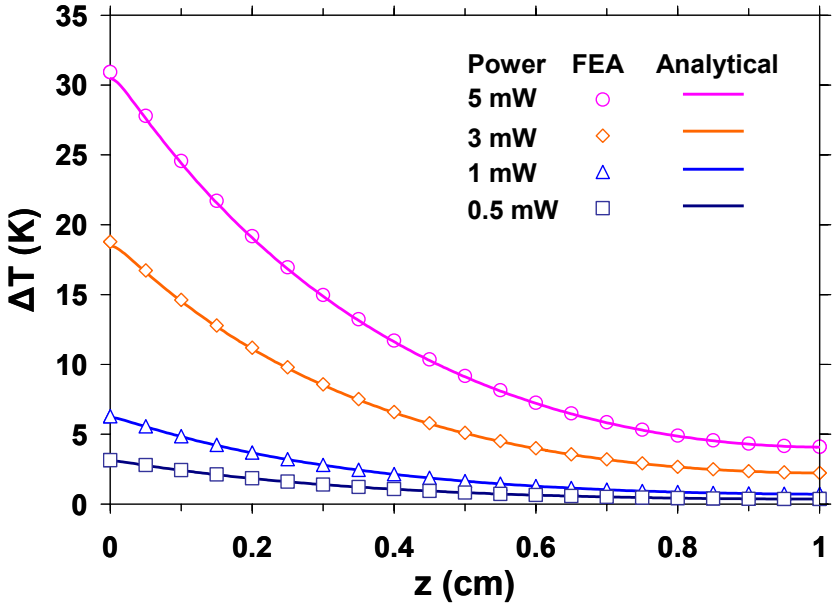

(b)

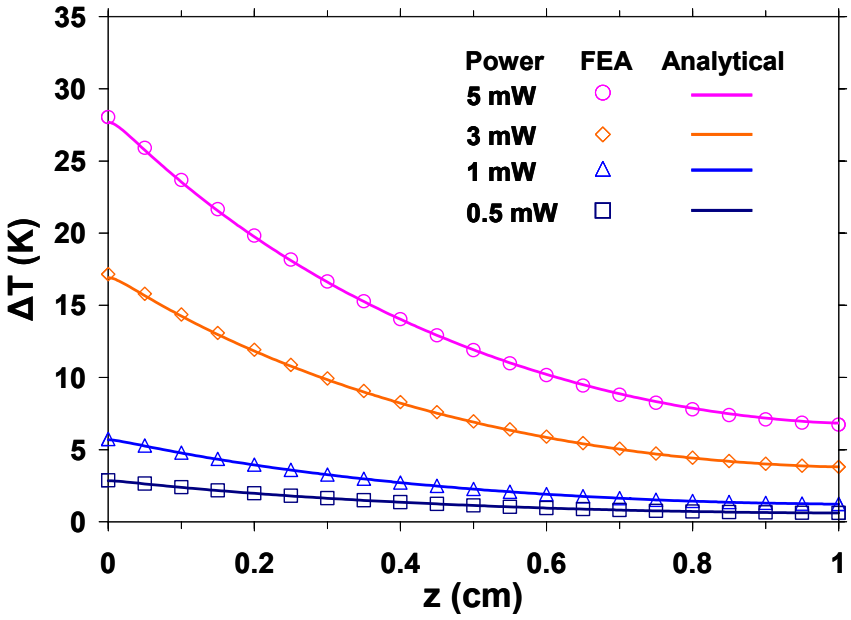

(c)

Figure 7.6: Analytical and numerical excess temperatures along a PMMA Fiber Bragg Grating illuminated by single mode laser diodes with spectral bandwidths of (a) 0.001 nm (b) 0.026 nm (c) 0.1 nm at ambient of 25°C

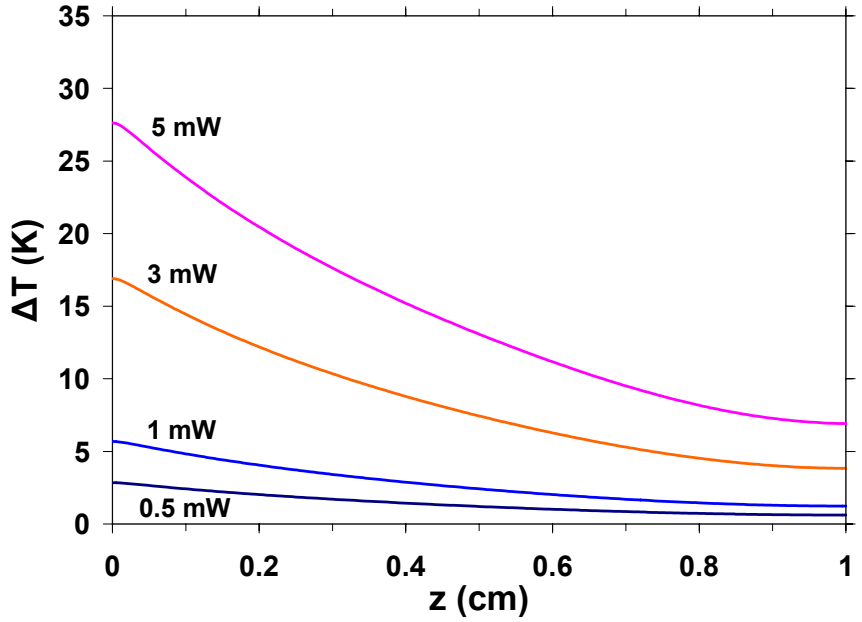

Figure 7.7: Analytical excess temperatures along a PMMA Fiber Bragg Grating illuminated by a single mode laser diode with a spectral bandwidth of 0.1 nm at ambient of 25°C. The solution was obtained using heat generations associated with the purely closed-form coupled-mode solutions (Eqs. 4.24 and 4.25).

.

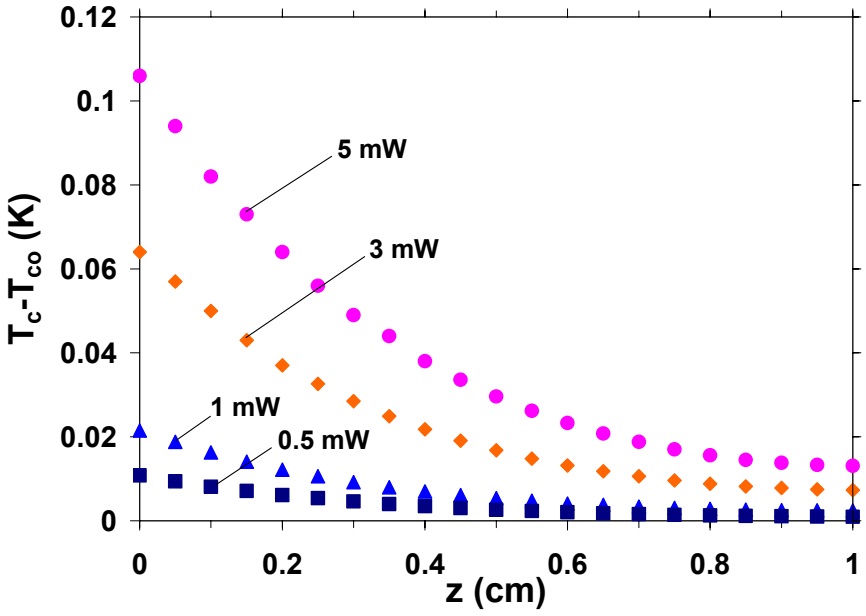

(a)

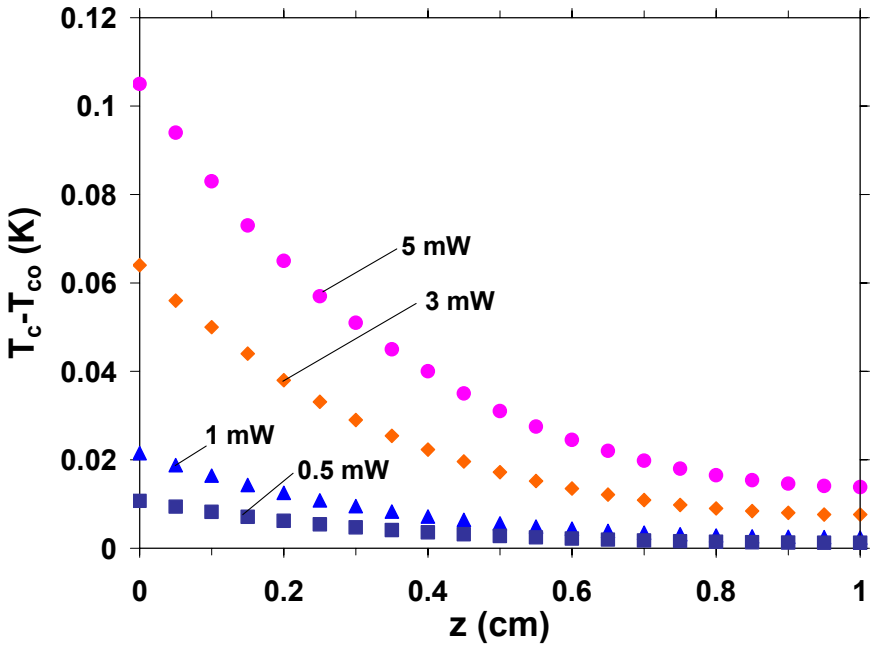

(b)

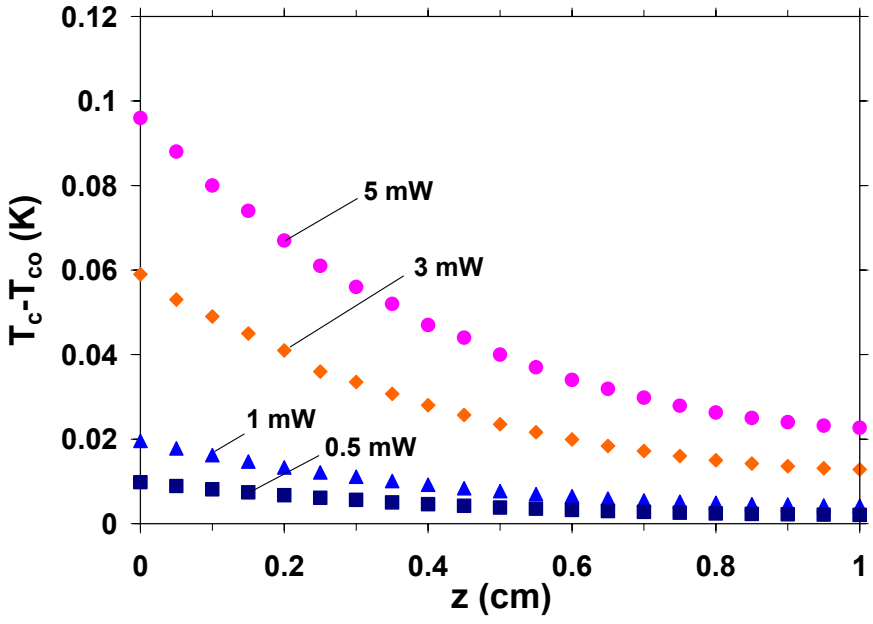

(c)

Figure 7.8: Radial temperature differences along a PMMA Fiber Bragg Grating illuminated by single mode laser diodes with spectral bandwidths of (a) 0.001 nm (b) 0.026 nm (c) 0.1 nm at ambient of 25°C.

The results obtained from the finite-element simulation are also shown in Figure 7.6. They agree very well with the analytical results, typically within 1% accuracy. Figures 7.6(c) and 7.7 show that the two solutions, associated with the modified and purely closed-form coupled-mode solutions, predict very similar temperature distributions with an average discrepancy of 5%. It should be noted again that all thermal solutions; spectral heat generation densities, axial heat generation densities, temperatures in the PFBG; associated with the modified closed-form coupled mode solutions are very similar to those with the purely closed-form coupled mode solutions.

Figure 7.8 shows another FEA results of the radial temperature differences between the center of the PFBG core (T_c) and the core surface temperature (T_{co}) along the PMMA FBG. The maximum radial temperature difference lies below 0.11 K at the inlet of the grating and decreases axially to below 0.03 K for the highest light intensity of 5 mW, with similar profiles and even lower radial temperature differences for the lower illumination powers. Thus, the FEA results validate the one-dimensional heat conduction assumption used in the analytical thermal model for the SMLD illuminations.

7.3 Thermo-Optical Analysis

7.3.1 Reflectivity spectra

The reflectivity spectra of the PMMA FBG associated with the SMLD illuminations were obtained by the fully coupled thermo-optical analysis. A total of 200 segments (Δz = 50 μm), with a wavelength band of 0.1 pm for SMLD I and 0.5 pm for SMLD II and III, was used for the numerical analysis.

Figure 7.9 displays the thermally-induced changes in the spectral reflectivities of the PMMA FBG, illuminated by 5 mW of SMLD lights, in an ambient temperature of 25°C. The results for SMLD III in Figure 7.9(c) are associated with the modified closed-form coupled-mode solutions. The individual effects of the index change with temperature, (dn/dT), and the grating period change with temperature, $(d\Lambda/dT)$, were determined.

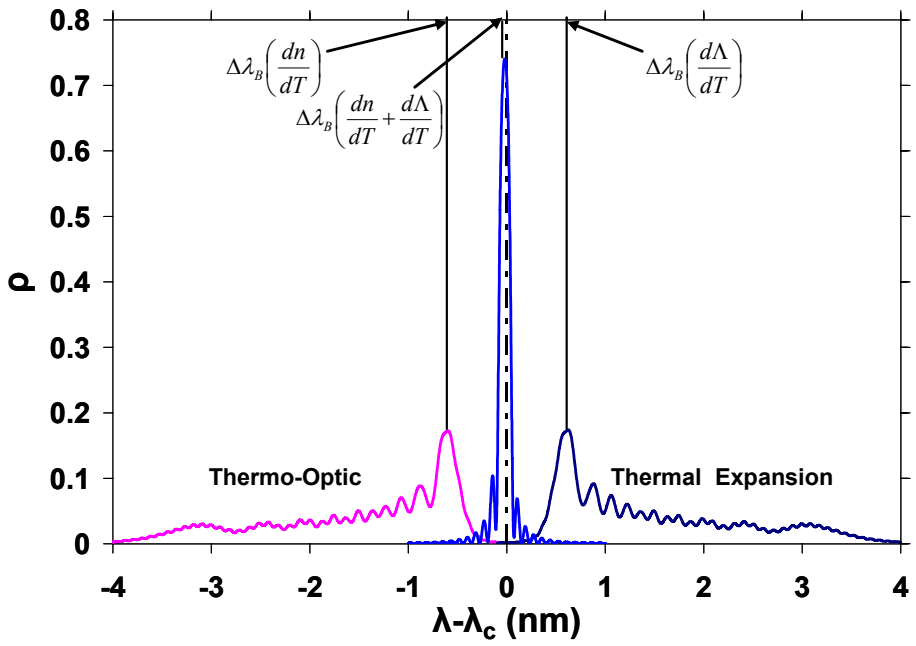

(a)

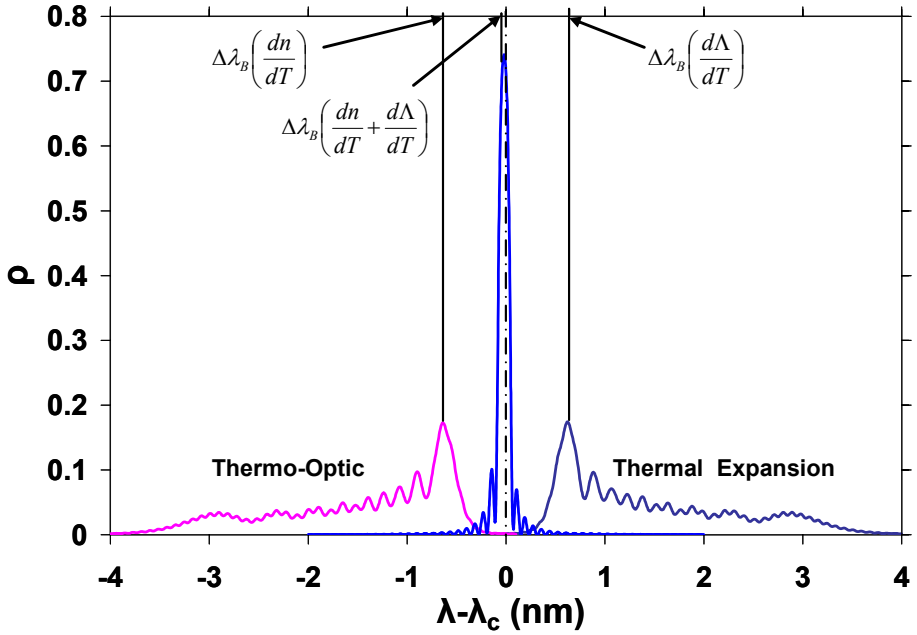

(b)

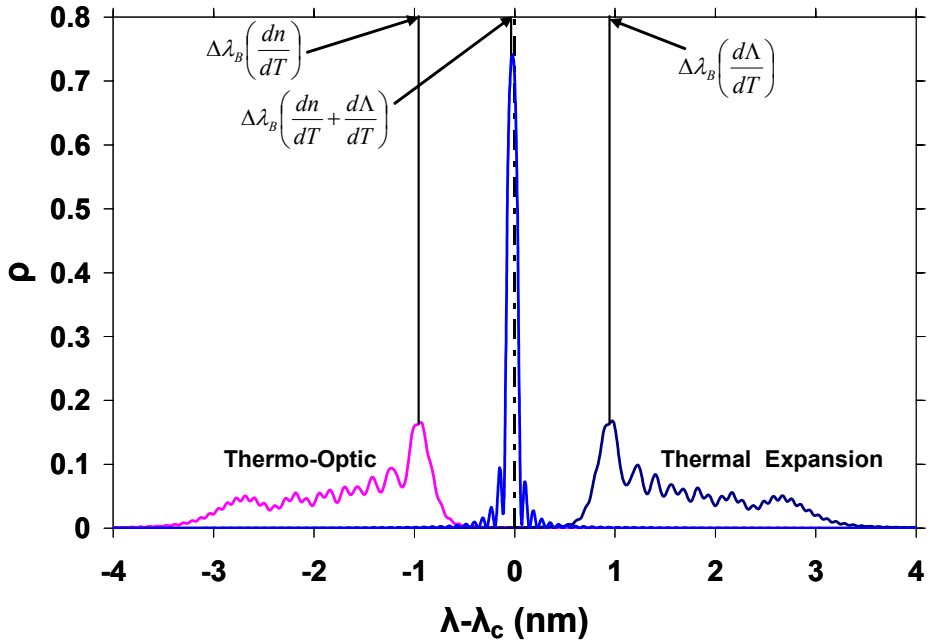

(c)

Figure 7.9: Thermally-induced Bragg wavelength shifts in a PMMA Fiber Bragg Grating illuminated with single mode laser diodes – thermo-optic (dn/dT), thermal expansion ($d\Lambda/dT$), and combined effects ($dn/dT + d\Lambda/dT$) associated with (a) 0.001nm, (b) 0.026 nm, and (c) 0.1nm of bandwidths of SMLDs at 5 mW of incident optical power with 25°C of ambient

The results show that the thermally-driven index change and the grating pitch change induced by thermal expansion produce a negative and a positive shift, respectively, relative to the incident 1576.5 nm-centered SMLD light. Due to the thermally-driven index changes, the dominant "Bragg" wavelengths move lower by 0.6 nm, 0.64 nm, and 0.94 nm for SMLD I, II and III, respectively. Grating period changes drive the dominant "Bragg" wavelengths higher by 0.62 nm, 0.62 nm, and 0.97 nm for SMLD I, II and III, respectively. The combined reflectivity spectrums present tiny shifts in Bragg wavelengths, i.e. -0.019 nm, -0.02 nm, and -0.024 nm for for SMLD I, II and III, respectively. The spectral compensation, noted previously in Chapter 6, of the two individual effects, is in clear evidence in this reflectivity spectrums. The jagged characters of the reflectivity spectrums are associated with the spectral dispersions induced by the axially non-uniform temperatures along the FBG. It should be noted that the wider dispersion of the spectrum occurs with the narrower light source which produces a higher temperature gradient.

Figure 7.10 presents the total reflectivity spectrums for the maximum (5 mW) and minimum (0.5 mW) incident SMLD powers, as well as the no absorption case. It may again be noted that the results for the 0.1nm SMLD III, displayed in Figure 7.10(c), reflect a greater contribution of the "weak interaction zone" and the modified closed-form coupled-mode solutions than the other two SMLD's considered in this study. The Bragg wavelength shifts, $\Delta\lambda_B$, based on the wavelengths at the peak reflectivities can be determined from Figure 7.10. Figures 7.10 (c) and Figure 7.11 provide a clear evidence that two solutions, associated with the modified and purely closed-form coupled-mode solutions, predict very similar reflectivity spectra with a typical discrepancy of 1 %. This

result in the similar prediction of the Bragg wavelength shifts with discrepancies which is typically less than 1 pm.

Table 7.1 provides additional $\Delta\lambda_B$ values and compares them with the values predicted by the linear (Eq. 3.1) and the quadratic (Eq. 4.45) relation with the average temperature. They show reasonably good agreement when the ambient is 25°C, but the linear model produces significant errors at the higher ambient temperatures.

It is to be noted that at the ambient temperature of 25°C, the SMLD illuminations result in nearly 40 % smaller Bragg wavelength shifts compared to those produced by the LED light source. This reduction in $\Delta\lambda_B$ can be explained by the approximately 40 % lower average temperature rise for the PMMA grating illuminated by the SMLDs. As the ambient temperature increases, the difference in the average temperature rise becomes smaller and the values of $\Delta\lambda_B$ for the SMLD become similar of those of the LED light source.

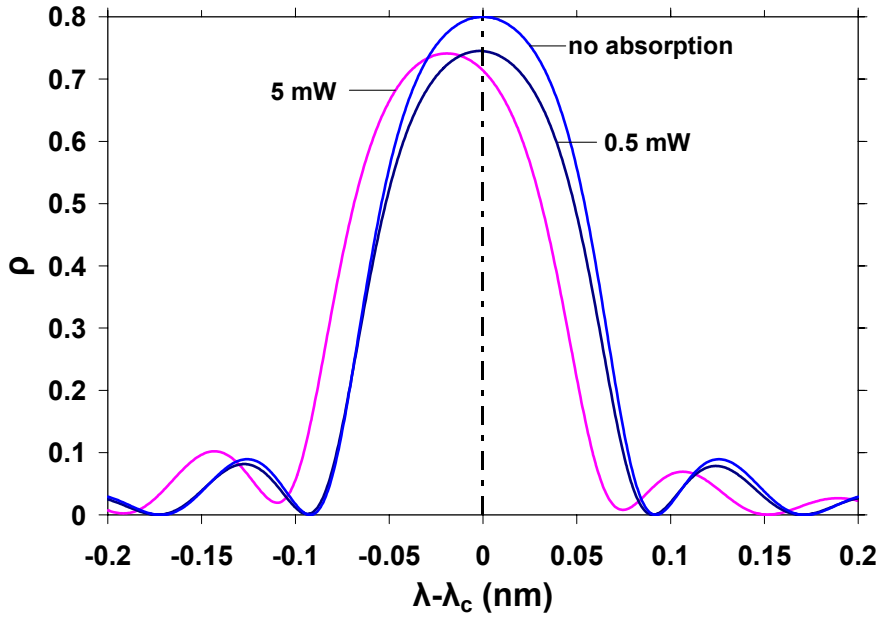
0.8
0.7
0.6
0.5
0.4
0.3
0.2
0.1
0
ρ
-0.2
-0.15
-0.1
-0.05
0
0.05
0.1
0.15
0.2
λ-λc (nm)
no absorption
5 mW
0.5 mW

(a)

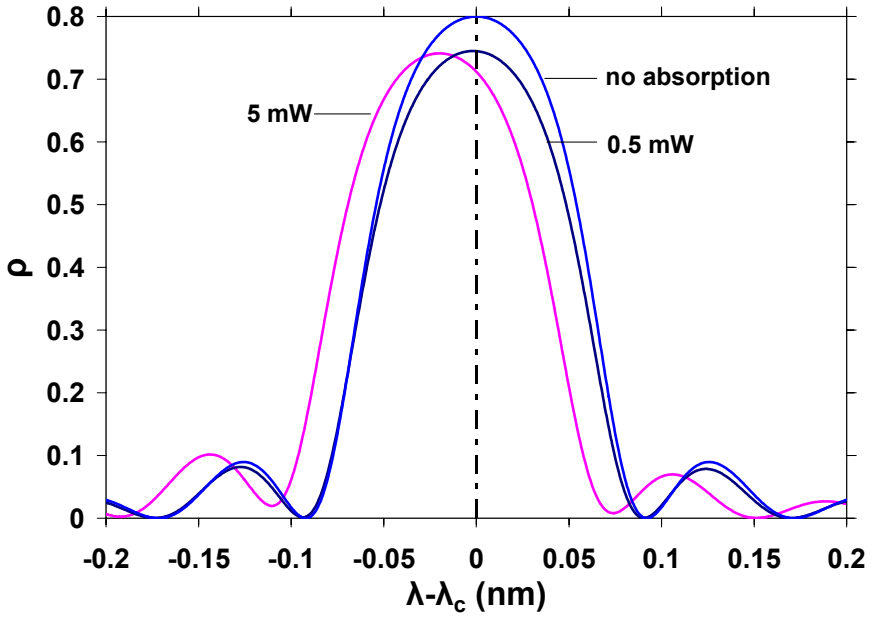
0.8
0.7
0.6
0.5
0.4
0.3
0.2
0.1
0
ρ
-0.2
-0.15
-0.1
-0.05
0
0.05
0.1
0.15
0.2
λ-λc (nm)
no absorption
5 mW
0.5 mW

(b)

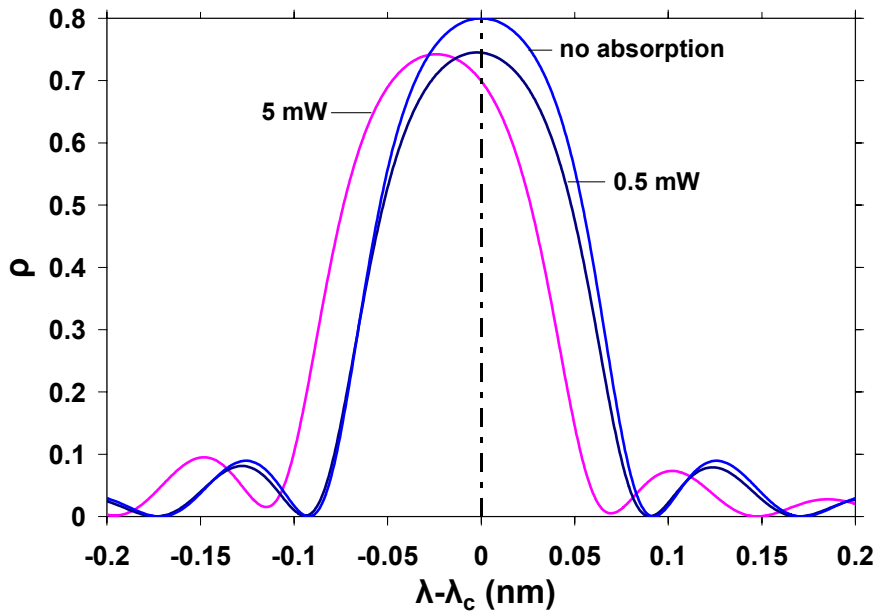

(c)

Figure 7.10: Narrow-band reflectivity spectra for a PMMA Fiber Bragg Grating illuminated by single mode laser diodes with spectral bandwidths of (a) 0.001 nm (b) 0.026 nm (c) 0.1 nm at ambient of 25°C

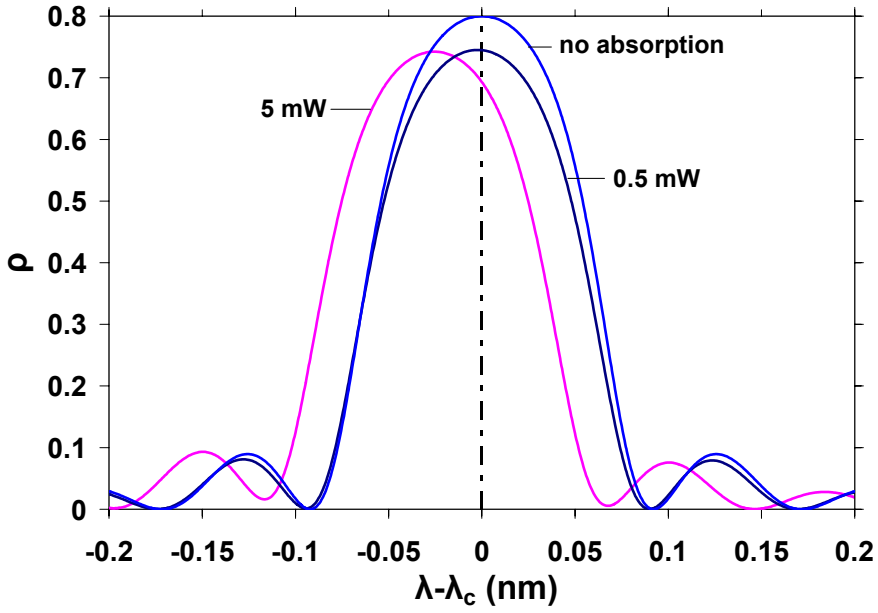

Figure 7.11: Narrow-band reflectivity spectrum for a PMMA Fiber Bragg Grating illuminated by a single mode laser diode with the spectral bandwidth of 0.1 nm at ambient of 25°C. The solution was obtained using temperatures associated with the purely closed-form coupled-mode solutions (Eqs. 4.24 and 4.25).

Table 7.1: Bragg wavelength shifts in a PMMA Fiber Bragg Grating with single mode laser diode illuminations with spectral bandwidths of (a) 0.001 nm (b) 0.026 nm (c) 0.1 nm

(a) Associated with bandwidth of 0.001 nm

Ambient temperature T_{amb}	Incident optical power $P_{inc}\ (mW)$	Average excess temperature $\overline{\Delta T}\ (K)$	Transfer Matrix Method (pm)	Quadratic -Eq. 4.45 (pm)	Linear -Eq. 3.1 (pm)
25	0.5	1.1	-1.7	-1.8	-1.8
25	1	2.2	-3.4	-3.7	-3.7
25	3	6.7	-10.8	-11.6	-11.2
25	5	11.57	-19.3	-20.5	-19.3
35	0.5	11.16	-19.6	-19.7	-18.6
35	1	12.34	-21.6	-21.9	-20.6
35	3	17.58	-31.4	-32.0	-29.3
35	5	24.5	-47	-47.1	-41.7
45	0.5	21.37	-39.5	-39.6	-35.7
45	1	22.84	-42.5	-42.6	-38.1
45	3	30.37	-58.9	-58.6	-50.7
45	5	37.11	-73.9	-73.7	-62.0

(b) Associated with bandwidth of 0.026 nm

Ambient temperature T_{amb}	Incident optical power $P_{inc}\ (mW)$	Average excess temperature, $\overline{\Delta T}\ (K)$	Transfer Matrix Method (pm)	Quadratic -Eq. 4.45 (pm)	Linear -Eq. 3.1 (pm)
25	0.5	1.12	-1.5	-1.9	-1.9
25	1	2.24	-3.5	-3.8	-3.7
25	3	6.83	-11	-11.8	-11.4
25	5	11.85	-20	-21	-19.8
35	0.5	11.18	-19.5	-19.7	-18.7
35	1	12.39	-21.5	-22	-20.7
35	3	17.79	-32	-32.4	-29.7
35	5	25.04	-47	-47.2	-41.8
45	0.5	21.4	-39.5	-39.6	-35.7
45	1	22.88	-42.5	-42.7	-38.2

45	3	29.8	-57.5	-57.3	-49.8
45	5	37.08	-74	-73.6	-61.9

(c) Associated with bandwidth of 0.1 nm

Ambient temperature T_{amb}	Incident optical power $P_{inc}\ (mW)$	Average excess temperature $\overline{\Delta T}\ (K)$	Transfer Matrix Method (pm)	Quadratic -Eq. 4.45 (pm)	Linear -Eq. 3.1 (pm)
25	0.5	1.33	-2	-2.2	-2.2
25	1	2.67	-4.5	-4.5	-4.5
25	3	8.07	-13.5	-14.0	-13.5
25	5	13.72	-24	-24.5	-22.9
35	0.5	11.36	-20	-20.1	-19.0
35	1	12.73	-22.5	-22.6	-21.3
35	3	18.44	-33.5	-33.7	-30.8
35	5	24.62	-46	-46.3	-41.1
45	0.5	21.43	-39.5	-39.7	-35.8
45	1	22.89	-42.5	-42.7	-38.2
45	3	29.04	-55.5	-55.7	-48.5
45	5	35.73	-70.5	-70.6	-59.7

7.3.2 Reflected power spectra

The reflectivity of a FBG is defined as the ratio of the reflected optical power to the incident optical power at the inlet of the FBG (at z = 0). To obtain this reflectivity, it is again necessary to perform a convolution of the incident spectrum with the calculated spectral reflectivity, which yields the reflected power spectrums and then integrate this over the bandwidth of the light source to obtain the total reflected power and the grating reflectivity. This procedure was followed using Eqs. (4.52) and (4.53).

The results for SMLD III in Figure 7.12(c) are most reflective of the contribution of the weak interactions encountered for large detuning values and incorporated into the modified closed-form coupled-mode solutions. The results disclose that the wider spectral illumination produces more asymmetric spectra of the reflected powers. From Figure 7.12, the shifts of wavelengths at maximum reflected powers (will be referred to as *reflected power based Bragg wavelength shift*; $\Delta\lambda_B^P$) can be determined. Figures 7.12 (c) and 7.13 demonstrate that two solutions (the modified and purely closed-form coupled-mode solutions) predict very similar reflected power spectra with a typical discrepancy of 1%. Consequently, the similar prediction of the $\Delta\lambda_B^P$ follows with discrepancies which are typically less than 0.5 pm. It should be noted that the similar thermo-optical solutions associated with two coupled-mode solutions result from the obtained similar thermal solutions. The values of $\Delta\lambda_B^P$ are compared with those based on the peak reflectivity (will be referred to *reflectivity based Bragg wavelength shift*; $\Delta\lambda_B^R$) in Tables 7.2.

Figure 7.14 illustrates graphically the difference between $\Delta\lambda_B^P$ (the wavelength at the maximum reflected power measured by an optical spectrum analyzer) and $\Delta\lambda_B^R$ (the wavelength at the maximum reflectivity) for the case of an incident power of 3 mW and an ambient temperature of 35°C. The maximum reflected power occurs at $\lambda - \lambda_c = -1$ pm while the maximum reflectivity is found at $\lambda - \lambda_c = -32$ pm.

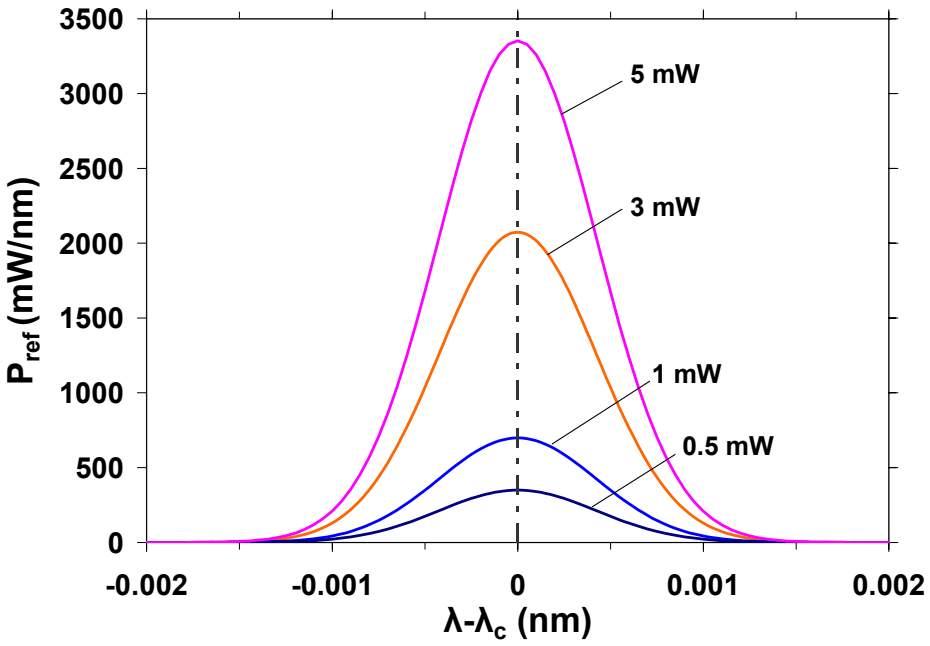

(a)

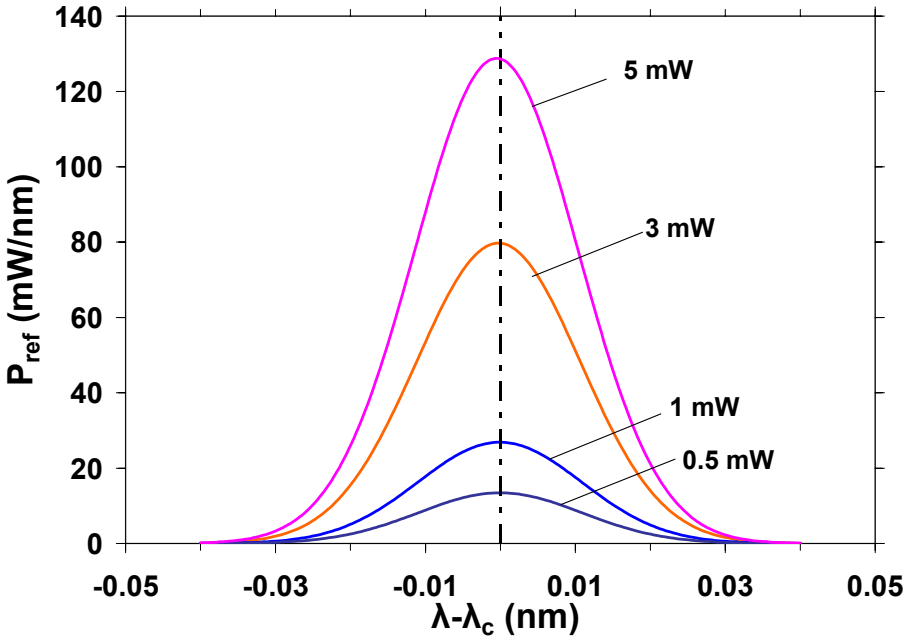

(b)

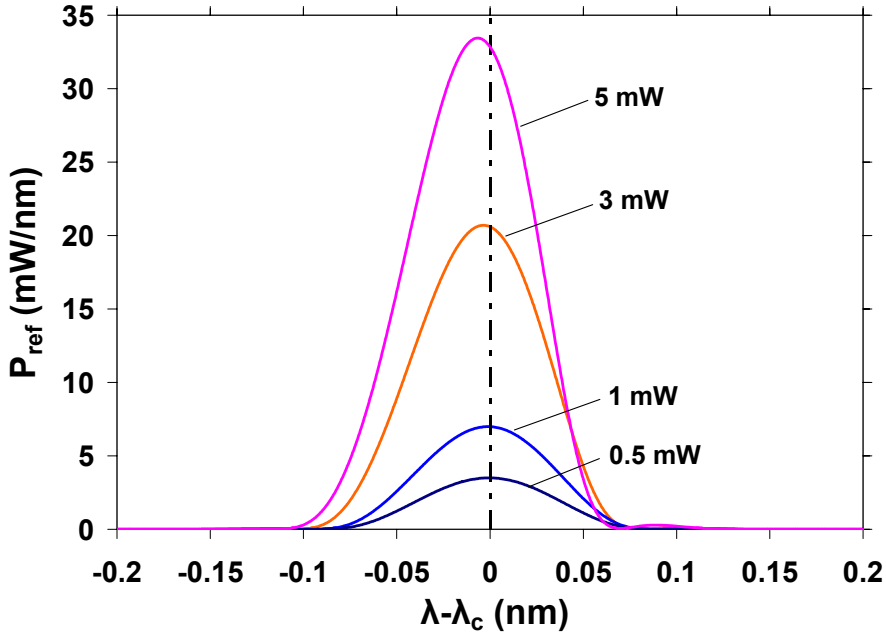

(c)

Figure 7.12: Reflected power spectra of a PMMA Fiber Bragg Grating illuminated by single mode laser diode illuminations with spectral bandwidths of (a) 0.001 nm (b) 0.026 nm (c) 0.1 nm at ambient of 25°C.

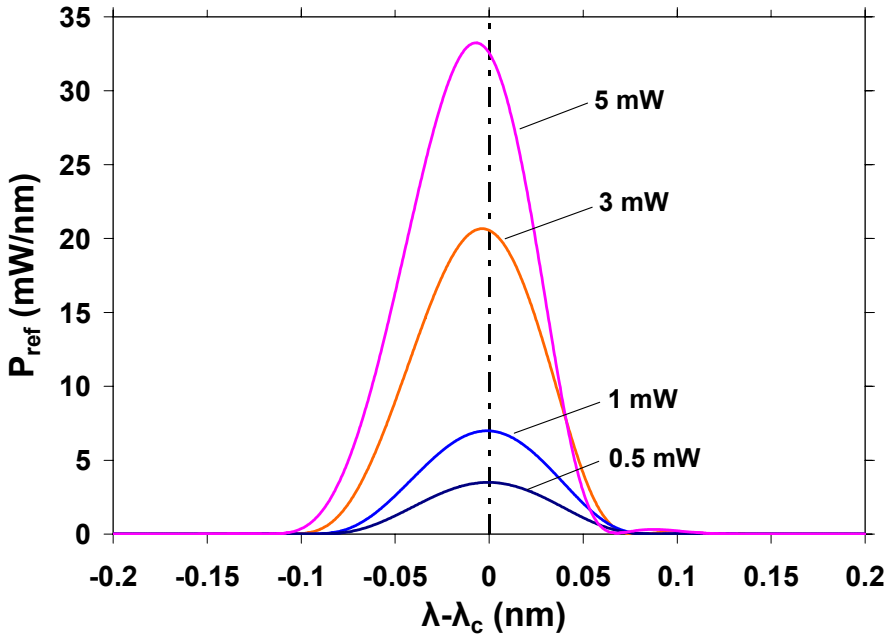

Figure 7.13: Reflected power spectrum of a PMMA Fiber Bragg Grating illuminated by a single mode laser diode illumination with a spectral bandwidth of 0.1 nm at ambient of 25°C. The solution was obtained using temperatures associated with the purely closed-form coupled-mode solutions (Eqs. 4.24 and 4.25).

In general the values of $\Delta\lambda_B^P$ are much smaller than those of $\Delta\lambda_B^R$. It is important to note that the values of $\Delta\lambda_B^P$ for SMLD I become virtually zero as shown in Table 7.2. It should be noted that these zero values are numerically calculated associated with 0.1 pm of the wavelength band for TMM; this zero values mean that $\Delta\lambda_B^P$ is smaller than 0.1pm. For SMLD I, the incident power sharply decreases for wavelengths outside the FWHM band of the incident light so that the maximum reflected power can only occur near the center of the grating bandwidth.

The data in Table 7.1 are plotted in Figure 7.15, which presents the Bragg wavelength shifts ($\Delta\lambda_B^R$) for different ambient temperatures. The results reveal the significant effect of ambient temperature rise on the Bragg wavelength shift; an ambient

temperature rise of approximately 10 K produces the value of $\Delta\lambda_B^R$ almost as large as the value of $\Delta\lambda_B^R$ produced by a factor of 10 increase in the incident optical power.

Figure 7.15 also contains the results obtained from the quadratic analytical solution based on the average temperature. In spite of its relative simplicity, the equation predicts the value of $\Delta\lambda_B^R$ faithfully; the maximum discrepancy is less than 1 pm.

The data in Table 7.2 are plotted in Figure 7.16. It clearly demonstrates that the considerable discrepancies between the values of $\Delta\lambda_B^P$ and $\Delta\lambda_B^R$. As discussed before, this was caused by the sharp spectral dependence on the power density.

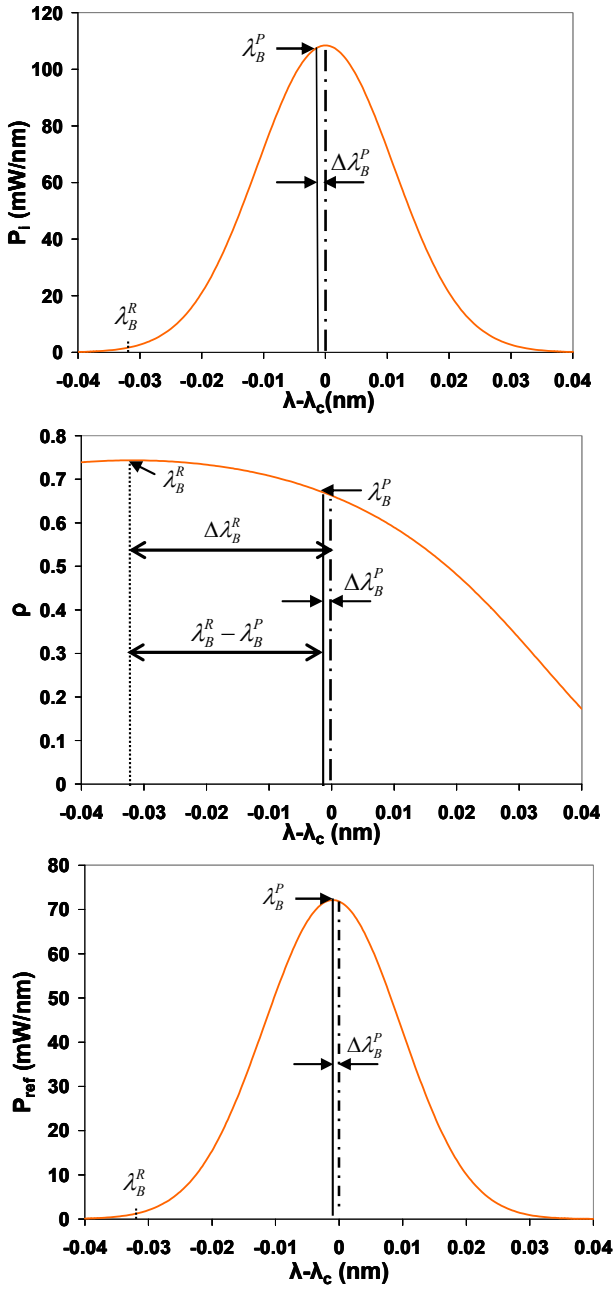

Figure 7.14: Reflected power based and reflectivity based Bragg wavelength shifts in a PMMA Fiber Bragg Grating illuminated with a 3mW single mode laser diode at ambient of 35°C

Table 7.2: Reflectivity based and reflected power based Bragg wavelength shifts in a PMMA Fiber Bragg Grating illuminated with single mode laser diodes with spectral bandwidth of (a) 0.001 nm (b) 0.026 nm (c) 0.1 nm
(a) Associated with bandwidth of 0.001 nm

Ambient temperature T_{amb}	Incident optical power $P_{inc}\ (mW)$	Average excess temperature $\overline{\Delta T}\ (K)$	Reflectivity based Bragg wavelength shift by Transfer Matrix Method (pm)	Reflected power based Bragg wavelength shift by Transfer Matrix Method (pm)
25	0.5	1.1	-1.7	0
25	1	2.2	-3.4	0
25	3	6.7	-10.8	0
25	5	11.57	-19.3	0
35	0.5	11.16	-19.6	0
35	1	12.34	-21.6	0
35	3	17.58	-31.4	0
35	5	24.5	-47	0
45	0.5	21.37	-39.5	0
45	1	22.84	-42.5	0
45	3	30.37	-58.9	0
45	5	37.11	-73.9	0

(b) Associated with bandwidth of 0.026 nm

Ambient temperature, T_{amb}	Incident optical power $P_{inc}\ (mW)$	Average excess temperature $\overline{\Delta T}\ (K)$	Reflectivity based Bragg wavelength shift by Transfer Matrix Method (pm)	Reflected power based Bragg wavelength shift by Transfer Matrix Method (pm)
25	0.5	1.12	-1.5	0
25	1	2.24	-3.5	0
25	3	6.83	-11	-0.5
25	5	11.85	-20	-0.5
35	0.5	11.18	-19.5	-0.5
35	1	12.39	-21.5	-0.5
35	3	17.79	-32	-1
35	5	25.04	-47	-2
45	0.5	21.4	-39.5	-1.5
45	1	22.88	-42.5	-2

45	3	29.8	-57.5	-3.5
45	5	37.08	-74	-7.5

(c) Associated with bandwidth of 0.1 nm

Ambient temperature T_{amb}	Incident optical power $P_{inc}\ (mW)$	Average excess temperature $\overline{\Delta T}\ (K)$	Reflectivity based Bragg wavelength shift by Transfer Matrix Method (pm)	Reflected power based Bragg wavelength shift by Transfer Matrix Method (pm)
25	0.5	1.33	-2	-0.5
25	1	2.67	-4.5	-1
25	3	8.07	-13.5	-3.5
25	5	13.72	-24	-6.5
35	0.5	11.36	-20	-5.5
35	1	12.73	-22.5	-6
35	3	18.44	-33.5	-10
35	5	24.62	-46	-15
45	0.5	21.43	-39.5	-12.5
45	1	22.89	-42.5	-13.5
45	3	29.04	-55.5	-19.5
45	5	35.73	-70.5	-28

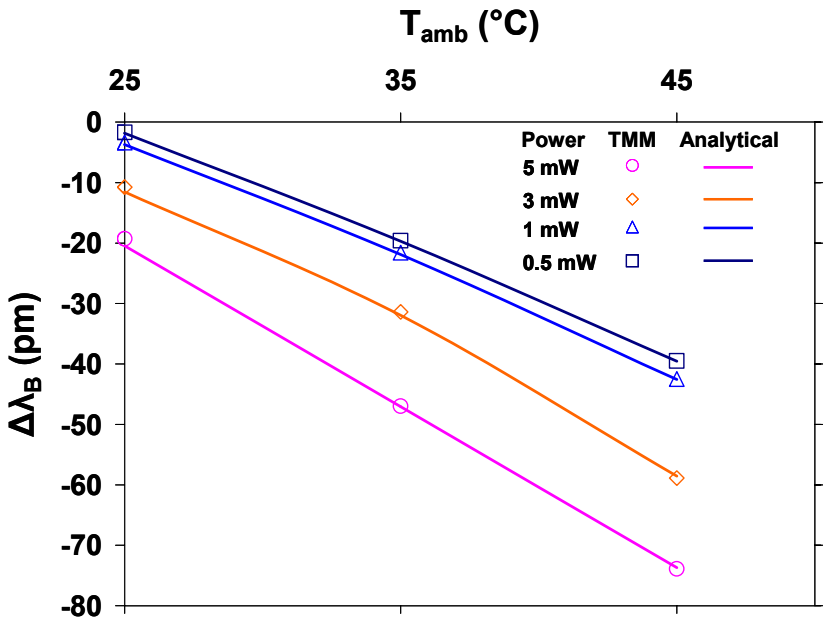
T_amb (°C)
25
35
45
0
-10
-20
-30
-40
-50
-60
-70
-80
Δλ_B (pm)
Power
TMM
Analytical
5 mW
3 mW
1 mW
0.5 mW

(a)

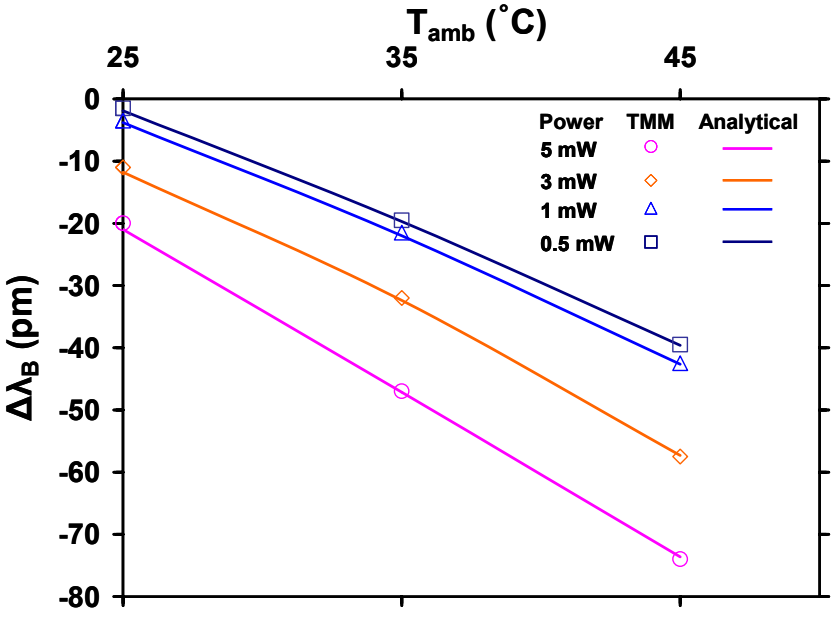
T_amb (˚C)
25
35
45
0
-10
-20
-30
-40
-50
-60
-70
-80
Δλ_B (pm)
Power
TMM
Analytical
5 mW
3 mW
1 mW
0.5 mW

(b)

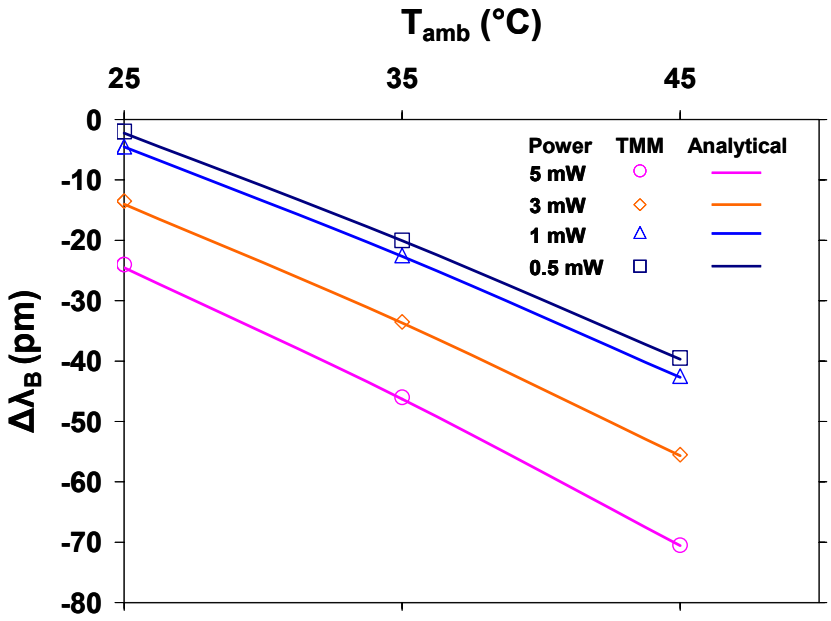

(c)

Figure 7.15: Bragg wavelength shifts in a PMMA Fiber Bragg Grating with single mode laser diode illuminations with spectral bandwidths of (a) 0.001 nm (b) 0.026 nm (c) 0.1 nm for ambient temperatures of 25°C to 45°C

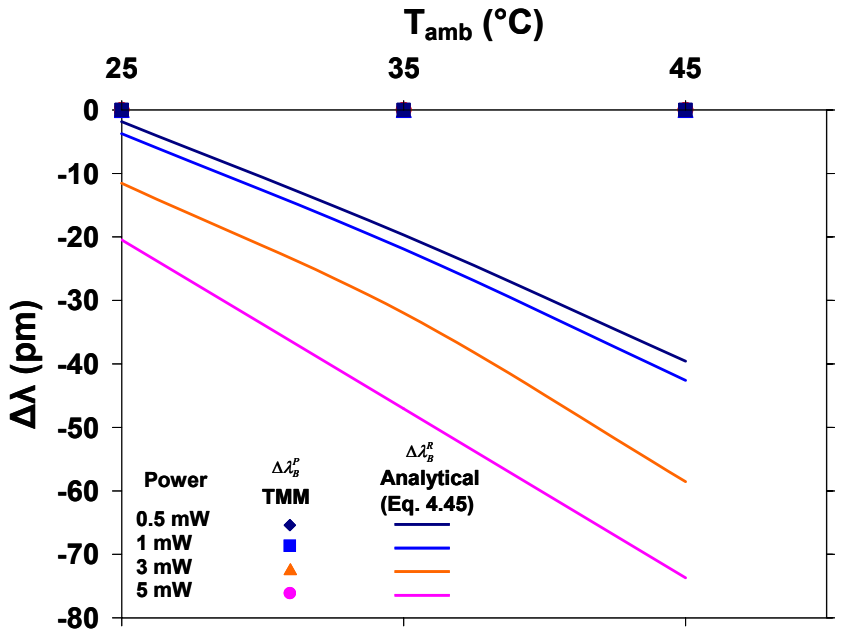
T_amb (°C)
25
35
45
0
-10
-20
-30
-40
-50
-60
-70
-80
Δλ (pm)
Power
0.5 mW
1 mW
3 mW
5 mW
Δλ_B^P
TMM
Δλ_B^R
Analytical
(Eq. 4.45)

(a)

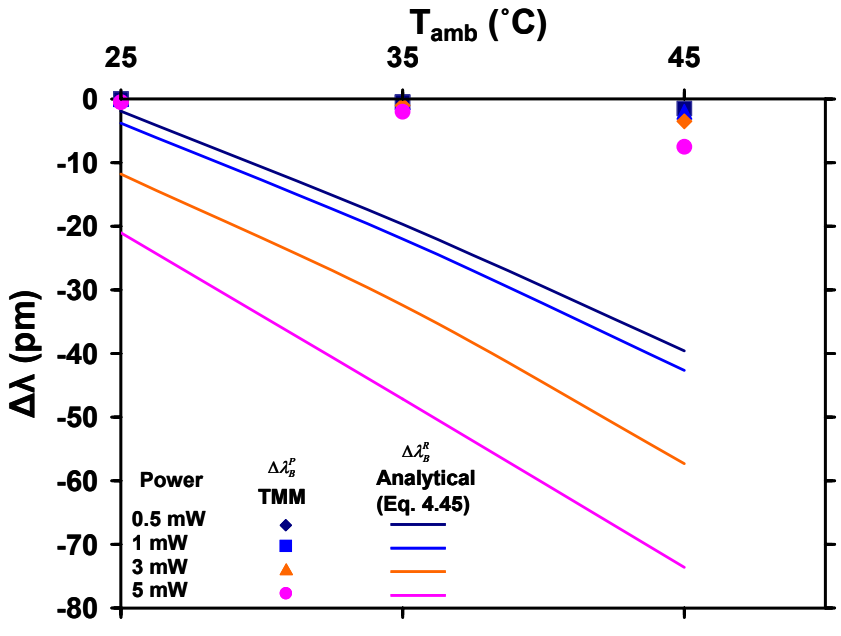
T_amb (°C)
25
35
45
0
-10
-20
-30
-40
-50
-60
-70
-80
Δλ (pm)
Power
0.5 mW
1 mW
3 mW
5 mW
Δλ_B^P
TMM
Δλ_B^R
Analytical
(Eq. 4.45)

(b)

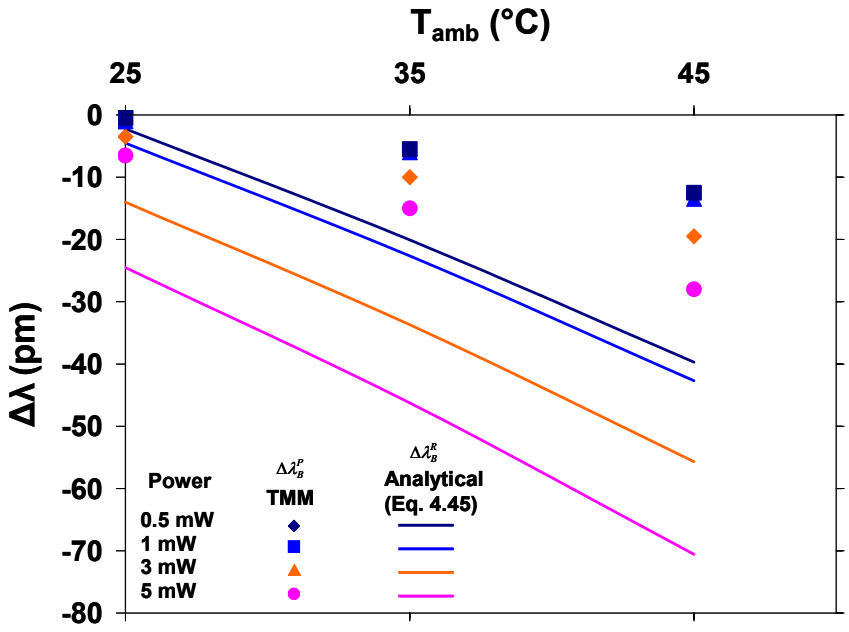

(c)

Figure 7.16: Reflectivity based and reflected power based Bragg wavelength shifts induced by single mode laser diode illuminations with spectral bandwidths of (a) 0.001 nm (b) 0.026 nm (c) 0.1 nm for ambient temperatures of 25°C to 45°C

Chapter 8

Conclusion

8.1 Summary

To facilitate the selection of polymeric optical materials and the rational design of polymer Bragg Gratings (BGs), this thesis seeks to provide a complete understanding of the thermo-optic behavior of polymer BGs. First order thermo-optical model of a self-heated polymer BG and the detailed thermo-optical model of a self-heated Polymer Fiber Bragg Grating (PFBG) were generated. The model for the PFBG was experimentally verified. The model was applied to predict the thermo-optical behavior of a self-heated PMMA FBG associated with a LED and a SMLD illumination. The conclusions of each chapter will be provided separately as follows.

Chapter 1:

- General backgrounds of polymer BGs and motives for the study were provided.

Chapter 2:

- Physical descriptions and basic optical principles of BGs were presented.

Chapter 3:

- 1st order thermo-optical model of a polymer BG was developed and applied to characterize a self-heated PMMA Bragg grating waveguide.
- It was found that Bragg wavelength shifts created by two coupled-effects; the thermally-induced index shift and the grating pitch change, the stress-induced index shift and the grating pitch change; should be considered to precisely predict the net Bragg wavelength shifts of a polymer BG.

- It was found that the PMMA substrate shows a reduced Bragg wavelength shift compared to the silicon substrate.
- The reduced shift can be explained by the compensation induced by the Bragg wavelength shift, caused by the thermally-driven index shift, with a comparable magnitude and a opposite sign to that induced by the grating pitch change.

Chapter 4:

- The methodology for a detailed thermo-optical modeling of a self-heated PFBG was developed.
- Three specific zones of Bragg grating behavior were identified.
- Heat generations in the BG were formulated for the PFBG associated with the illuminations of narrow and wide band lights.
- A fully-coupled thermo-optical model of a PFBG illuminated by a narrow band light was generated.

Chapter 5:

- An experiment was conducted to verify the validity of the thermo-optical modeling of the PFBG.
- It was found that the predicted Bragg wavelength shifts by the numerical thermo-optical model show less than 10% of discrepancy to the measured values.
- The predicted spectrums showed reasonably good agreements with the measured spectrums despite some discrepancies in the higher orders of reflection.
- The small discrepancy demonstrates the proposed thermo-optical model predicts Bragg wavelength shifts well.

Chapter 6:

- The verified thermo-optical model was applied to characterize the thermo-optical behavior of a self-heated PMMA FBG illuminated by a LED.
- Use of the derived model revealed that light absorption in a PMMA FBG, associated with a 0.5 mW to 5 mW LED illumination, resulted in up to 400W/cm^3 of in-fiber heating and a consequent rise in the temperature of a passively-cooled PFBG approaching 18 K.
- It was found that at 5mW of the LED illumination, the dominant "Bragg" wavelength moves lower by -2.03 nm due to the index change, while the change of the grating period results in a positive shift of 2.0 nm, and consequently the combined reflectivity spectrum shows a very small total shift in Bragg wavelength (-0.03 nm) with modest spectral dispersion.
- The resulting changes in the effective refractive index and the Bragg grating pitch were found to be significant in magnitude but opposite in sign, thus leading to very modest net changes in the Bragg wavelength.
- An analytical thermo-optical model was found to yield Bragg wavelength shifts that are nearly indistinguishable from the more rigorous numerical solution.

Chapter 7:

- The thermo-optical model was applied to characterize the thermo-optical behavior of a self-heated PMMA FBG illuminated by SMLDs.
- The results revealed that the inlet of the SMLD illuminated PMMA FBG experiences significant heating, reaching excess temperatures of 31 K to 28 K at 5

mW and 7 K to 3 K even at just 0.5 mW of incident power, and they are significantly higher than the peak temperatures induced by the LED illumination.

- It was found that the reflectivity spectra present tiny shifts in Bragg wavelengths, i.e. -0.019 nm, -0.02 nm, and -0.024 nm for SMLD I, II and III, respectively.
- The TMM simulation has identified a Bragg shift anomaly for narrow-band illuminations, with the reflectivity based shift far larger than the reflected power-based shift in the PMMA grating.
- The tiny shifts in wavelengths of the PMMA FBG associated with SMLD illuminations are due to the spectral compensation in two individual effects.
- The Bragg shift anomaly can be explained by the strong spectral dependence of the incident optical power.

8.2 Future Work

The fully integrated thermo-optical model for a self-heated PFBG was firstly generated in this study. The generated thermo-optical model was carefully verified conducting the thermo-optical experiment. The developed model was utilized to investigate thermo-optical behavior of the passively-cooled PMMA PFBG illuminated by light sources. However, there are still many questions left for the complete understanding of thermo-optical characteristics of polymer Bragg gratings. Hence, topics and questions for the future investigations are suggested as follows.

8.2.1 Polymer fiber Bragg grating

- More rigorous experimental studies utilizing a PFBG would be needed to support the model-predicted significantly variant temperatures along a PFBG associated with a narrow band illumination.
- The effect of the radial temperature gradient on the effective index of the PFBG can be investigated to strengthen the thermo-optical model for the PFBG.
- The thermal dependence of the index modulation might be studied to provide the better understanding of the effect of the thermally-driven coupling coefficient change on the optical behavior of the PFBG.
- Inter-relationships among penetration depths, local coupling coefficients, local Bragg resonances, and the axial temperature gradients in a non-isothermal PFBG can be studied to develop a more sophisticated thermo-optical model.
- The thermo-optical behavior of the PFBG associated with other temperature gradients and stress, which can be generated by environmental effects would be investigated.

8.2.2 Polymer planar Bragg grating

- Thermo-optical behaviors of the other base materials for the polymer planar Bragg grating would be studied for the better understanding the effect of the material properties.
- Rigorous modeling works would be needed to understand the thermo-optical behavior of the polymer planar Bragg gratings.

Appendices

A. Solution Procedure to Obtain the Optical Power along the PFBG

Using R(0) = 1 and S(L) = 0, the following equation can be obtained from Eq. (4.17).

$$r_1 + r_2 = 1 \tag{A.1}$$

$$s_1 e^{mL} + s_2 e^{-mL} = 0 \tag{A.2}$$

Substitution of the general solutions into the coupled-mode equation yields

$$\frac{dR}{dz} = \frac{d}{dz}\left(r_1 e^{mz} + r_2 e^{-mz}\right) = -\left(\frac{\hat{a}}{2} + i\delta\right)\left(r_1 e^{mz} + r_2 e^{-mz}\right) - i\kappa\left(s_1 e^{mz} + s_2 e^{-mz}\right) \tag{A.3}$$

The above equation can be rearranged as

$$e^{mz}\left[r_1\left(m + \frac{\hat{a}}{2}\right) + i\left(\delta r_1 + \kappa s_1\right)\right] + e^{-mz}\left[r_2\left(-m + \frac{\hat{a}}{2}\right) + i\left(\delta r_2 + \kappa s_2\right)\right] = 0 \tag{A.4}$$

, which produces two additional conditions required to determine the four constants in the general solution as

$$r_1\left(m + \frac{\hat{a}}{2}\right) = -i\left(\delta r_1 + \kappa s_1\right) \tag{A.5}$$

$$r_2\left(-m + \frac{\hat{a}}{2}\right) = -i\left(\delta r_2 + \kappa s_2\right) \tag{A.6}$$

Solving four simultaneous equations ((A.1), (A.2), (A.5), and (A.6)), the coefficients of the general solution can be obtained as

$$r_1 = \frac{m - \left(\frac{\hat{a}}{2} + i\delta\right)}{m - \left(\frac{\hat{a}}{2} + i\delta\right) + \left[m + \left(\frac{\hat{a}}{2} + i\delta\right)\right]e^{2mL}} \tag{A.7}$$

$$r_2 = \frac{\left[m + \left(\frac{\hat{a}}{2} + i\delta\right)\right] e^{2mL}}{m - \left(\frac{\hat{a}}{2} + i\delta\right) + \left[m + \left(\frac{\hat{a}}{2} + i\delta\right)\right] e^{2mL}} \tag{A.8}$$

$$s_1 = \frac{m^2 - \left(\frac{\hat{a}}{2} + i\delta\right)^2}{-i\kappa\left[m - \left(\frac{\hat{a}}{2} + i\delta\right) + \left[m + \left(\frac{\hat{a}}{2} + i\delta\right)\right] e^{2mL}\right]} \tag{A.9}$$

$$s_2 = \frac{\left[m^2 - \left(\frac{\hat{a}}{2} + i\delta\right)^2\right] e^{2mL}}{i\kappa\left[m - \left(\frac{\hat{a}}{2} + i\delta\right) + \left[m + \left(\frac{\hat{a}}{2} + i\delta\right)\right] e^{2mL}\right]} \tag{A.10}$$

Coefficients for the solution of axial powers are

$$c_1 = \left(m_1 - \frac{\hat{a}}{2}\right)^2 + (m_2 - \delta)^2 \tag{A.11}$$

$$c_2 = \left(m_1 + \frac{\hat{a}}{2}\right)^2 + (m_2 + \delta)^2 \tag{A.12}$$

$$c_3 = 2e^{2m_1 L}\left(m_1{}^2 + m_2{}^2 - \left(\frac{\hat{a}}{2}\right)^2 - \delta^2\right) \tag{A.13}$$

$$c_4 = -4e^{2m_1 L}\left(-m_1\delta + m_2\frac{\hat{a}}{2}\right) \tag{A.14}$$

$$c_5 = 2e^{2m_1 L}\left(\left(m_1{}^2 + m_2{}^2 - \left(\frac{\hat{a}}{2}\right)^2 - \delta^2\right)\cos(2m_2 L) + 2\left(-m_1\delta + m_2\frac{\hat{a}}{2}\right)\sin(2m_2 L)\right) \tag{A.15}$$

$$c_6 = \left(m_1{}^2 - m_2{}^2 - \left(\frac{\hat{a}}{2}\right)^2 + \delta^2\right)^2 + 4\left(m_1 m_2 - \frac{\hat{a}}{2}\delta\right)^2 \tag{A.16}$$

$$c_7 = 2\kappa^2 e^{2m_1 L}\left(\left(m_1{}^2 + m_2{}^2 - \left(\frac{\hat{a}}{2}\right)^2 - \delta^2\right)\cos(2m_2 L) + 2\cdot\left(-m_1\delta + m_2\frac{\hat{a}}{2}\right)\sin(2m_2 L)\right) \quad \text{(A.17)}$$

B. Solution Procedure to Determine the Temperature Profile along the PFBG

B.1. Solution procedure of the temperature profile along the PFBG with the LED

Substituting the proposed particular solution into the conduction equation (Eq. (4.36)), the coefficient of the particular solution can be obtained as

$$D = \frac{P_{inc}\hat{a}}{\left(p^2 - \hat{a}^2\right)\left(\pi r_o{}^2 k\right)} \quad \text{(B.1)}$$

Using boundary conditions, both ends of Bragg grating are adiabatic,

$$\left.\frac{d\theta}{dz}\right|_{z=0} = pg_1 - pg_2 - \hat{a}D = 0 \quad \text{(B.2)}$$

$$\left.\frac{d\theta}{dz}\right|_{z=L} = pg_1 e^{pL} - pg_2 e^{-pL} - \hat{a}De^{-\hat{a}L} = 0 \quad \text{(B.3)}$$

Two coefficients of the general solution can be determined as

$$g_1 = \frac{\hat{a}D\left(e^{-\hat{a}L} - e^{-pL}\right)}{p\left(e^{pL} - e^{-pL}\right)} \quad \text{(B.4)}$$

$$g_2 = g_1 - \frac{\hat{a}}{p}D \quad \text{(B.5)}$$

B.2. Solution procedure of the temperature profile along the PFBG with the SM LD

Rearranging the non-homogeneous term in the conduction equation associated with the SMLD (Eq. (4.42)) yields

$$\left(-\frac{q_G(z)}{k}\right)=\frac{-P_{inc}}{k\pi {r_o}^2}\cdot\hat{a}\int_{\lambda_1}^{\lambda_4}\overline{P(\lambda)}\left(\left|R(\lambda,z)\right|^2+\left(\left|S(\lambda,z)\right|\right)^2\right)d\lambda$$

$$=\frac{-P_{inc}}{k\pi {r_o}^2}\cdot\hat{a}\int_{\lambda_1}^{\lambda_4}Be^{4\ln 0.5\left(\frac{\lambda-\lambda_c}{FWHM}\right)^2}\cdot\left(a_1(\lambda)e^{2m_1(\lambda)z}+a_2(\lambda)e^{2m_1(\lambda)(2L-z)}\right)d\lambda$$

$$-\frac{P_{inc}}{k\pi {r_o}^2}\cdot\hat{a}\int_{\lambda_2}^{\lambda_3}Be^{4\ln 0.5\left(\frac{\lambda-\lambda_c}{FWHM}\right)^2}\cdot\left(a_3(\lambda)\cos\left(2m_2(\lambda)(z-L)\right)+a_4(\lambda)\sin\left(2m_2(\lambda)(z-L)\right)\right)d\lambda$$

$$-\frac{P_{inc}}{k\pi {r_o}^2}\cdot\hat{a}\int_{\lambda_1}^{\lambda_2}Be^{4\ln 0.5\left(\frac{\lambda-\lambda_c}{FWHM}\right)^2}\cdot\left(a_3(\lambda)\left(\left(\frac{1-\cos\left(2m_2(\lambda)L\right)}{L}\right)z+\cos\left(2m_2(\lambda)L\right)\right)\right.$$

$$\left.+a_4(\lambda)\left(\frac{\sin\left(2m_2(\lambda)L\right)}{L}z-\sin\left(2m_2(\lambda)L\right)\right)\right)d\lambda$$

$$-\frac{P_{inc}}{k\pi {r_o}^2}\cdot\hat{a}\int_{\lambda_3}^{\lambda_4}Be^{4\ln 0.5\left(\frac{\lambda-\lambda_c}{FWHM}\right)^2}\cdot\left(a_3(\lambda)\left(\left(\frac{1-\cos\left(2m_2(\lambda)L\right)}{L}\right)z+\cos\left(2m_2(\lambda)L\right)\right)\right.$$

$$\left.+a_4(\lambda)\left(\frac{\sin\left(2m_2(\lambda)L\right)}{L}z-\sin\left(2m_2(\lambda)L\right)\right)\right)d\lambda \qquad \text{(B.6)}$$

$$a_1(\lambda)=\frac{c_1}{c_1+c_5+c_2e^{4m_1L}}+\frac{c_6}{\kappa^2c_2e^{4m_1L}+2\kappa^2c_5+\kappa^2c_1}$$

$$a_2(\lambda)=\frac{c_2}{c_1+c_5+c_2e^{4m_1L}}+\frac{c_6}{\kappa^2c_2e^{4m_1L}+2\kappa^2c_5+\kappa^2c_1}$$

$$a_3(\lambda)=\frac{c_3}{c_1+c_5+c_2e^{4m_1L}}+\frac{c_6}{\kappa^2c_2e^{4m_1L}+2\kappa^2c_5+\kappa^2c_1}\left(-2e^{2m_1L}\right)$$

$$a_4(\lambda)=\frac{c_4}{c_1+c_5+c_2e^{4m_1L}}$$

The particular solution can take a form as

$$\theta_p = \int_{\lambda_1}^{\lambda_4} F(\lambda)e^{2m_1(\lambda)z}d\lambda + \int_{\lambda_1}^{\lambda_4} G(\lambda)e^{-2m_1(\lambda)z}d\lambda + \int_{\lambda_2}^{\lambda_3} H(\lambda)\cos(M(\lambda)(z-L))d\lambda$$
$$+ \int_{\lambda_2}^{\lambda_3} N(\lambda)\sin(U(\lambda)(z-L))d\lambda + \int_{\lambda_1}^{\lambda_2} V(\lambda)z + W(\lambda)d\lambda + \int_{\lambda_3}^{\lambda_4} V(\lambda)z + W(\lambda)d\lambda \quad \text{(B.7)}$$
$$+ \int_{\lambda_1}^{\lambda_2} X(\lambda)z + Y(\lambda)d\lambda + \int_{\lambda_3}^{\lambda_4} X(\lambda)z + Y(\lambda)d\lambda$$

By substituting the above particular solution (Eq. (B.7)) into the governing equation (Eq. (4.42)), one can obtain the following equation.

$$\int_{\lambda_1}^{\lambda_4} \left(4(m_1(\lambda))^2 - p^2\right)F(\lambda)e^{2m_1(\lambda)z}d\lambda + \int_{\lambda_1}^{\lambda_4} \left(4(m_1(\lambda))^2 - p^2\right)G(\lambda)e^{-2m_1(\lambda)z}d\lambda$$
$$- \int_{\lambda_2}^{\lambda_3} \left((M(\lambda))^2 + p^2\right)H(\lambda)\cos(M(\lambda)(z-L))d\lambda - \int_{\lambda_2}^{\lambda_3} \left((U(\lambda))^2 + p^2\right)N(\lambda)\sin(U(\lambda)(z-L))d\lambda$$
$$- p^2\int_{\lambda_1}^{\lambda_2} V(\lambda)z + W(\lambda) + X(\lambda)z + Y(\lambda)d\lambda - p^2\int_{\lambda_3}^{\lambda_4} V(\lambda)z + W(\lambda) + X(\lambda)z + Y(\lambda)d\lambda$$
$$= \frac{-P_{inc}}{k\pi r_o^{\,2}} \cdot \hat{a}\int_{\lambda_1}^{\lambda_4} Be^{4\ln 0.5\left(\frac{\lambda-\lambda_c}{FWHM}\right)^2} \cdot \left(a_1(\lambda)e^{2m_1(\lambda)z} + a_2(\lambda)e^{2m_1(\lambda)(2L-z)}\right)d\lambda$$
$$- \frac{P_{inc}}{k\pi r_o^{\,2}} \cdot \hat{a}\int_{\lambda_2}^{\lambda_3} Be^{4\ln 0.5\left(\frac{\lambda-\lambda_c}{FWHM}\right)^2} \cdot \left(a_3(\lambda)\cos(2m_2(\lambda)(z-L)) + a_4(\lambda)\sin(2m_2(\lambda)(z-L))\right)d\lambda$$
$$- \frac{P_{inc}}{k\pi r_o^{\,2}} \cdot \hat{a}\int_{\lambda_1}^{\lambda_2} Be^{4\ln 0.5\left(\frac{\lambda-\lambda_c}{FWHM}\right)^2} \cdot \left(a_3(\lambda)\left(\left(\frac{1-\cos(2m_2(\lambda)L)}{L}\right)z + \cos(2m_2(\lambda)L)\right)\right.$$
$$\left. + a_4(\lambda)\left(\frac{\sin(2m_2(\lambda)L)}{L}z - \sin(2m_2(\lambda)L)\right)\right)d\lambda$$
$$- \frac{P_{inc}}{k\pi r_o^{\,2}} \cdot \hat{a}\int_{\lambda_3}^{\lambda_4} Be^{4\ln 0.5\left(\frac{\lambda-\lambda_c}{FWHM}\right)^2} \cdot \left(a_3(\lambda)\left(\left(\frac{1-\cos(2m_2(\lambda)L)}{L}\right)z + \cos(2m_2(\lambda)L)\right)\right.$$
$$\left. + a_4(\lambda)\left(\frac{\sin(2m_2(\lambda)L)}{L}z - \sin(2m_2(\lambda)L)\right)\right)d\lambda$$

(B.8)

The spectrally dependent coefficients of the particular solution can be found by comparing coefficients in each term of Eq. (B.8) as

$$F(\lambda) = \frac{\dfrac{-P_{inc}}{k\pi r_o^{\,2}} \cdot \hat{a} \cdot Be^{\,4\ln 0.5\left(\frac{\lambda-\lambda_c}{FWHM}\right)^2} \cdot a_1(\lambda)}{\left(4\left(m_1(\lambda)\right)^2 - p^2\right)} \tag{B.9}$$

$$G(\lambda) = \frac{\dfrac{-P_{inc}}{k\pi r_o^{\,2}} \cdot \hat{a} \cdot Be^{\,4\ln 0.5\left(\frac{\lambda-\lambda_c}{FWHM}\right)^2} \cdot a_2(\lambda) \cdot e^{4L\cdot m_1(\lambda)}}{\left(4\left(m_1(\lambda)\right)^2 - p^2\right)} \tag{B.10}$$

$$M(\lambda) = U(\lambda) = 2m_2(\lambda) \tag{B.11}$$

$$H(\lambda) = \frac{\dfrac{P_{inc}}{k\pi r_o^{\,2}} \cdot \hat{a} \cdot Be^{\,4\ln 0.5\left(\frac{\lambda-\lambda_c}{FWHM}\right)^2} \cdot a_3(\lambda)}{\left(4\left(m_2(\lambda)\right)^2 + p^2\right)} \tag{B.12}$$

$$N(\lambda) = \frac{\dfrac{P_{inc}}{k\pi r_o^{\,2}} \cdot \hat{a} \cdot Be^{\,4\ln 0.5\left(\frac{\lambda-\lambda_c}{FWHM}\right)^2} \cdot a_4(\lambda)}{\left(4\left(m_2(\lambda)\right)^2 + p^2\right)} \tag{B.13}$$

$$V(\lambda) = \frac{\dfrac{P_{inc}}{k\pi r_o^{\,2}} \cdot \hat{a} \cdot Be^{\,4\ln 0.5\left(\frac{\lambda-\lambda_c}{FWHM}\right)^2} \cdot a_3(\lambda)}{p^2} \frac{\left(1-\cos\left(2m_2L\right)\right)}{L} \tag{B.14}$$

$$W(\lambda) = \frac{\dfrac{P_{inc}}{k\pi r_o^{\,2}} \cdot \hat{a} \cdot Be^{\,4\ln 0.5\left(\frac{\lambda-\lambda_c}{FWHM}\right)^2} \cdot a_3(\lambda)}{p^2} \cos\left(2m_2L\right) \tag{B.15}$$

$$X(\lambda) = \frac{\dfrac{P_{inc}}{k\pi r_o^{\,2}} \cdot \hat{a} \cdot Be^{\,4\ln 0.5\left(\frac{\lambda-\lambda_c}{FWHM}\right)^2} \cdot a_4(\lambda)}{p^2} \frac{\sin\left(2m_2L\right)}{L} \tag{B.16}$$

$$Y(\lambda)=\frac{-\frac{P_{inc}}{k\pi r_o^{\,2}}\cdot\hat{a}\cdot Be^{\,4\ln 0.5\left(\frac{\lambda-\lambda_c}{FWHM}\right)^2}\cdot a_4(\lambda)}{p^2}\sin(2m_2L) \tag{B.17}$$

Assuming that all the heat loss occurs from the surface of the fiber and neglecting the axial conduction at the fiber ends, i.e., assuming that both ends of the BGs are adiabatic, the following two boundary conditions can be obtained.

$$\left.\frac{d\theta}{dz}\right|_{z=0}=0 \text{ and } \left.\frac{d\theta}{dz}\right|_{z=L}=0$$

Applying the above BCs to the general solution for the excess temperature (Eq. (4.43)),

$$\begin{aligned}\theta'(0)&=pd_1-pd_2+\int_{\lambda_1}^{\lambda_4}2m_1(\lambda)\big(F(\lambda)-G(\lambda)\big)d\lambda+\int_{\lambda_2}^{\lambda_3}H(\lambda)M(\lambda)sin\big(L\cdot M(\lambda)\big)d\lambda\\&+\int_{\lambda_2}^{\lambda_3}N(\lambda)M(\lambda)cos\big(L\cdot M(\lambda)\big)d\lambda+\int_{\lambda_1}^{\lambda_2}V(\lambda)+X(\lambda)d\lambda+\int_{\lambda_3}^{\lambda_4}V(\lambda)+X(\lambda)d\lambda=0\end{aligned} \tag{B.18}$$

$$\begin{aligned}\theta'(L)&=pd_1e^{pL}-pd_2e^{-pL}+\int_{\lambda_1}^{\lambda_4}2m_1(\lambda)F(\lambda)e^{2m_1(\lambda)L}d\lambda-\int_{\lambda_1}^{\lambda_4}2m_1(\lambda)G(\lambda)e^{-2m_1(\lambda)L}d\lambda\\&+\int_{\lambda_2}^{\lambda_3}N(\lambda)M(\lambda)d\lambda+\int_{\lambda_1}^{\lambda_2}V(\lambda)+X(\lambda)d\lambda+\int_{\lambda_3}^{\lambda_4}V(\lambda)+X(\lambda)d\lambda=0\end{aligned} \tag{B.19}$$

Solving (B.18) and (B.19) simultaneously, the two coefficients of the general solution can be determined as

$$\begin{aligned}d_1=\frac{1}{p\left(1-e^{2pL}\right)}\Bigg\{&\int_{\lambda_1}^{\lambda_4}-2m_1(\lambda)\Big(F(\lambda)\big(1-e^{L(2m_1(\lambda)+p)}\big)-G(\lambda)\big(1-e^{-L(2m_1(\lambda)-p)}\big)\Big)d\lambda\\&-\int_{\lambda_2}^{\lambda_3}H(\lambda)M(\lambda)\sin\big(L\cdot M(\lambda)\big)+N(\lambda)M(\lambda)\big(\cos\big(L\cdot M(\lambda)\big)-e^{pL}\big)d\lambda\\&-\int_{\lambda_1}^{\lambda_2}\big(V(\lambda)+X(\lambda)\big)\big(1-e^{pL}\big)d\lambda-\int_{\lambda_3}^{\lambda_4}\big(V(\lambda)+X(\lambda)\big)\big(1-e^{pL}\big)d\lambda\Bigg\}\end{aligned} \tag{B.20}$$

$$d_2 = d_1 + \frac{1}{p}\left\{\int_{\lambda_1}^{\lambda_4} 2m_1(\lambda)(F(\lambda) - G(\lambda))d\lambda \right.$$
$$+ \int_{\lambda_2}^{\lambda_3} H(\lambda)M(\lambda)\sin(L \cdot M(\lambda)) + N(\lambda)M(\lambda)\cos(L \cdot M(\lambda))d\lambda \qquad \text{(B.21)}$$
$$\left. + \int_{\lambda_1}^{\lambda_2} V(\lambda) + X(\lambda)d\lambda + \int_{\lambda_3}^{\lambda_4} V(\lambda) + X(\lambda)d\lambda \right\}$$

REFERENCES

[1] L. Eldada and L. Shacklette, Advances in polymer integrated optics, IEEE Journal of Selected Topics in Quantum Electronics 6 (2000) 54-68

[2] K.O. Hill and G. Meltz, Fiber Bragg grating technology fundamentals and overview, Journal of Lightwave Technology 15 (1997) 1263-1276

[3] K.O. Hill, B. Malo, et al., Bragg Gratings fabricated in monomode photosensitive optical fiber by UV exposure through a phase mask, Applied Physics Letters 62 (1993) 1035-1037

[4] K.O. Hill, Y. Fujii, D.C. Johnson, and B.S. Kawasaki, Photosensitivity in optical fiber waveguides, Applied Physics Letters 32 (1978) 647-649

[5] A.Othonos, Fiber Bragg gratings-fundamentals and applications in telecommunications and sensing, Artech House, Boston,1999

[6] Z. Xiong, G.D. Peng, B. Wu, and P.L. Chu, Highly tunable Bragg gratings in single-mode polymer optical fibers, IEEE Photonics technology letters 11 (1999) 352-354

[7] Y.-J. Rao, D.J. Webb, D. A. Jackson, L. Zhang, I. Bennion, In-Fiber Bragg-grating temperature sensor system for medical applications, Journal of Lightwave Technology 15 (1997) 779-785

[8] E.D.J. Smith, B.A. Patterson, R.J. Webster, P.A. Krug, S.K. Jones, D.D. Sampson, Engineering a portable quasi-distributed fibre-Bragg-grating temperature sensing system for clinical hyperthermia, Optical Fiber Sensors Conference Technical Digest, 2002. OFS 2002, 15th , 6-10 May 2002, 269-272

[9] B. A. Patterson, D.D. Sampson, et. al., In vivo quasi-distributed temperature sensing with fibre Bragg gratings, Lasers and Electro-Optics, 2001. CLEO '01. Technical

Digest. Summaries of papers presented at the Conference on , 6-11 May 2001, 402 – 403

[10] A.V. Koulaxouzidis, M.J. Holmes, C.V. Roberts, V.A. Handerek, A shear and vertical stress sensor for physiological measurements using fibre Bragg gratings, Engineering in Medicine and Biology Society, 2000, Proceedings of the 22nd Annual International Conference of the IEEE ,Volume: 1 , 23-28 July 2000, 55 – 58

[11] N.E. Fisher, J. Surowiec, et. al., In-fibre Bragg gratings for ultrasonic medical applications, Measurement Science & Technology 8 (1997) 1050-1054

[12] T. Katchalski, E. Teitelbaum, Towards ultra-narrow bandwidth polymer-based resonant grating waveguide structures , Applied Physics Letters 84 (2004) 472-474

[13] W. C. Wang, M. Fisher, et. al., Phase-shifted Bragg grating filters in polymer waveguides, IEEE photonics technology letters 15 (2003) 548-550

[14] J.-W. Kang, M.-J. Kim, et. al, Polymeric wavelength filters fabricated using holographic surface relief gratings on azobenzene-containing polymer films, Applied physics letters 82 (2003) 3823-3825

[15] H. Zou, K. W. Beeson, L. W. Shacklette, Tunable planar polymer Bragg gratings having exceptionally low polarization sensitivity, Journal of Lightwave Technology 21 (2003) 1083-1088

[16] T. Augustsson, Proposal of a Bragg grating assisted MMIMI-coupler for tunable add-drop multiplexing, IEEE Photonics Technology Letters 13 (2001) 1011-1013

[17] A. Sato, S. Atsushi, et. al., Holographic edge-illuminated polymer Bragg gratings for dense wavelength division optical filters at 1550 nm, Applied Optics 42 (2003) 778-784

[18] J-F. Viens, C. Callender, et. al., Compact wide-band polymer wavelength-division multiplexers, IEEE Photonics Technology Letters 12 (2000) 1010 -1012

[19] L. Eldada, Y. Shing, et al., Integrated multichannel OADM's using polymer Bragg grating MZI's, IEEE Photonics Technology Letters 10 (1998) 1416-1418

[20] S. Tang, Y. Tang, et. al., Fast electrooptic Bragg grating couplers for on-chip reconfigurable optical waveguide interconnects, IEEE Photonics Technology Letters 16 (2004) 1385-1387

[21] T. Erdogan, Fiber grating spectra, Journal of Lightwave Technology 15 (1997) 1277-1294

[22] C.-L. Chen, Elements of optoelectronics and fiber optics, Irwin, Chicago, 1996

[23] T. Tamir, Guided-wave optoelectronics, Springer-Verlag, New York, 1990

[24] D. Lee, Electromagnetic principles of integrated optics, John Willey and Sons, New York, 1986

[25] R. Steenkiste and G. Springer, Strain and temperature measurement with fiber optic sensors, Technomic Publishing Company, Lancaster, PA, 1997

[26] M. Weber, CRC handbook of laser science and Technology supplement 2: optical materials, CRC press, Boca Raton, FL, 1995

[27] K. Nagano, et al., Change of the Refractive Index in an Optical Fiber due to External Forces, Applied Optics 17 (1978) 2080-2085

[28] N. Borrelli and R. Miller, Determination of the Individual Strain-Optic Coefficients of Glass by an Ultrasonic Technique, Applied Optics 7 (1968) 745-750

[29] M. Born and E. Wolf, Principles of Optics, 5th ed., Pergaman Press, New York, 1975

[30] T. Narasimhamurty, Photoelastic and Electro-Optic Properties of Crystals, Plenum Press, New York (1981)

[31] T. M. Smith, A. Korpel, Measurement of Light-Sound Interaction Efficiencies in Sounds, IEEE Journal of quantum electronics QE-1 (1965) 283-284

[32] D.B. Cavanaugh,C.H. Wang, Measurement of the Photoelastic and Elastic Constants of Drawn Films and Extruded Rods of Polypropylene with Brillouin Light Scattering, Journal of Applied Physics 53 (1982) 2793-2799

[33] A. Kraus, A. Bar-Cohen, Thermal Analysis and Control of Electronic Equipment, Hemisphere Publishing Corp., New York 1983

[34] E. Suhir, An Approximate Analysis of Stresses in Multilayered Elastic Thin Films, Journal of Applied Mechanics 55 (1988) 143-148

[35] S. Moaveni, Finite Element Analysis-Theory and Application with ANSYS, Prentice Hall, New Jersey, 2002

[36] ANSYS 7.0 Online Manual, ANSYS Inc. ,2003

[37] M. Ozisik , Heat Conduction, John Willey and Sons, New York, 1980

[38] B. Boley and J. Weiner, Theory of Thermal Stresses, John Willey and Sons, New York, 1960

[39] B. Booth, Low Loss Channel Waveguides in Polymers, Journal of Lightwave Technology, 7, (1989) 1445-1453

[40] S Imamura,.R. Yoshimura et al., Polymer Channel Waveguides with Low loss at 1.3 μm, Electronic Letters 27 (1991) 1342-1343

[41] M. Zhou, Low-loss Polymeric Materials for Passive Waveguide Components in Fiber Optical Communication, Optical Engineering, 41(2002) 1631-1643

[42] P.K. Cheo, Fiber optics and optoelectronics, Englewood cliffs, NJ, Prentice-Hall, 2nd ed., 1990

[43] Product specification sheets of the Mitsubishi DFB laser diodes (ML9XX12)

[44] Product catalog of Osram Opto-Semiconductors LED

[45] H. Kogelnik, Coupled wave theory for thick hologram gratings, The Bell System Technical Journal 48,(1969) 2909-2947

[46] H. Kogelnik and C.V. Shank, Coupled-wave theory of distributed feedback lasers, Journal of Applied Physics 43 (1972) 2327-2335

[47] A. Yariv, Coupled-mode theory for guided-wave optics, IEEE Journal of Quantum Electronics 9 . (1973) 919-933

[48] D. G. Zill, Advanced engineering mathematics, PWS-KENT Publishing Co., Boston, 1992

[49] H.Y. Liu, G.D. Peng, and P.L. Chu, Thermal stability of gratings in PMMA and CYTOP polymer fibers, Optics Communications 24 (2002) 151-156.

[50] G. D. Peng and P.L. Chu, Polymer optical fiber photosensitivities and highly tunable fiber gratings, Fiber and Integrated Optics 19 (2000) 277-293

[51] M. Yamada and K. Sakuda, Analysis of almost-periodic distributed slab waveguides via a fundamental matrix approach, Applied Optics 26 (1987) 3474-3478

[52] J. E. Sipe, L. Poladian, C. M. D. Sterke, Propagation through non-uniform grating structures, Journal of the Optical Society of America A 11 (1994) 1307-1320

[53] L. A. Weller-Brophy and D.G. Hall, Analysis of waveguide gratings: application of Rouard's method, Journal of the Optical Society of America A 2 (1985) 863-871

[54] P. C. Won, J. Leng, et. al., Distributed temperature sensing using a chirped fibre Bragg grating, Measurement Science and Technology, 15 (2004) 1501-1505

[55] Product specification document, Avensys Inc, 2005

[56] Product specification document, Corning Inc, 2005

[57] T. Irvine and J. Hartnett, Advances in heat transfer, Vo.11, Academic Press, Inc., New York 1975

[58] F. Incropera, D. Dewitt, Fundamentals of Heat and Mass Transfer,4th ed, John Wiley & Sons, New York, 1996.